

1
2 **Geological Characterization of the Ina Shield Volcano Summit Pit Crater on the**
3 **Moon: Evidence for Extrusion of Waning-Stage Lava Lake Magmatic Foams and**
4 **Anomalously Young Crater Retention Ages**

5 **Le Qiao^{1,2}, James W. Head², Zongcheng Ling¹, Lionel Wilson³, Long Xiao⁴, Josef D.**
6 **Dufek⁵, and Jianguo Yan⁶**

7 ¹Shandong Provincial Key Laboratory of Optical Astronomy and Solar-Terrestrial Environment,
8 Institute of Space Sciences, Shandong University, Weihai 264209, China.

9 ²Department of Earth, Environmental and Planetary Sciences, Brown University, Providence, RI
10 02912, USA.

11 ³Lancaster Environment Centre, Lancaster University, Lancaster LA1 4YQ, UK.

12 ⁴Planetary Science Institute, School of Earth Sciences, China University of Geosciences, Wuhan
13 430074, China.

14 ⁵School of Earth and Atmospheric Sciences, Georgia Institute of Technology, Atlanta, Georgia
15 30332, USA.

16 ⁶State Key Laboratory of Information Engineering in Surveying, Mapping and Remote Sensing,
17 Wuhan University 430070, Wuhan, China.

18 Corresponding authors: Le Qiao (leqiao.geo@gmail.com), Zongcheng Ling (zcling@sdu.edu.cn)

19 **Key Points:**

- 20 • Ina feature occurs as a summit pit crater/vent atop a broad ~22-km-diameter, ~3.5-Ga-old
21 shield volcano
- 22 • The range of geologic characteristics of Ina are most consistent with an ancient origin of
23 “waning-stage lava lake magmatic foam extrusion”
- 24 • Highly vesicular nature of the magmatic foam mounds and lava lake crust floor substrate
25 results in anomalously young crater retention ages

26 **Abstract**

27 Ina, a distinctive $\sim 2 \times 3$ km D-shaped depression, is composed of unusual bulbous-shaped mounds
28 surrounded by optically immature hummocky/blocky floor units. The crisp appearance, optical
29 immaturity and low number of superposed impact craters combine to strongly suggest a
30 geologically recent formation for Ina, but the specific formation mechanism remains
31 controversial. We reconfirm that Ina is a summit pit crater/vent on a small shield volcano ~ 3.5
32 billion years old. Following detailed characterization, we interpret the range of Ina characteristics
33 to be consistent with a two-component model of origin during the waning stages of summit pit
34 eruption activities. The Ina pit crater floor is interpreted to be dominated by the products of late-
35 stage, low rise-rate magmatic dike emplacement. Magma in the dike underwent significant
36 shallow degassing and vesicle formation, followed by continued degassing below the solidified
37 and highly micro- and macro-vesicular lava lake crust, resulting in cracking of the crust and
38 extrusion of gas-rich magmatic foams onto the lava lake crust to form the mounds. These unique
39 substrate characteristics (highly porous aerogel-like foam mounds and floor terrains with large
40 vesicles and void space) exert important effects on subsequent impact crater characteristics and
41 populations, influencing 1) optical maturation processes, 2) regolith development and 3)
42 landscape evolution by modifying the nature and evolution of superposed impact craters and thus
43 producing anomalously young crater retention ages. Accounting for these effects results in a shift
44 of crater size-frequency distribution model ages from <100 million years to ~ 3.5 billion years,
45 contemporaneous with the underlying ancient shield volcano.

46 **Plain Language Summary**

47 Among the most outstanding questions in lunar evolution is the end of extrusive volcanic
48 activity, commonly thought to be at least a billion years old. A recent study found evidence for
49 volcanic activity within the last 100 million years, in the form of “irregular mare patches” (IMPs)
50 dated by size-frequency distributions of superposed craters (CSFD). The most prominent IMP is
51 Ina, an $\sim 2 \times 3$ km depression composed of bulbous-shaped mounds surrounded by fresh,
52 hummocky and blocky floor units, both supporting the geologically very recent age. We
53 undertook a detailed characterization of the setting of Ina and its interior, and found that its
54 location on the summit of a 3.5 billion years old small shield volcano, together with Hawaiian
55 field analogs and theoretical analyses of the ascent and eruption of magma, provided new clues
56 to its origin and age. Late-stage magma extrusion in the summit pit characterized by gas-rich
57 strombolian activity produced a very vesicular crust and concentration of underlying magmatic
58 foams; cracking of the crust caused magmatic foam extrusions to produce the mounds. The very
59 porous nature of Ina deposits decreases the superposed crater diameters and shifts the CSFD to
60 ~ 3.5 billion years, coincident with the ancient age of the volcano.

61 **1. Introduction**

62 Ina is an unusual lunar feature in Lacus Felicitatis on the central nearside of the Moon
63 (18.65° N, 5.30° E), first discovered in Apollo 15 orbital photographs (Whitaker, 1972; El-Baz,
64 1973). Located in the midst of mare deposits interpreted to be ancient basalts, the $\sim 2 \times 3$ km letter
65 D-shaped shallow depression consists of unusually bright and blocky floor materials and dozens
66 of bleb-like mounds with cross-sections resembling liquid droplets with a high surface tension
67 and a convex meniscus (El-Baz, 1973; Strain & El-Baz, 1980). Lunar Reconnaissance Orbiter
68 (LRO) high-resolution image and topography data have permitted the characterization of the

69 units within and associated with this feature (Garry et al., 2012), and the identification of dozens
70 of small mare features resembling Ina on the central nearside of the Moon (Stooke, 2012; Braden
71 et al., 2014), described as Irregular Mare Patches (IMPs). Other major lunar IMPs (e.g.,
72 Sosigenes, Maskelyne and Cauchy 5) also have interior structures similar to those of Ina, i.e.,
73 being composed of bulbous-shaped mounds with surrounding lower hummocky and blocky
74 terrains, while some relatively smaller IMPs may only develop topographically lower floor
75 terrains (Braden et al., 2014). On high-resolution optical images, the floor terrains show much
76 more complicated surface textures than the adjacent higher mounds. The optical maturity of the
77 mounds lies between that of the mature surrounding ancient mare and the optically least mature
78 floor units (Bennett et al., 2015).

79 Notable for their morphological crispness, apparent optical immaturity and unusually low
80 superposed impact crater density, Ina and other IMPs are commonly interpreted to be related to
81 geologically very recent processes. Earlier morphological analyses had found the Ina mounds to
82 be some of the youngest lava extrusions on the Moon (Strain & El-Baz, 1980). Crater population
83 studies yielded <100 Ma (million years) or even younger model ages for Ina and several other
84 IMPs, specifically for Ina, ~33 Ma (Braden et al., 2014) or even <10 Ma for the Ina interior
85 (Schultz et al., 2006). Diffusional landscape evolution models reported 5–40 Ma maximum ages
86 for some marginal scarps within Ina, and suggested that some small topographic troughs
87 probably developed within the last 1–2 Ma or are still forming currently (Fassett & Thompson,
88 2014, 2015).

89 The wide range of geological peculiarities of the Ina feature, particularly the anomalously
90 young crater retention ages, has led to various interpretations in terms of its formation
91 mechanism (see summaries of parts of previous investigations in Elder et al., 2017 and Qiao et
92 al., 2018a). Preliminary characterization of Ina attributed the high reflectance of the floor
93 materials to deposition of sublimates (Whitaker, 1972). Earlier photogeologic analyses based on
94 Apollo orbital photographs interpreted the Ina floor as a collapse summit caldera atop an
95 extrusive volcanic dome and the mounds as subsequent small lava extrusions (El-Baz, 1972,
96 1973; Strain & El-Baz, 1980). Schultz et al. (2006) examined the topographic relief, superposed
97 impact crater populations and optical maturity of Ina, and suggested that Ina floor units
98 originated from the removal of fine-grained surface materials by episodic out-gassing within the
99 past 10 Ma, and that they are perhaps still active today. Garry et al. (2012) called on terrestrial
100 analogs (specifically, the McCarty's inflated lava flow field in New Mexico) and found that the
101 Ina interior terrains have comparable dimensions and topographic relief to some terrestrial
102 inflated lava flows, and interpreted Ina as being formed through inflated lava flows (the mounds)
103 followed by lava breakouts from the mound margins which built the hummocky units.

104 Braden et al. (2014) employed high-resolution LRO Narrow Angle Cameras (LROC NAC)
105 images to demonstrate many similarities between the morphology, topography and spectroscopy
106 of Ina and dozens of small topographic anomalies (termed “IMPs”) on the central nearside mare;
107 they interpreted the floor units as disrupted lava pond crust caused by the collapse or drainage of
108 the eruptive vent, and the mounds as small magma extrusions. Braden et al. (2014) also dated the
109 mounds to be <100 Ma old, based on impact crater size-frequency distributions (SFD), crater
110 equilibrium populations and topographic slope analyses. The <100 Ma old estimate is
111 significantly younger than the previous estimated age of the cessation of lunar mare volcanism
112 ~1 billion years ago (Hiesinger et al., 2011; Schultz & Spudis, 1983; Morota et al., 2011). If true,
113 this new age would require a major re-evaluation of the conventional theory of lunar heat sources

114 and lunar thermal evolution models. Carter et al. (2013) examined the radar scattering from Ina
115 and two other IMPs, and found that lunar IMPs exhibited a range of radar backscatter properties.
116 The edges of the Ina depression and the interior blocky units are characterized by enhanced
117 circular polarization ratio (CPR) values, while the Ina mounds have CPR values similar to those
118 of the surrounding mare deposits, indicating relatively homogeneous near-surface physical
119 properties. Another lunar IMP feature studied (i.e., Cauchy 5) exhibits radar signals consistent
120 with fine-grained, block-free materials, suggesting a potential origin of being mantled by
121 pyroclastic deposits or other very fine-grained deposits (Carter et al., 2013).

122 Bennett et al. (2015) used Moon Mineralogy Mapper (M^3) spectroscopic data to analyze the
123 mineralogy and optical maturity of Ina, and found that the multiple terrains within Ina and
124 surrounding mare all exhibited similar, high-Ca pyroxene-dominated mineralogy, while optical
125 maturity varied: the maturity of the mounds lies between those of the surrounding mature
126 background mare and the least mature floor materials. Bennett et al. (2015) interpreted the
127 multiple interior morphologic units of Ina to be emplaced contemporaneously with the
128 surrounding ancient mare basalts, and interpreted the apparent optical immaturity of the floor
129 units as being due to their elevated blockiness; however, neither the precise formation
130 mechanism, nor other observed characteristics, particularly the apparently low number of
131 superposed impact craters, were explained by Bennett et al. (2015). Elder et al. (2016, 2017)
132 analyzed the thermophysical measurements collected by the LRO Diviner thermal radiometer,
133 and found that (1) the Ina interior is only slightly rockier than the surrounding mature mare
134 regolith, while much less rocky than the ejecta of some ~100 Ma-old craters; (2) the surface
135 regolith of the Ina interior is interpreted to be thicker than 10–15 cm; and (3) the Ina interior has
136 slightly lower thermal inertia than the surrounding mare, indicating that the Ina materials are less
137 consolidated or contain fewer small rock fragments than typical regolith. These surface physical
138 properties suggest either that Ina is older than its calculated crater retention ages, or that Ina is
139 indeed <100 Ma old, but its surface accumulates regolith more rapidly than blocky ejecta
140 deposits. Elder et al. (2017) proposed that some form of explosive activity, either pyroclast
141 deposition (Carter et al., 2013) or another style of outgassing (Schultz et al., 2006) was likely to
142 have been involved in the formation of Ina, though the possibility of lava flow inflation (Garry et
143 al., 2012) or regolith drainage into subsurface void space (Qiao et al., 2016) could not be
144 precluded; however, the specific formation mechanism and emplacement sequences of the
145 various morphologic units within Ina were not detailed by Elder et al. (2017).

146 Neish et al. (2017) compared the surface physical properties of Ina mounds and lunar
147 impact melt flows at Korolev X via LROC NAC DTM topography and Mini-RF S-Band radar
148 images, and found that Ina mounds have similar physical properties (e.g., Hurst exponent and
149 RMS slope) to lunar impact melt flows at the meter scale (both appear “smooth”). However, Ina
150 mounds appear much “smoother” than lunar impact melt flows at decimeter scale. Integrating
151 analyses with other physical property investigations (Neish et al., 2014) of lunar Copernican
152 impact melts (Ravi et al., 2016) indicate either that Ina mounds are not formed by Copernican
153 lava flow emplacement, or that young lava flows have different physical properties from those of
154 similarly-aged impact melt flows on the Moon. Valantinas et al. (2018) presented new impact
155 crater SFD measurements of the Sosigenes and Nibum IMPs, and obtained model ages of 22 ± 1
156 Ma and 46 ± 5 Ma, respectively. They also observed production-like cumulative log-log SFD
157 slopes of -3 for these superposed craters, suggesting these crater populations are probably still in
158 production. Valantinas et al. (2018) concluded that the Nubium and Sosigenes IMPs might have

159 been affected by a unique endogenic process, though the specific modification mechanism is not
160 detailed.

161 Recent theoretical treatments of final-stage shield-building magmatic activity and volatile
162 exsolution physics (Wilson & Head, 2017a; Head & Wilson, 2017) provided a framework to
163 interpret Ina as a drained summit pit crater lava lake atop an ancient shield volcano ~3.5 billion
164 years (Ga) old, contemporaneous with the major phase of lunar mare volcanism (Qiao et al.
165 2017; Wilson & Head, 2017b). In this hypothesis, the floor hummocky and blocky units are the
166 solidified lava lake crust, which is several meters thick and very vesicular, both at the micro-
167 vesicular and macro-porosity scales due to the presence of large void spaces generated by crust
168 deformation, bubble coalescence, and disruption during the very late stage volatile-release-driven
169 strombolian eruptions. The lava lake crust is underlain by the hypothesized magmatic foams
170 accumulated in the top tens to hundreds of meters of the dike and in the lake interior, produced
171 through the exsolution of H₂O and the gradual decrease of magma ascent rates. The mounds are
172 interpreted as solidified magmatic foams extruded through fractures in the chilled lava lake crust,
173 characterized by abundant small vesicles, with an extremely high vesicularity, up to ~95%. The
174 unique physical properties of the floor units (abundant small vesicles and large void space) and
175 the mounds (magmatic foams) significantly change the behavior of the subsequent impact
176 cratering and regolith development processes, topographic degradation, and surface weathering,
177 maintaining the observed apparent optical immaturity and crisp appearance, and resulting in an
178 anomalously young crater retention age for the Ina interior units (Qiao et al. 2017).

179 In the present contribution, building on these previous analyses and hypotheses of origin for
180 the Ina feature above (Strain & El-Baz, 1980; Schultz et al., 2006; Garry et al., 2012; Braden et
181 al., 2014; Qiao et al., 2017; Wilson & Head, 2017b), we undertake a detailed and comprehensive
182 analysis of the data available for Ina (see detailed analysis data and methods in Text S1 in the
183 supporting information) and characterize 1) the regional geologic context, 2) the quantitative
184 topography, morphology and morphometry of the Ina interior terrains (including the mounds,
185 ledge, scarps, floor hummocky and blocky units, pit formations, depressions and topographic
186 moats), 3) impact craters (including identification, morphology, size-frequency distributions and
187 the discrepancy between different interior units and the surrounding ancient mare), 4) regolith
188 thickness and its variations among different regions, and 5) optical reflectivity and maturity. We
189 focus on the following specific questions to assess the multiple theories of origin: 1) what is the
190 nature of the specific morphological units in Ina and the nature, distribution and relationships of
191 the “mound” and the “hummocky floor” materials? 2) what is the nature of the detailed
192 topography within Ina and how does it relate to the distribution of the “mound” and the
193 “hummocky floor” material? 3) the Ina structure shows an anomalously immature interior, thus
194 supporting a young age: what is the detailed nature and distribution of the immaturity within Ina,
195 how does it relate to the detailed geologic units, and how does this inform the discussion of Ina
196 origin? 4) the Ina structure shows a paucity of superposed impact craters, thus supporting a
197 young age: what is the detailed nature and distribution of the existing impact craters within Ina
198 and how does this inform the discussion of the origin of Ina? 5) if Ina represents a shield volcano
199 summit pit crater, how does its geology and morphology support or challenge models of a)
200 geologically recent, or b) final-stage summit pit crater evolution during a phase of ancient shield-
201 building volcanism? 6) what are the detailed pros and cons for volcanism occurring in the last
202 100 Ma? 7) what are the outstanding questions that can be addressed to resolve the origin of Ina
203 (and other IMPs)? Then, on the basis of terrestrial analog observations of terrestrial small shield
204 volcanoes in Hawai'i, and lunar mare basalt ascent and eruption theory and observations (Wilson

205 & Head, 2017a; Head & Wilson, 2017), we address alternative formation mechanisms of the
206 ranges of characteristics associated with Ina and their post-emplacement geologic modification,
207 especially the observed anomalously young crater retention ages. We also discuss the
208 implications for the origin of other lunar IMPs, the duration of mare volcanism, and the potential
209 of Ina as a target for future surface exploration missions.

210 **2. Regional Setting of the Ina Pit Crater**

211 2.1 Regional morphology and topography

212 The enigmatic Ina feature occurs in the middle of Lacus Felicitatis, a relatively small mare
213 basaltic plain (diameter ~ 90 km, area $\sim 2.24 \times 10^3$ km²) among three extensive maria: Mare
214 Vaporum in the south, Mare Imbrium in the northwest and Mare Serenitatis in the northeast
215 (Figure 1a). Lacus Felicitatis is surrounded by voluminous ejecta deposits from the Imbrium and
216 Serenitatis basins, and the Ina feature is only ~ 3 km from the adjacent basin ejecta (Figure 1a).
217 These ejecta deposits are overprinted by distinctive linear ridged and grooved patterns,
218 dominantly in a northwest-southeast trend and radial to the Imbrium basin center (Strain & El-
219 Baz, 1980; Figure 1a). The formation of these lineaments is generally thought to be related to the
220 catastrophic Imbrium impact event ~ 3.85 Ga ago (e.g., Stöffler & Ryder, 2001) or subsequent
221 ejecta sedimentation process, while the specific origin is largely unknown (e.g., Head, 1976;
222 Spudis, 1993). Northeast-southwest trending lineaments radial to the Serenitatis basin have also
223 been observed, which have been heavily covered and degraded by subsequent Imbrium ejecta
224 (Strain & El-Baz, 1980; Figure 1a).

225 The basalts of Lacus Felicitatis, along with several other small patches of mare, e.g., Lacus
226 Odii and Lacus Doloris (Figure 1a), are superposed on these highland materials ejected from the
227 two giant basins. The Lacus Felicitatis mare deposits are ~ 100 – 220 km from the southeastern
228 main rim of the Imbrium basin, and ~ 80 – 150 km from the intermediate ring of the Serenitatis
229 basin (Figure 1a). The Imbrium ejecta deposits feature a continuous and rapid elevation decrease
230 from the Imbrium main rim (Montes Apenninus) to the Lacus Felicitatis mare region, with a total
231 topographic relief of ~ 2.5 km across a distance of 150 km (Figure 1b, c). From the intermediate
232 rim (Montes Haemus) of the Serenitatis basin to Lacus Felicitatis, the regional surface elevation
233 decreases by ~ 1.4 km across a distance of ~ 90 km (Figure 1b, d).

234 The mare basalts within Lacus Felicitatis show evidence of multiple phases of lava infilling
235 activity and complex geological modification processes. The surface elevations of the Lacus
236 Felicitatis mare deposits are generally higher than those of the adjacent mare deposits, e.g.,
237 Lacus Odii, Lacus Doloris and Mare Vaporum (Figure 1b). Compared with the neighboring
238 Lacus Odii, the Lacus Felicitatis deposits are characterized by an at least ~ 80 m higher elevation.
239 The basalts of Lacus Felicitatis have a relatively uniform iron abundance (Figure 2c, FeO = 15.8
240 ± 1.2 wt.%), but show a titanium enrichment toward the east (Figure 2b, d) (calculated from
241 Clementine UVVIS data using the Lucey et al., (2000a) algorithm). The central Lacus Felicitatis
242 is characterized by a raised plateau, which is ~ 800 m higher than the eastern Lacus Felicitatis
243 basalts, and ~ 650 m higher than the western Lacus Felicitatis basalts (Figures 1b and 3b,d). This
244 plateau dips toward the west: the west margin scarp has a steeper kilometer-scale slope ($\sim 9^\circ$, 305
245 m/ 1900 m) than the eastern scarp ($\sim 6^\circ$, 740 m/ 6600 m). The west scarp extends both north and
246 south, into the highlands, in a direction radial to the Imbrium rim and appears to merge with
247 wrinkle ridges crossing eastern Mare Vaporum (Figure 1a). The central Lacus Felicitatis basalts

248 have an intermediate titanium abundance ($\text{TiO}_2 = 4.4 \pm 1.0$ wt.%) and, in particular, the materials
249 in the Ina interior and a nearby fresh crater show apparently elevated titanium contents,
250 suggesting the exposure of underlying high-titanium mare basalts (see section 3.14 for more
251 details).

252 2.2 The Ina shield volcano

253 New high-resolution altimetry and image data from the LRO and Kaguya spacecraft clearly
254 show that Ina is not only located within the Lacus Felicitatis mare deposits, but also occurs as an
255 $\sim 2 \times 3$ km depression atop a shield volcano (Figure 3), consistent with the previous interpretation
256 of Strain and El-Baz (1980). This shield is ~ 22 km wide at its base and ~ 320 m high (Qiao et al.,
257 2017), and at the upper end of the base diameter and height range for over 300 mare domes
258 which are interpreted as small shield volcanoes (Head & Gifford, 1980; Tye & Head, 2013;
259 Figure 4a). The diameter of the Ina pit crater also lies on the summit crater diameter/base
260 diameter trend line of lunar small shields (Figure 4b). Lunar small shield volcanoes are generally
261 interpreted to develop when dikes propagate to the surface and shields build up through multiple
262 phases of flows erupted from a common pit crater source, dominated by accumulating low-
263 effusion rate, cooling-limited flows (Head & Wilson, 1992, 2017). The Ina shield volcano is well
264 developed in the southern portion, while the growth of the northern part is affected by the pre-
265 existing ejecta deposits. The topographic slope of this shield is typical $\sim 2\text{--}6^\circ$ (Figure 3c). A
266 linear rille is observed crossing the Ina shield volcano, extending west-northwest to the proximal
267 highlands, and east-southeast to the lower eastern Lacus Felicitatis mare deposits (Figure 3). The
268 trend of this rille is non-radial to the Imbrium center, distinguishing it from a set of low-relief
269 radial lineations in the surrounding ejecta deposits; the latter lineations are generally interpreted
270 to originate from the giant Imbrium impact (e.g., Head, 1976; Schultz & Crawford, 2016). Cross-
271 cutting relationships indicate that this linear rille developed after the building of the Ina shield.

272 We dated the Ina shield volcano using impact crater SFD measurements and LROC NAC
273 images on the south flank and obtained an absolute model age of 3.5 (+0.06/-0.1) Ga (Qiao et al.,
274 2017; Figure S1), which is consistent with previous >3.5 Ga estimation by Schultz et al. (2006)
275 and shows unequivocally that this shield is ancient and contemporaneous with the major phase of
276 lunar mare volcanism (Papike et al., 1976; Hiesinger et al., 2011). Any interpretation that calls on
277 Ina floor features to be formed geologically very recently (e.g., <100 Ma) must also explain why
278 these features are located in an ancient volcano summit pit crater.

279 3. Interior of Ina

280 High resolution LROC NAC image (up to ~ 0.48 m pixel size) and altimetry (2 m/pixel) data
281 have permitted the detailed characterization of the interior units of Ina pit crater (Garry et al.,
282 2012; Braden et al., 2014; Qiao et al., 2017). Here, we utilize previous studies, new data and
283 mapping to report some updated and more comprehensive observations of the quantitative
284 topography, morphology morphometry, crater population, regolith thickness and optical
285 properties of Ina interior terrains. These quantitative characterizations will provide important
286 information for constraining the emplacement process of each interior units and the comparison
287 with those of other IMPs will contribute fundamental observation to future investigations of IMP
288 characteristics and origin.

289 3.1 General characterization

290 The Ina crater interior is delimited by an inward-facing wall (typical up to ~100 m wide,
 291 ~10 m high and 5–10° slope) and a relatively flat basal terrace/ledge (typical ~50 m wide, up to
 292 ~5 m high, and <5° slope) with a steep (10–30° slope) inward-facing scarp up to ~12 m high
 293 (Figures 5-8). The entire interior is broadly letter D-shaped (El-Baz, 1973 and Figure 5), with a
 294 dimension of $\sim 2.9 \times 2.1$ km and a surface area of 4.55 km². Bounding the rim is a raised
 295 topographic “collar”, about 0.5–1 km wide and up to ~30 m high relative to the surrounding
 296 mare shield (Figure 3 in Garry et al., 2012). The interior floor is generally flat, slopes gently
 297 (<2°) toward the center (Figure 6), and mainly lies about 20–50 m below the rim (Figures 6 and
 298 7). The interior of Ina pit crater is dominated by three morphological units typical for other major
 299 lunar IMPs (Figure 5b): (1) the unusual meniscus-like mounds, rising up to ~20 m above the
 300 proximal floor units (Figure 7), occupying ~50% of the total interior area, (2) topographically
 301 lower hummocky units (~44% by area) with ridged and pitted textures, and (3) topographically
 302 lower blocky materials consisting of 1–5 m size boulders (Strain & El-Baz, 1980; Schultz et al.,
 303 2006; Garry et al., 2012; Braden et al., 2014; Qiao et al., 2017, 2018a). The mounds are generally
 304 convex upward (Figures 6 and 7), very flat at the tops, and reach steep slopes (~10–30°) at the
 305 edges (Figure 6c). Among the multiple terrains within the Ina interior, only the major mound at
 306 the eastern margin has an IAU confirmed name, termed *Mons Agnes* (Figure 5a). In the
 307 following subsections, we will characterize each morphologic terrain with specific details.

308 3.2 Mounds

309 A key question in determining the origin of the range of features in Ina is their morphology,
 310 morphometry, and relationship to one another. We identify 88 mounds within the Ina interior
 311 (Figure 5b and Figure S2 with mounds numbered), compared with more than fifty mounds
 312 reported by Garry et al. (2012). The mounds have a total surface area of 2.27 km², and occupy
 313 ~50% of the Ina interior area. The surface area of individual mounds ranges from 340 m² – 0.72
 314 km², with an average value of 0.025 ± 0.087 km²; the mounds display a log-linear area
 315 distribution (Figure S3 and Vaughan & Head, 2012). The maximum length of all the Ina mounds
 316 ranges from 0.03 – 2 km, with a bimodal frequency distribution pattern, peaking at 0.04 – 0.06
 317 km and ~0.2 km (Figure S4).

318 For all the Ina mounds, their distances from the depression geometric center (18.6544°N,
 319 5.30262°E) are approximately normally distributed, peaking between 800–1000 m (Figure S5).
 320 Of the 88 identified mounds, 15 of them are spatially continuous with the depression walls, and
 321 relatively flat ledge terrains are often observed between the walls and most of these wall-
 322 connected mounds (Figure 5). For the other mounds, which are not connected with the
 323 depression wall ($n = 73$), the distribution of the distance from mound margins to the Ina interior
 324 floor edge is shown in Figure S6. The majority of the Ina mounds are within ~300 m of the floor
 325 edge, while some very small mounds (typically less than ~0.01 km²) occur in the interior portion
 326 of the depression floor (Figure 5b).

327 The summits of the mounds are always below the rim of Ina (with an average elevation of
 328 ~-274 m) (Figure 6a); the average elevation of Ina mound summits (~312 m) is ~38 m below the
 329 rim, with a range of ~33 m (Figure S7); the mound summit elevations decrease (relative to the
 330 rim crest) toward the center of Ina (Figures 6 and 7; Garry et al., 2012; Qiao et al., 2017). We
 331 measure the proximal terrain topography around the Ina mounds, with a distance of 5–30 m from
 332 the mound edges to avoid the topographically lowest moats, usually present at the mound
 333 margins. The difference between the summit elevation of each mound and the average elevation

334 of the proximal floor region is calculated as the height of each mound. Examination of the
 335 height-frequency distribution of the Ina mounds and their average areas (Figure S8) shows an
 336 obvious size-height grouping: smaller mounds are generally shorter than their larger
 337 counterparts. For the 60 smaller mounds (surface area $< \sim 0.01 \text{ km}^2$), their heights are generally
 338 within $\sim 8 \text{ m}$. While relatively larger mounds generally have much greater heights, for 22 mounds
 339 higher than 8 m , 14 of them have surface areas greater than $\sim 0.03 \text{ km}^2$. The calculated volumes
 340 (assuming a plane base model) of 85 identified mounds (excluding those mounds with negative
 341 calculated heights) on the Ina floor total 0.0258 km^3 , and show a wide range for individual
 342 mound volumes between 41 and $9.2 \times 10^6 \text{ m}^3$ (Figure S9), with mean and median values of $3.0 \times$
 343 10^5 and $1.6 \times 10^4 \text{ m}^3$, respectively. Individual Ina mounds mainly exhibit roughly elliptical map-
 344 view shapes (Figure 5b), while much more extensive mounds generally exhibit complex,
 345 coalescing bleb-like shape patterns (e.g., the largest mound in the center, Figure 5b), and appear
 346 to “be comprised of multiple mounds that are interconnected” (Garry et al., 2012). The mounds
 347 are generally characterized by convex cross-sectional profiles, with surface topography
 348 becoming steeper towards the margins (Figures 6, 7 in Garry et al., 2012). The cross-section
 349 profiles are often asymmetric, the surface elevation typically tilts towards the pit crater floor
 350 interior, with a maximum relief between one side of a mound and the other side of up to $\sim 12 \text{ m}$
 351 (Figure 7 in Garry et al., 2012). In addition, relatively larger mounds ($> 100 \text{ m}$ wide) commonly
 352 develop nearly flat tops (mainly $< 2^\circ$ in surface slope) (Figure S10) where the total topographic
 353 relief is only $1\text{--}2 \text{ m}$ over 100s of meters (Garry et al., 2012).

354 We calculated the surface area-averaged topographic slope and orientation of each mound
 355 (Figure S11) based on LROC NAC DTM raster topography, using the following algorithms:

$$\text{slope} = \text{atan2}\left(\frac{1}{N} \sum_{i=1}^N \frac{dz}{dx}, -\frac{1}{N} \sum_{i=1}^N \frac{dz}{dy}\right) \quad (1)$$

$$\text{orientation} = \text{atan} \sqrt{\left(\frac{1}{N} \sum_{i=1}^N \frac{dz}{dx}\right)^2 + \left(\frac{1}{N} \sum_{i=1}^N \frac{dz}{dy}\right)^2} \quad (2)$$

356 where *slope* and *orientation* are in radians, N is the number of pixels in each mound, and dz/dx
 357 and dz/dy are the rates of the topographic change in west-east and north-south directions,
 358 respectively. The averaged topographic slope and orientation distribution map of the Ina mounds
 359 shows that the majority of these mounds have area-averaged slopes towards the pit crater center
 360 (Figure S11), supported by observations from contour maps (Figure 6) and cross-sectional
 361 profiles of individual mounds (Figure 7 in Garry et al., 2012 and Figure 7). This orientation
 362 distribution pattern implies that there was a potential tendency for the materials forming the
 363 mounds to flow inward toward the inner lower floor.

364 Six mounds are located in depressions (termed “low mounds”), i.e., terrain units with
 365 smooth textures analogous to those of typical convex mounds on LROC NAC images, and
 366 elevation decreasing towards the margins (similar to the other typical mounds), while abnormally
 367 lower than the surrounding floor terrain. With one exception (#81 in Figure S2) which is
 368 relatively extensive with a maximum length of $\sim 200 \text{ m}$ (Figure 9), the other five “low-mounds”
 369 are rather small, generally shorter than $\sim 50 \text{ m}$ (Figure S12), and also lie within much shallower
 370 ($0.1\text{--}2.5 \text{ m}$ deep) depressions (Table S1).

371 The largest “low mound” is present within an $\sim 200 \times 150$ m, roughly trapezoid-shaped
372 depression (Figure 9a). The bottom (“mound”) is $\sim 100 \times 80$ m in size. Relative to the proximal
373 terrains, this “mound” is typically ~ 7 m deep and has a maximum depth of ~ 10 m at the western
374 margin (Figure 9b, c, e). The slope along the depression wall ranges from $5\text{--}15^\circ$, and increases to
375 $15\text{--}30^\circ$ in limited areas (Figure 9d). This “low mound” is also characterized by convex cross-
376 sectional profiles (Figure 9e), similar to normal uplifted Ina mounds (Figure 7). Locally, the
377 mound surface largely slopes towards the west, with the eastern portion generally 2–3 m higher
378 than the west, and it reaches the highest elevation at the northeast margin, with a maximum relief
379 of nearly 6 m. Topographic moats, several meters wide and up to ~ 1 m deep, are observed to
380 surround the smooth terrains (Figure 9e). The NAC DTM-derived slope of this mound surface is
381 generally flatter than 3° , while the northwest marginal areas show slightly elevated slope ($3\text{--}6^\circ$).

382 The transition area between Ina mounds and the crater floor shows a wide range of
383 morphology and topography (Garry et al., 2012). Parts of the mound margins have clearly
384 defined boundaries with the floor units (Figure 10a), occasionally with topographically lower
385 moats present at the transition region (Figure 10b). Some intervening moats are filled with
386 blocky materials and/or rubble piles (Figure 10c). However, the majority of the mound-floor
387 boundaries are not clearly defined, being instead characterized by gradual morphologic
388 transitions from mounds to finger-like features and pitted units, with complex, multi-branched
389 morphologic patterns (Figure 10d). These small finger-like features extending from the mound
390 margins appear to have similar surface textures to those of the mound terrains, and commonly
391 connect with the lower pitted terrains (Garry et al., 2012). The pitted terrains are composed of
392 ridged or vermicular hillocks up to ~ 1 m high and decameter-scale irregular depressions (Figure
393 10d). In some rare cases, the mounds are spatially continuous with the lower hummocky units,
394 and neither morphologic boundaries nor small finger-like features are observed (Figure 10e). The
395 transitions between the Ina depression wall and floor generally have similar morphologic
396 patterns to the mound-floor transitions, though dominated by clearly-defined geomorphologic
397 boundaries.

398 There are also dozens of unusual depressions (designated as Category 3 depressions in
399 section 3.6) observed on the floor terrains (Figure 11; see discussion of their differences from
400 other depressions within Ina in section 3.6). These depressions are roughly circular to elliptical in
401 shape, and develop a relatively extensive central uplifted structure (Figure 11a, b). Alternatively,
402 they can be described as small domes/mounds surrounded by a ring of topographic moats. The
403 central domes/mounds are clearly different from the internal mound structure of the relatively
404 common “central-mounded” impact craters on the lunar surface (e.g., Bart, 2014). The central
405 structures appear to have similar surface textures to the Ina mounds, while having comparable
406 elevations to the surrounding floor units. In addition, bright boulders are usually present within
407 the marginal ring of topographic lows (Figure 11c). These moat-mound structures share many
408 morphologies similarities with the so-called “ring-moat dome structures” (Zhang et al., 2017).
409 We interpret these unusual central-uplifted structures as possible miniature analogues of Ina
410 mound units, and the marginal ring of lows analogous to the moats frequently occurring along
411 the edges of Ina mounds, where fresh boulders are also often observed (Figure 5c).

412 3.3 Ledge and scarp

413 There are also about a dozen mound structures present at the edge of the Ina interior, which
414 connect the surrounding depression wall and the lower floor terrain (Figure 5). Unlike the typical

415 convex-upward mounds on the central floor, these marginal mounds usually exhibit multiple
416 slope breaks (Figures 8 and 12), permitting us to define the transition region into an inward-
417 facing wall ($5\text{--}10^\circ$ slope), a relatively flat ($<5^\circ$) ledge, a steep ($10\text{--}30^\circ$) inward-facing scarp
418 and the topographically lowest floor, in an inward sequence. The ledges are typically ~ 50 m
419 wide ($\sim 30\text{--}120$ m range), though they are not always well developed in some marginal areas.
420 The inner scarps are typically ~ 50 m wide and ~ 12 m high, with topographic slopes increasing
421 inward and downward and reaching maximum slopes over 30° (Figure 12b). The marginal
422 ledges and scarps delimit the Ina floor terrains; they appear to be the edge of an outer boundary
423 layer, and have comparable topographic slopes to those of the Ina floor units. Among the 15
424 mounds that are connected with the depression walls, 13 of them develop the relatively flat ledge
425 formations, while the other two mounds have very narrow connecting bridges with the
426 surrounding mare shield (Figures 5 and 6).

427 3.4 Floor elevation

428 The Ina floor terrains (including both hummocky and blocky units) are approximately
429 confined between the LROC NAC DTM contours -304 m and -300 m (Figures 5 and 6),
430 indicating that the floor terrain was probably once a hydrostatic surface, for example, a lava-
431 flooded pond surface (Qiao et al., 2017). The floor terrain has a total surface area of ~ 2.28 km²,
432 making up $\sim 50\%$ of the entire Ina interior. Almost all of the floor terrains are spatially
433 connected, except several very small marginal or inter-mound floor units, which are generally
434 smaller than ~ 150 m in dimension (Figure 5b). The elevation of the entire floor terrain ranges
435 from -334 m to -296 m, with a mean value of -316 m ($1\sigma = 7.6$ m; Figures 6 and S13), which is
436 typically up to $\sim 10\text{--}20$ m lower than the proximal mounds (with an average summit elevation
437 of 312 m, $1\sigma = 7.8$ m; Figure S7).

438 The elevation of the floor terrains shows an apparent decreasing trend toward the center of
439 Ina (Figures 6 and 7), and can be broadly categorized as three annular terraces, with ~ 10 m
440 elevation decrements (Figures 6a and S14). The first terrace (Annulus 1, red patches in Figure
441 S14) extends inward to contour -314 m (Figures 6 and S13), the second terrace (Annulus 2, green
442 patches in Figure S14) can be defined between contours -314 m and -324 m (Figures 6 and S13),
443 while the interior-most and lowest areas can be regarded as the third terrace (Annulus 3, blue
444 patches in Figure S14). A part of the boundaries between these terraces seem to be related to
445 surface morphologic features. For instance, the Annuli 1 and 2 boundary near the northeastern
446 edge of Mons Agnes (Figure 5a) is characterized by a stripe-shaped area with apparently
447 elevated slopes ($>10^\circ$, Figure 6c) and a morphologic transition from hummocky terrains (unit H)
448 to highly pitted and ridged terrains (units HPw and R, Figure 13). The existence of multiple
449 annular units within the Ina floor suggests potential multiple stages of surface
450 emplacement/modification processes, for example, lava lake inflation and deflation cycles (Qiao
451 et al., 2017). In addition, the interior mounds appear to occur preferentially at the contacts
452 between the annular terraces (Figure S14), plausibly supporting the formation scenario of Ina
453 mounds by the hypothesized magmatic foam extrusions through the fractures (e.g., caused by the
454 subsidence of the lava lake crust) within the floor terrains proposed by Wilson and Head (2017b)
455 and Qiao et al. (2017).

456 3.5 Hummocky unit

457 Initial examination based on Apollo photographs had already noted the geomorphological
 458 variations within the Ina floor terrains, for instance, the rough-textured units with interlocking
 459 polygonal hummocks and dark hilly units (Strain & El-Baz, 1980). Newly-identified properties
 460 of the floor units include hummocky, pitted, ridged, polygonal and vermicular textures. In
 461 addition, differently-textured surface portions of the Ina floor commonly group with variable
 462 spatial patterns, further complicating the surface geomorphology of the floor terrain. The
 463 intricate combination of various surface textures indicates highly complex geological activities
 464 and emplacement mechanism, and probably intertwinement of products from different surface
 465 processes. We here make a detailed subdivision of the floor terrain into eight geomorphologic
 466 sub-units (Figure 13):

467 (1) **Fine-textured and hummocky units (H)**: These units are composed of relatively
 468 smooth, fine-textured terrains, interspersed with very small (typically <5 m) circular to polygonal
 469 hummocks. These units appear to have the smoothest surface texture (comparable to that of the
 470 mound units) among all the floor terrains, with the least occurrence of topographic pits and
 471 ridges.

472 (2) **Hummocky and moderately pitted units, with closely-spaced pits and ridges (HPc)**:
 473 HPc units are characterized by a hummock-dominated surface texture, while interspersed with
 474 abundant tiny and closely-spaced pits and ridges.

475 (3) **Hummocky and moderately pitted units, with wide-spaced pits and ridges (HPw)**:
 476 HPw units have a similar surface texture to HPc units, but they appear relatively smoother on an
 477 optical image than the HPc units, and the pits and ridges within them are more widely-spaced
 478 (sparse).

479 (4) **Hummocky and highly pitted units (PH)**: PH units are composed of circular or
 480 irregular hummocks, with interspersed abundant tiny pits, thus showing an elevated surface
 481 roughness relative to the above units.

482 (5) **Ridged and pitted units (R)**: These terrains are composed of ridged or vermicular to
 483 polygonal hillocks up to ~1 m high and some decameter-scale irregular depressions, and exhibit
 484 relatively coarser surface textures at longer baselines than hummocky units.

485 (6) **Vermicular units (V)**: Vermicular units are composed of vermicular ridges and inter-
 486 ridge floor materials. These vermicular structures are generally much larger than the more
 487 common ridges within the above (HPc, HPw, PH and R) units. Bright blocky materials are
 488 commonly present within the inter-ridge floors.

489 (7) **Pitted units (P)**: Pitted units are characterized by a hummocky surface texture with
 490 abundant tiny (<5 m long) circular pits. These unusual pits are characterized by preferentially
 491 conical shapes, steep inner walls, and no observed associated floors, elevated rims and
 492 surrounding ejecta, suggesting they may represent locations where surface materials have
 493 drained into the subsurface (see more detailed characterization in section 3.7).

494 (8) **Blocky units (B)**: Blocky units are composed of freshly-exposed boulder fields,
 495 characterized by apparently elevated surface reflectance.

496 3.6 Depressions inside Ina

497 There are various kinds of topographic depressions within Ina. We categorize these
 498 depressions/structures into three major classes according to their morphology, topography,
 499 surface texture, and spatial association with other terrains:

500 **Category 1:** Craters: This category includes both typical bowl-shaped craters interpreted to
 501 be of impact origin (similar to the most common craters on the lunar mare regolith surface), and
 502 unusual, (approximately) circular or sub-circular depressions with observed wall and floor
 503 structures sometimes bounded by a raised rim (for relatively fresh impact craters); these are
 504 interpreted to be poorly-developed and/or highly-modified impact craters (see detailed
 505 characterization in section 3.10).

506 **Category 2:** Regolith pits: These pits are generally very small (<5 m), rimless, without
 507 surrounding ejecta, blocky interior or a detectable floor, and have very steep inner walls (see
 508 detailed characterization in section 3.7). They are interpreted to be regolith drainage pits.

509 **Category 3:** Annular-moat mounds: These depressions are characterized by central
 510 dome/mound structures surrounded by annular moats. The central mounds in the depression
 511 interior seem to have surface textures similar to those of the Ina mounds, while having
 512 comparable elevations to those of the surrounding (pre-emplacment) floor terrain (see section
 513 3.2 and Figure 11). While the central structures are generally much larger than those in the more
 514 common central-mounded craters (e.g., Bart, 2014). These are interpreted to be mound
 515 extrusion-induced surface subsidence depressions.

516 3.7 Pits

517 We have observed abundant pit structures in the Ina interior terrains (Figure 14). These pits
 518 (designated as Category 2 depressions in section 3.6) are generally <5 m in diameter, and have
 519 various map-view shapes, including circular, elliptical, narrow and irregular. There is a host of
 520 unusual morphologic characteristics which distinguishes these pits from impact craters
 521 (including both typical impact craters on the lunar mare and regolith surface, and depressions
 522 within Ina interpreted to be atypical impact craters, see sections 3.6 and 3.10): preferentially
 523 conical shapes, absence of elevated rims and ejecta deposits, steep inner walls, no observed
 524 floors (i.e., like a “hole”), and much greater depth/diameter ratios than for typical lunar impact
 525 craters (e.g., Pike, 1974; Daubar et al., 2014).

526 Most of these pits are observed on the floor units (Figure 14a-d), and very few are located at
 527 the margin of the mounds (Figure 14e, f). Many pits are spatially aligned (Figure 14a-c) or
 528 clustered (Figure 14d). Some aligned pits are nearly spatially connected, and coalesce into linear
 529 troughs (Figure 14a, c, f). High-albedo blocky materials are commonly present within these
 530 aligned pits (Figure 14b, d), implying that the surface regolith may have mostly drained into the
 531 voids below or blown out (Schultz et al., 2006), and shallow subsurface bedrock has been
 532 exposed.

533 3.8 Moats

534 Topographically lower moats along the steep perimeter of Ina mounds are another major
 535 mystery concerning the origin of Ina and other large IMPs (Garry et al., 2012; Qiao et al., 2017;
 536 Figures 8 and 10b). Geomorphological mapping on high-resolution LROC NAC images (~0.5 m
 537 pixel size) shows that moat structures occur at the margins of almost all Ina mounds (Figure 5c),
 538 though some moats might not be well resolved on the relatively lower-resolution NAC DTM

539 topography (2 m/pixel). The width of these topographic moats can range from a few meters to
540 ~13 m, with a typical value of ~5 m. Most of these moat features are generally <1 m deep, while
541 some can reach a maximum depth of ~2 m. The moats occurring along the marginal annulus of
542 the Ina interior commonly occur together with blocky units (Figure 10c), while blocky materials
543 are seldom observed within the central moats (Figure 5c). In addition, we observe no obvious
544 spatial continuity of moats with regolith drainage pits on the floor terrains (see section 3.7).

545 3.9 Blocky unit

546 The apparently optically immature blocky materials within Ina are another major
547 characteristic that has perplexed lunar scientists for decades. In earlier analyses based on
548 relatively coarser resolution Apollo orbital photographs, the blocky units are often described as
549 “bright” or “white” units (El-Baz, 1972; Strain & El-Baz, 1980); sub-meter LROC NAC images
550 show unequivocally that blocky units are basically freshly exposed boulder fields (Garry et al.,
551 2012), with individual boulders reaching ~5 m in dimension; these are, however, much smaller
552 than the largest boulders at Sosigenes, another major IMP occurrence (up to ~12 m, Qiao et al.,
553 2016, 2018a).

554 LROC NAC image-based geological mapping shows that the Ina blocky materials occur
555 dominantly at the marginal annulus of the Ina floor (Figure 5b): within Annulus 1 and close to
556 the contact between Annulus 1 and 2 (Figure S14 and section 3.4), with a small portion of such
557 blocky materials scattered in the topographical moats surrounding the mounds (Figures 5c and
558 10c). In addition, impact cratering on the floor terrains may also expose blocks within craters or
559 eject them to the adjacent floor and mound terrains (see detailed characterization in section 3.10
560 and Figure 15g, h). There are also some individual boulders present within the hummocky units
561 (Figure S12 upper right panel), probably ejected from some distant craters, or exposed *in-situ*.
562 The spatial distribution of the blocky units also corresponds to the areas of least optical maturity
563 (Garry et al., 2013 and Figure 19b) and steepest slopes (Figure 6c), suggesting that they are the
564 most-recently exposed surface materials among the entire Ina interior components.

565 The blocky units in the central portion of the interior of Ina typically have relatively small
566 spatial extents (<~30 m), and relatively smaller sizes of the exposed boulders (Figure 5b), and in
567 some areas, boulders are not well resolved on the half-meter resolution NAC images (in these
568 cases, the identification of blocky units is based on their unusually high albedo and rough surface
569 texture). The blocky units occurring at the marginal annulus of the Ina interior exhibit a much
570 larger spatial extent of fresh boulder fields (up to ~100 m) and relatively higher spatial density
571 and larger sizes of exposed boulders (Figure 8), as evidenced by the unusually great brightness of
572 the marginal portions of the Ina interior (Figure 5a).

573 3.10 Impact craters: geomorphology

574 Based on our careful geomorphologic analyses and comparison with other topographic
575 depressions inside Ina (section 3.6), we interpret these (approximately) circular or sub-circular
576 depressions with observed wall, floor structures and possible raised rim formations (though
577 sometimes relatively less apparent for mature craters), as meteoritic impact craters (designated as
578 Category 1 depressions in section 3.6). These include both typical bowl-shaped craters (Figure
579 15a) and unusual craters (Figure 15c-i) on Ina interior terrains.

580 Most impact craters superposed on the mounds have common bowl-shaped cross-section
581 profiles, similar to the most frequently observed craters elsewhere on the lunar surface. Nearly

582 all the mound craters, even the fresh-appearance ones (as evidenced by their sharp rims, Figure
583 15a), do not exhibit a blocky interior, or associated surrounding ejecta fields, halos and ray
584 patterns. These craters seem to be different from their counterparts on typical mare regions
585 (Figure 15b), suggesting that the mound craters probably degraded very quickly, or that they may
586 represent impacts into unconsolidated materials, e.g., solidified magmatic foams (Wilson &
587 Head, 2017b; Qiao et al., 2017).

588 However, impact craters identified on the floor terrains show a wide range of morphologies,
589 often very complex, and are significantly different from those on both the mound units and
590 surrounding mare regions. Almost none of the floor craters have typical bowl-shaped profiles; in
591 contrast, they are generally characterized by relatively shallow floors and irregular interior
592 structures (compared with their counterparts on Ina mounds and the surrounding mare; Figure
593 15c-f), suggesting that these craters are poorly formed, highly modified and/or may represent
594 impact into unusual targets other than typical lava flows or regolith materials, for example,
595 impact cratering into highly-porous targets (Figure 2 of Housen et al., 1999; Figure 8 of Housen
596 & Holsapple, 2003). In addition, exterior ejecta materials, blocky interior structures, and ray or
597 halo patterns are generally not observed to be associated with these craters, even for those with
598 relatively sharp rims (Figure 15d). Some of the floor craters display concentric and central-
599 mounded interior structures (Figure 15e, f), which are very different from those of fresh craters
600 formed on layered targets (typically with an unconsolidated layer overlain on a more cohesive
601 layer, Bart, 2014). However, several craters on the floor terrains have developed a variable extent
602 of boulder fields in both the crater interior and exterior (Figure 15g, h), indicating that these
603 impacts have penetrated the unconsolidated surface materials (commonly lunar regolith) and
604 excavated the underlying blocky materials. Based on the measured diameters (as small as ~20 m)
605 and the scaling law between crater diameter and excavation depth (Melosh, 1989), the thickness
606 of the surface regolith accumulated on the floor units can be roughly constrained to be $< \sim 1.7$ m
607 (consistent with the 10–15 cm regolith thickness lower limit value reported by Elder et al. (2016,
608 2017)).

609 There are also some impact craters occurring at the boundaries between the mounds and
610 floor terrains (Figure 15i). The morphology of a crater of this kind shows significant differences
611 between the part on the mound and the other part on the floor: the mound part is relatively well-
612 developed, resembling the bowl-shaped craters entirely formed on the mounds (Figure 15a),
613 while the typical crater morphologies (including wall, floor, rim, etc.) on the floor part are hardly
614 visible. This morphological discrepancy strongly indicates the fundamental differences in target
615 properties between the mounds and floor terrains and the effects they exert on crater formation
616 and subsequent degradation: the craters on the floor either are poorly developed or degrade
617 rapidly compared with their counterparts on the mounds.

618 3.11 Impact craters: size-frequency distributions

619 In addition to their morphological peculiarities (section 3.10), the impact craters within the
620 interior of Ina are also distinctive and unusual in their remarkably low areal density, suggesting a
621 33.2 Ma model age for the mounds through a crater population study on LROC NAC imagery
622 data (Braden et al., 2014). To investigate the detailed nature of and potential causes responsible
623 for the extreme paucity of superposed impact craters on the Ina mounds, we performed a careful
624 crater counting analysis (for craters ≥ 10 m in diameter) using LROC NAC images with a range
625 of illumination geometries (solar incidence angle up to 87° ; Figure 16). Moreover, due to the

626 highly complicated surface textures and unusual crater morphologies of the floor terrain, the
627 impact crater size frequency distributions of the floor units and how they compare with those of
628 other adjacent terrains, are both poorly understood and remain controversial (cf. Robinson et al.,
629 2010b; Braden, 2013; Braden et al., 2014). Based on our analyses of the morphological
630 characteristics and recognition criteria of the atypical impact craters superposed on the floor
631 terrain (section 3.10), we here also identify and measure all impact craters ≥ 10 m in diameter on
632 the Ina floor units using LROC NAC images (Figure 16a). For comparison, we also transfer the
633 map of the Ina interior units to the upper flank of the shield volcano and count the superposed
634 impact craters there (Figure 16b). During the crater counting investigations, special care has been
635 taken to eliminate contamination by secondary impact craters and endogenous pits according to
636 their morphologic characteristics (e.g., Shoemaker, 1962; Oberbeck & Morrison, 1974; Head &
637 Wilson, 2017). The crater counting results are mapped in Figure 16a,b and reported in the
638 standard cumulative SFD plots (Figure 16c) and tabular form (Table 1).

639 We identify 542 impact craters ≥ 10 m in diameter on the Ina mounds, which is more than
640 twice the number (i.e., 232) reported by Braden et al. (2014). The cumulative SFD of these
641 mound impact craters (Figure 16c) does not show clear evidence of a crater population in the
642 equilibrium state (e.g., Xiao & Werner, 2015). Fitting of these mound impact craters using the
643 Neukum lunar CF and PF produces an absolute model age of 59 ± 3 Ma, compared with 33.2 ± 2
644 Ma of Braden et al. (2014). For the floor units, 378 impact craters ≥ 10 m in diameter are
645 counted, $\sim 30\%$ less than on the mounds with an identical surface area. The cumulative SFD
646 demonstrates that the floor craters are almost indistinguishable from the mounds craters, while
647 subtle discrepancies are also observed: (1) for craters $\leq \sim 14$ m, the cumulative crater density on
648 the mounds is slightly higher than that on the floor; (2) for craters ~ 14 – ~ 30 m in diameter, the
649 reverse trend is observed; (3) for the ~ 30 – ~ 50 m diameter range, the cumulative crater density on
650 the two interior units closely overlap; (4) for craters $\geq \sim 50$ m in diameter, the floor units exceed
651 the mounds in cumulative crater density again, though in this diameter range a very limited
652 number of craters are counted (Table 1). Fitting of the floor craters ≥ 10 m in diameter yields a
653 model age of 48 ± 2 Ma, slightly younger than that of the Ina mounds.

654 Compared with the surrounding ancient shield volcano flank (Table 1 and Figure 16c), the
655 Ina interior records much fewer superposed impact craters, especially for craters in the greater
656 diameter ranges: for craters ≤ 20 m, the crater density in the Ina interior is generally about $1/4$ –
657 $1/3$ of that of the surrounding shield, while for craters ≥ 20 m, the Ina interior crater density is
658 less than $1/5$ of the outside mare shield surface density. We also note that the crater population of
659 the surrounding shield is in equilibrium for diameters $\leq \sim 220$ m (section 2.2), which indicates that
660 the observable impact crater record is incomplete rather than representing what actually
661 accumulated.

662 The Ina mounds are characterized by a wide range of surface slopes (Figure 6c). We also
663 investigate the potential effect of topographic slopes on the observed surface impact crater
664 density at variable diameter ranges. Several patchy areas with representative topographic slopes
665 ($< 3^\circ$, 3 – 6° and $> 6^\circ$, derived from NAC DTM, Figure S15) were selected from the relatively
666 areally extensive Ina mounds, and their superposed impact crater SFDs are plotted as standard R-
667 values at three diameter bins (Figure 17 and Table S2; calculated using the technique
668 recommended by the Crater Analysis Techniques Working Group (1979)), and compared with
669 the surrounding shield flank (patches with same areas and shapes as the Ina mounds shown in
670 Figure 16b). The results clearly show a correlation between crater densities and topographic

671 slopes: (1) the crater density generally decreases with increasing slopes, implying smaller craters
672 on steeper sloped-surface are relatively poorly preserved, probably due to being destroyed by
673 surface degradation processes, for instance, regolith creep process (Xiao et al., 2013); (2)
674 relatively larger craters show relatively less reduction of crater densities, or even slightly
675 increased crater density on steeper slopes, suggesting larger craters are probably more resistant to
676 slope erasure effect; (3) the surrounding ancient shield region ($3.1 \pm 2.7^\circ$ slope) exhibits a
677 significantly higher crater density than Ina interior mound portions with comparable slopes.

678 The multiple annular terrace pattern of the Ina interior floor, with decreasing elevations
679 towards the central portion (Figures 6a and S14), suggests potential multi-phase
680 emplacement/modification processes (section 3.4), which may have an effect on the preserved
681 impact crater populations. To explore this issue, we compare the SFD of impact craters
682 superposed on the three floor annuli (Figure S16). It shows: (1) the innermost annulus (Annulus
683 3) has a relatively higher cumulative crater density than the outer two annuli for craters $\leq \sim 18$ m
684 in diameter; (2) the outermost annulus (Annulus 1) has a comparable cumulative crater density to
685 the middle annulus (Annulus 2) for craters $\leq \sim 13.5$ m in diameter, and shows a slightly elevated
686 cumulative crater density at greater diameters and reaches a comparable level with the innermost
687 annulus; (3) at the $\geq \sim 25$ m diameter range, the cumulative crater SFD of the three annuli closely
688 overlap. Our formation model suggests that the multiple annuli of the Ina floor were formed
689 contemporaneously (section 4.1), and the floor generally has a very flat slope (so no obvious
690 slope effect), and the superposed CSFD are predicted to be comparable, as observed here.

691 3.12 Floor topography and slopes

692 We use the NAC DTM-derived slope map (Figure 6c, 2 m pixel size, with a baseline of 6
693 m) to characterize the topographic slopes of the interior of Ina and associated geomorphologic
694 units (details can be found in Text S2 and Figures S17-19 in the supporting information). Slope-
695 frequency distribution investigations show the mounds and hummocky units have similar most-
696 frequent slopes ($2\text{--}5^\circ$) to the entire Ina interior; the mounds, however, have many more (areal
697 percentage) areas with slopes over $>7^\circ$ than the hummocky units. We suggest that this can be
698 explained by the slope baseline effect: most of the surface reliefs of the hummocky units are
699 shorter than the slope baseline (6 m), while the convex upward profile, relatively extensive
700 (commonly wider than ~ 10 m), steep marginal scarps of the mounds can significantly elevate
701 their average slope. The blocky units and the moats have relatively clustered most-frequent
702 slopes ($3\text{--}4^\circ$), while the moats have more areas with slopes steeper than 8° ; this can be again
703 caused by the slope baseline effect.

704 3.13 Regolith thickness

705 Small fresh impact craters on the lunar surface have been observed to develop variable
706 interior structures ranging from normal bowl-shaped craters to abnormal craters with special
707 interior structures (e.g., concentric ring, flat bottom and central mound). These crater interior
708 morphology variations are interpreted to represent meteoritic impacts into layered targets with an
709 unconsolidated surface layer (commonly lunar regolith) underlain by a more cohesive substrate
710 (e.g., basaltic bedrock). The morphology and size of the craters are correlated with the contrast
711 between crater diameter and the thickness of the surface unconsolidated materials (e.g.,
712 Oberbeck & Quaide, 1967). Measurements of the rim-to-rim diameter and size of the interior
713 structure of these abnormal craters provide a quantitative method to estimate the surface regolith

714 thickness for typical lunar mare-regolith surfaces (see the methodology in Bart, 2014). For the
715 shield volcano flank surrounding the Ina pit crater, 87 abnormal craters are identified and
716 measured, which give a median regolith thickness of 4.8 m (1.3 – 11.0 m range with $1\sigma = 2.3$ m,
717 Figure 18). For the Ina mounds, we identify 10 such abnormal craters, and obtain an estimated
718 median regolith thickness of 2.1 m (1.0 – 7.6 m range with $1\sigma = 2.0$ m). Within one of the largest
719 Ina mounds (Mons Agnes), the estimated regolith thickness shows a trend of becoming thin
720 towards the margins (four abnormal crater measurements), accompanied by increased
721 topographic slopes. We note that this regolith thickness estimation method is based on the
722 assumption of impacts into a typical mare regolith target; impacts into highly-porous targets, as
723 suggested by Wilson and Head (2017b) and Qiao et al. (2017) for the Ina mounds, may introduce
724 a different cratering manifestation. For example, these abnormal craters may represent impacts
725 into a different set of layered targets other than typical basalt-mare targets, for instance, the
726 hypothesized magmatic foam extrusions superposed on a solidified lava lake crust (Qiao et al.,
727 2017 and section 4.1); in these cases, these craters many have penetrated about the depth of the
728 mound height and sampled the underlying bedrock, and the calculated thickness may be related
729 to the magmatic foam thickness.

730 Blocky craters, i.e., craters with exposed blocky materials within the crater interior and/or in
731 the surrounding exterior, provide another method to constrain the surface regolith thickness: the
732 excavation depth of these blocky craters should exceed the surface regolith thickness. Several
733 blocky craters as small as ~20 m are observed on the Ina floor terrains, thus the floor surface
734 regolith materials can be constrained to be thinner than the excavation depth of these craters, i.e.,
735 ~1.7 m (see section 3.10 and Figure 15g, h). Moreover, no confirmed blocky craters have been
736 observed on the Ina mounds (see section 3.10). Our estimation of the surface regolith thickness
737 of Ina interior is consistent with the 10–15 cm lower limit value reported by LRO Diviner
738 thermophysical measurements (Elder et al., 2016, 2017).

739 3.14 Optical reflectivity and maturity

740 One of the most enigmatic characteristics of Ina pit crater is its anomalously high
741 reflectivity and optical immaturity, especially for the interior floor rubble materials (Strain & El-
742 Baz, 1980; Schultz et al., 2006; Staid et al. 2011; Garry et al., 2013; Bennett et al. 2015). To
743 explore the nature and potential origin of these uncommon optical properties, we here present an
744 updated characterization the reflectance of Ina and its adjacent area at 750 nm and their optical
745 maturity (OMAT) using the high-resolution imaging spectrometer data obtained by the Kaguya
746 Multiband Imager (MI) (Figures 19, 20 and Table S3; details can be found in Text S3 in the
747 supporting information). Reflectance mapping shows that 1) the Ina mounds have comparable
748 (or slightly elevated) visible reflectance to the surrounding mare, 2) the floor blocky materials
749 are much more reflective (Figure 19a and Table S3) and 3) the Ina floor hummocky units show
750 apparent reflectance variations: areally extensive hummocky terrains at the eastern marginal
751 floor with abnormally low 750 nm reflectance and other smaller hummocky units with relatively
752 elevated reflectance (Garry et al., 2013; Figure 19 and Table S3); these brightness variations are
753 probably due to occurrence of (sub-resolution) blocky materials. OMAT investigations (Figure
754 19b and Table S3) reveal that the entire Ina interior is generally optically more immature than the
755 surrounding mare, while displaying noticeable differences in various interior terrains: (1) the
756 mounds are slightly more immature than the surrounding mare shield; (2) the blocky units are the
757 most immature materials in the local regions within and surrounding Ina; (3) hummocky units
758 have OMAT measurements between those of the Ina mounds and the blocky units; (4) the two

759 different sub-types of hummocky units (“dark” and “bright”) exhibit indistinguishable OMAT
760 values, suggesting they may have been emplaced contemporaneously. Spectroscopic analysis
761 (Figure 20) shows (1) the Ina interior is mainly composed of high-titanium basalt; (2) the
762 brighter portion of the Ina hummocky units shares similar optical alteration path with Ina
763 mounds, while may have been subject to different optical maturation processes from the blocky
764 units and the darker hummocky units.

765 4. Discussion

766 4.1 Interpreted formation mechanism of Ina shield volcano summit pit crater

767 On the basis of 1) our latest physical volcanology analysis of lunar dike evolution processes
768 and final-stage shield-building eruptions (Wilson & Head, 2017a; Head & Wilson, 2017), 2)
769 analog studies of the morphology, topography and magmatic-volcanic processes of terrestrial
770 small shield volcanoes in Hawai'i (Qiao et al., 2017 and Figure 21), and 3) following our
771 comprehensive geological characterization of the context and interior of Ina pit crater presented
772 above (sections 2 and 3) and prior investigations (e.g., Strain & El-Baz, 1980; Garry et al., 2012;
773 Braden et al., 2014; Qiao et al., 2017), we examine the Ina feature in the context of lunar shield-
774 building eruptions. We begin with the crucial observation and interpretation that the Ina feature
775 is a summit pit crater/vent atop a ca. 22 km diameter, ~3.5 Ga old shield volcano (Strain & El-
776 Baz, 1980; Qiao et al., 2017), and then examine the successive phases of a lunar shield-building
777 eruptions (Wilson & Head, 2017b), with a special focus on final-stage summit pit crater
778 activities. We interpret the wide range of characteristics associated with the Ina feature as being
779 consistent with a two-component model of origin as a partially-drained summit pit crater lava
780 lake atop an ancient shield volcano (“hummocky floor model”), accompanied by the waning-
781 stage extrusion of highly gas-rich magmatic foam materials (“mound foam model”) (Qiao et al.
782 2017; Wilson & Head, 2017b).

783 New theoretical and observational treatments of lunar magmatic-volcanic and gas production
784 processes (Rutherford et al. 2017; Wilson & Head, 2018) provide important evidence that lunar
785 small shield volcanoes, like the one containing the Ina pit crater, are formed through eruptions
786 fed by a single dike sourced deep in the upper mantle. Wilson and Head (2018) synthesized
787 recent developments in understanding the origins and volatile contents of lunar magmas, the
788 mechanisms that transferred magma to the surface, and the factors that controlled the eruption
789 style of the resulting volcanism, with emphasis on the effects of volatile formation and release.
790 Assessment of mare basalt gas release patterns during individual eruptions (Rutherford et al.,
791 2017) provides the basis for predicting the effect of vesiculation processes on the structure and
792 morphology of associated features. Using these data, Wilson and Head (2018) subdivided typical
793 lunar eruptions into four phases: *Phase 1*, dike penetrates to the surface, transient gas release
794 phase; *Phase 2*, dike base still rising, high flux hawaiian eruptive phase; *Phase 3*, dike
795 equilibration, lower flux hawaiian to strombolian transition phase; and *Phase 4*, dike closing,
796 strombolian vesicular flow phase. They showed how these four phases of mare basalt volatile
797 release, together with total dike volumes, initial magma volatile content, vent configuration and
798 magma discharge rate, can help relate the wide range of apparently disparate lunar volcanic
799 features to a common set of eruption processes and help place small shield volcanoes and their
800 summit pit craters into this context. Specifically, Wilson and Head (2018) showed that small
801 shield volcanoes can consist of Phase 2 lavas erupted from dikes that have a relatively small
802 volume, so that neither the erupted volume nor the volume flux are large. Overflows from the

803 lava lake around the vent are fed at a low eruption volume flux; the resulting lava flows travel
804 ~5–15 km before stopping due to cooling, successively forming the shield. Subsequent Phase 3/4
805 activity builds additional features at the summit of the volcano, including summit pit craters.
806 Summit pit craters and lava lakes may also be the result of Phase 4a activity in the latter stages of
807 typical eruptions; as the rise rate wanes and volatile exsolution is optimized, very vesicular
808 magma from the dike is emplaced under a cooling crust on the lava lake above the vent.

809 In summary, shield-building eruptions are predicted to occur when the magma volume flux
810 in the upwelling dike is sufficient to penetrate to the surface, while still too low to cause typical
811 mare basin-filling eruptions (Wilson & Head, 2017a), or at the end, in the waning stages of the
812 fourth phase of the typical eruption sequence (Wilson & Head, 2018). In the course of the dike
813 approaching the surface, volatile phases within the magma would continuously exsolve due to
814 pressure release, generating abundant gas bubbles (mainly CO and H₂O; Figure S20a).
815 Expansion of the bubble-rich magma into the lunar hard vacuum would ensure that the Ina
816 shield-building eruptions began with vigorous fountain activities, ejecting abundant pyroclastics
817 beyond the vent (Figure S20b); some of them would deposit on a growing crater rim surrounding
818 the vent, in a similar style with many terrestrial eruptions, for instance, the 1961 effusive
819 eruptions at the Halema'uma'u crater (Richter et al., 1964; Dzurisin et al. 1984).

820 The building of the small Ina shield volcano is dominated by the accumulation of low
821 effusion-rate, cooling-limited flows (Figure S20c). The measured size, height and estimated ~0.6
822 km³ volume of the Ina shield volcano are at the upper end of values for more than 300 small
823 mare shields identified on the Moon (Head & Gifford, 1980; Tye & Head, 2013), indicating that
824 it is formed by relatively longer flows (up to ~12 km) through lengthy eruptions. On the basis of
825 the topographic slopes of the Ina shield flanks (averagely ~1.7°) and observations of
826 southwestern Imbrium flows (Schaber et al., 1976), the thickness of individual flows can be
827 estimated as ~1 m. Assuming an ~1–2 km width of individual flows, calculations based on the
828 parameter relation for channelized flows (Wilson & Head, 2017a) yields an estimated magma
829 extrusion volume flux of ~225–450 m³/s. Thus, the building of the Ina small shield is predicted
830 to have operated over a period of ~3–6 months (assuming an uninterrupted emplacement
831 activity). Spectroscopic examination of shield deposits excavated by fresh small craters indicates
832 that the erupted magma shows inhomogeneities in titanium abundance (section 2.1 and Figure
833 2d): flows emplaced earlier are more titanium-rich than the last flows deposited on the surface.

834 The final-stages of a small shield-building eruption are characterized by a series of
835 important summit pit activities, significantly different from normal mare basalt flow eruptions
836 (Head & Wilson, 2017; Wilson & Head, 2017b). As observed in the late-stages of terrestrial
837 shield-building eruptions, fountain activities at the Ina shield volcano diminished gradually;
838 decrease in magma rise rate would allow gas bubble production and rise, bubble coalescence,
839 and the onset of a strombolian phase of activity in the pit crater lava pond. Cycles of lava
840 drainage and refilling, along with gas-piston activities, caused the lava lake surface to fluctuate
841 frequently. During the waning part of this period, the lava lake surface began to cool and
842 solidify, developing a platy, meters-thick solidified crust forming the thermal boundary layer
843 (TBL) of the summit pit crater lava lake. Cooling of the lava lake is predicted to be more
844 efficient in the shallower marginal parts of the lake in contact with the relatively chilled
845 surroundings, and less efficient over the deeper part above the source vent. During lava lake
846 inflation and deflation cycles, the magma continuously degassed, strombolian ejecta was
847 emplaced on the cooling lava lake crust, and bubbles and foams accumulated below the lava

848 pond crust; during the deflation episodes, the lava lake crust foundered and tilted towards the
849 interior multiple times, generating multiple terrace patterns within the lava crust. The relatively
850 chilled marginal portion of the crust, welded to the crater wall, became very brittle. During crust
851 subsidence, the tensile stress operating on the marginal crust would cause it to fracture and
852 separate from the central part of the lava crust, leaving steep-sided ledge structures at the base of
853 pit crater wall. Also during the lava lake deflation, the surface crust was locally cracked and
854 deformed into small polygonal plates and pressure ridges. Lava and magmatic foams oozed from
855 these surface cracks, flowed sluggishly on the crust surface and covered previous pressure ridges
856 and cones, leaving them as isolated islands/hummocks (kipukas). In the waning eruption stage,
857 the lava lake became increasingly stagnant; the dominant activities were sporadic small
858 strombolian and related gas-release events forming pits and linear fissures.

859 On the basis of the nature of the lava lake crust development and lava drainage and crust
860 deflation, we would expect significant void space to exist below the pristine surface of the
861 deflated and draped crust. Thermal calculations show that a 1 m thick boundary layer will
862 develop on a lunar lava lake within the first 4 days, growing to a two-meter thick crust in less
863 than a month (Wilson & Head, 2017a), periods of time well within the observed duration of lava
864 lake formation and drainage in terrestrial shield pit craters. These thicknesses are more than
865 sufficient to cause local bending and breaking of the crust upon lake drainage to produce
866 pressure ridges of tilted and imbricated plates, as well as roofs and arches over drained
867 subsurface lava tubes (Wilson & Head, 2017b). More importantly, all these complex activities
868 during the lava lake process, including lava drainage, inflation and deflation, squeeze-ups,
869 sporadic gas venting, and volume decrease due to thermal contraction and solidification, would
870 together make the lava lake floor highly porous, containing abundant macro- and micro-
871 vesicularity and open void spaces. Indeed, this is seen in surface investigations of and drill cores
872 from the Kīlauea Iki lava lake floor: 10-40% vesicles were observed in the upper 10 m of lava
873 lake crust (Figure 21; Richter & Moore, 1966; Mangan & Helz, 1986), and vesicles were likely
874 to be considerably larger in the lunar environment (Head & Wilson, 2017). For a lava lake of
875 ~30 m thickness, these processes could readily produce at least 10–20% sub-crustal void space.

876 In the latest stage of the shield-building volcanic process, the overpressure in the dike has
877 been finally exhausted and no more magma will ascend; this marks the ending of the shield-
878 building activity and the transition of eruption style towards a strombolian explosive phase
879 (Wilson & Head, 2017b; Figure S20d) with minor explosions through the lake surface above the
880 widest part of the dike. The final volatile production at shallows depths is dominated by the
881 release of water vapor, with bubbles rising buoyantly and accumulating at the tip of the magma
882 column, just below the TBL (Wilson & Head, 2017b; Figure S20e). The typical water content
883 (several hundred ppm) for lunar basaltic magma (Saal et al., 2008; Harui et al., 2011, 2015),
884 combined with the near-zero magma ascent rate and the likely high bubble number density from
885 abundant nucleation sites, would ensure that these gas bubbles are so small (~20 μm radius,
886 Wilson & Head, 2017b) that the surface tension forces allow them to remain stable against the
887 internal gas pressures and so to form a stable magmatic foam layer. This foam layer can extend
888 several hundred meters downward and reach an extreme vesicularity up to ~95% (Wilson &
889 Head, 2017b; Qiao et al., 2017). The final stages of dike stress relaxation and closure would
890 squeeze the magmatic foams upward very slowly (~10 mm/s), causing them to extrude to the
891 surface through cracks in the TBL to produce the bleb-like mounds (Wilson & Head, 2017b;
892 Qiao et al., 2017; Figures S20f and S21).

893 The availability of high-resolution topographic and imaging data from LROC NAC permits
894 the rheological modeling of the emplacement of magmatic foam lavas, which shows that
895 magmatic foam extrusion proceeds at a very low effusion rate ($\sim 0.6 \text{ m}^3/\text{s}$), with the majority of
896 the Ina mounds being emplaced over a period of several hours to several days (Wilson & Head,
897 2017b). The unusually high foam viscosity and low effusion rate would inhibit the lateral motion
898 of foam lava flows, enhancing their convex shapes and steep edges, in a similar style to the
899 building of highly silicic domes on the Earth and the Moon (e.g., Wilson & Head, 2003). The
900 final-stage of dike closure would involve solidification of magma against the dike walls and
901 consequent shrinkage, resulting in drainage of residual lava from the bottom of the lake,
902 deformation of the lava lake crust, and final floor subsidence. Mass load of magmatic foam
903 extrusions and the large void spaces left underlying the lava lake crust due to magma foam
904 extrusion enhance the deformation and subsidence of the adjacent local lava lake crust (see the
905 detailed crust subsidence mechanism in Wilson & Head, 2017b), further ensuring the steep sides
906 of the mounds and generating topographic moats around the mound margins (Qiao et al., 2017;
907 Figure S21). Occasionally, the vertical displacement of local lake crust subsidence may exceed
908 the building height of the extruded foamy mounds, which, consequently, generates the observed
909 “low mounds” (section 3.2). Topographic and morphometric characterizations of all the “low
910 mounds” ($n=6$) show the vertical displacement of local lake crust is generally less than $\sim 1\text{--}2 \text{ m}$,
911 and can be as deep as $\sim 10 \text{ m}$ at the largest “low mound” (Figure 9). Though occurrence of these
912 “low mounds” are much less frequent than the common raised mounds, it is very likely that local
913 lava lake crust subsidence due to upward extrusion of foamy magma would be an important
914 process, which would in part account for the inward lowering of the Ina floor topography
915 (section 3.4). It is predicted that gas bubbles in the top of the emplaced foam will explode in the
916 hard vacuum, producing a layer of low-density (compared to basaltic lava flows), very fine
917 regolith. The mass loading of these surface regolith and radiative cooling of the foam lava flows
918 will protect the extruded foamy lava from further disruption.

919 The interpreted magmatic foam substrate of Ina floor mounds is supported by a line of
920 observations: (1) the unusual morphologies of superposed impact craters, including general non-
921 blocky crater interior and no associated radial ray patterns (section 3.10), (2) much lower density
922 of superposed impact craters compared with the surrounding mare (interpreted to be due to the
923 crater diameter decrease effect of impact into a highly porous target (section 3.11) and (3)
924 Diviner thermophysical mapping results, which show that Ina mound materials are less
925 consolidated or contain fewer small rock fragments than typical mare regolith (Elder et al., 2017).

926 Thus, in this waning-stage two-component, lava lake process and magmatic foam extrusion,
927 scenario (Qiao et al., 2017), the various terrains associated with Ina are interpreted to have
928 formed in the terminal phases of the shield-building activity (Wilson & Head, 2017b; Figure
929 S20), contemporaneous with the adjacent mare basalt lava eruptive phase more than three billion
930 years ago. The narrow collar surrounding Ina (section 3.1 and Figure 3 in Garry et al., 2012) is
931 interpreted to be the remnant of lava lake filling and overflow, together with possible
932 pyroclastics. The basal terrace/ledge and steep inward-facing scarp at the base of the interior
933 walls of Ina (section 3.3) are analogous to the chilled margin of a lava lake remaining after lava
934 lake deflation and/or recession, which are embayed and overridden by subsequent magmatic
935 foam extrusions near the floor edge. The topographically low floor terrains (section 3.5 and
936 Figure 13) are analogous to the solidified lava lake crust, and each of their complex topographic
937 and morphologic characteristics corresponds to the various activities operating during the lava
938 lake process: 1) the three-stage annular, inwardly lower topography of the floor (section 3.4) is

939 interpreted to be formed through lava lake crust foundering and tilting towards the interior
940 portion during the final magma retreat, lava lake deflation episodes and subsequent upward
941 extrusion of foamy magma; 2) the hummocky textures (section 3.5 and Figure 13) are analogous
942 to lava lake inflation, lake crust flexure, bending, fracturing and ridge formation; 3) the abundant
943 pits (section 3.7) are analogous to degassing pits (enhanced by the lunar vacuum), late-stage
944 sporadic lava fountains and subsequent regolith drainage through infiltration pits into porous
945 macro-vesicular lava lake crust and void space below; 4) the linear depressions/fractures
946 (sections 3.6 and 3.7) are interpreted to be modified cracks in the lava lake surface formed by
947 flexure, cooling and shrinkage during lava lake deflation and deformation; 5) the polygonal
948 patterns are analogous to highly deformed and cracked lava lake crust; 6) the vermicular patterns
949 (section 3.5 and Figure 13) are analogous to tilted lava lake crust; 7) ridged textures are
950 interpreted to be locally deformed lava lake surface crust; 8) the floor blocky units (section 3.9)
951 are analogous to exposed blocks of the solidified lava lake crust (either exposed instantaneously
952 or subsequently by subsequent meteoritic impacts and regolith infiltration). In addition, the
953 various morphologies from these complicated lava lake activities often intricately interweaved,
954 producing the highly diversified surface textures of the Ina floor terrains (section 3.5 and Figure
955 13). The bleb-like mounds (section 3.2) are interpreted to be the solidified magmatic foam
956 extrusions, and the topographically lower moats surrounding the mounds (section 3.8) are
957 formed through the subsidence of local lava lake crust to conserve volume. The several “low
958 mounds” (section 3.2) are interpreted to be explained by the much greater vertical displacement
959 of the local crust during subsidence, which exceeds the height of the extruded mounds, making it
960 lower than the pre-emplacement lava lake crust floor. The preferential occurrences of mounds at
961 the contacts between floor annular terraces is interpreted as the extrusion of magmatic foam
962 through the lava lake crust fractures caused by its inward subsidence. These interpretations and
963 predictions can be tested with future observations, measurements and missions (see section 5).

964 The final stage of formation of lunar shield volcanoes, summit pit craters and lava lakes
965 involves cooling and solidification processes. As magma supply wanes and dike closure
966 processes reach equilibrium (Wilson & Head, 2018), any remaining advective magmatic heat in
967 the dike or lava lake is transferred by conduction to the surrounding country rocks over
968 geologically rapid time scales ($\sim 10^2$ - 10^3 years) (Wilson & Head, 1981, 2017a, 2018; Richter &
969 Moore, 1966; Wright et al, 1976; Hardee, 1980). Subsequent, separate dike intrusion events from
970 the same very deep diapiric magmatic source region are possible during the source region
971 lifetime (Wilson & Head, 2017a). However, 1) the repose time between eruptions is predicted to
972 be much longer than the cooling time of the initial dike (Wilson & Head, 2017a), and 2) a second
973 dike propagated from the same source at several hundred kilometers depth is very unlikely to
974 reach the surface at exactly the same $\sim 2 \times 3$ km location as the Ina summit pit crater; in fact the
975 solidification of the dike is predicted to change the local stress field sufficiently that it virtually
976 precludes the reoccupation of the Ina summit pit crater by a later dike (Head & Wilson, 2017).
977 These same considerations place severe constraints on the likelihood of a dike originating from
978 the lunar mantle over three billion years later (< 100 Ma ago) and erupting in the exact position of
979 the very small (~ 2 - 3 km) Ina summit pit crater on an ancient shield volcano.

980 Once the lava lake has solidified, how will the unique eruption products, formed during the
981 waning-stage of shield-building activity (i.e., subsided macro-vesicular and micro-vesicular lava
982 lake crust superposed by numerous solidified magmatic foam extrusions), respond to the
983 subsequent, billions-of-years of continuous geologic modification by regolith forming
984 bombardment processes?

985 4.2 Post-emplacement geologic modifications

986 Our two-component model for Ina formation is predicted to have occurred more than 3 Ga
987 ago, contemporaneous with the adjacent mare deposit emplacement. Subsequent to this time,
988 geological modification process, including impact cratering, optical maturation, regolith
989 development and topographic degradation, should have operated on all surfaces equally (mare,
990 shield, and Ina mounds and hummocky/blocky terrains). How can the geomorphological
991 crispness, optical immaturity and anomalously young crater retention ages of the Ina interior be
992 explained? The unique substrate nature of the Ina interior, solidified magmatic foam mounds
993 with bulk porosity up to ~95% and chilled lava lake crust floor with abundant micro-vesicularity
994 and large void space, provides an insight.

995 4.2.1 Impact cratering

996 Meteoritic impact is arguably the most important geological modification process on the
997 Moon, continuously operating everywhere on the lunar surface. On typical mare surfaces
998 including the flanks of Ina shield volcano (solid basaltic lava flows), when a meteoritic impactor
999 strikes the lunar surface substrate, its kinetic energy is focused on deforming, fracturing,
1000 comminuting, excavating and ejecting the target materials, leading to the formation of well-
1001 developed, bowl-shaped, relatively shallow, blocky craters, with lateral blocky ejecta deposited
1002 several radii outward and finer particles ejected further (Wilson & Head, 2017b; Figure S22a).
1003 Impacts into the micro- and macro-vesicular Ina lava lake crust floor, however, are predicted to
1004 operate dominantly through the compaction and crushing of the substrate, which is extremely
1005 porous at diverse scales, disruption of vesicle walls, and excavation of the blocky portions of the
1006 crust substrate (Qiao et al., 2017; Wilson & Head, 2017b; Figure S22b). As the chilled lake crust
1007 floor already consists of abundant large (decimeter to meter scales) open void spaces, a large
1008 portion of the impact crushed and excavated substrate debris will preferentially sift into the
1009 abundant substrate macro-vesicularity. This infiltration process is assisted by continual seismic
1010 shaking activities caused by the multiple subsequent impacts. In consequence, craters on the Ina
1011 hummocky floor are poorly developed, filled with crushed rubble, abnormally-shaped, difficult
1012 to identify and degrade rapidly, and show a deficit of larger craters; lateral ejecta emplacement is
1013 highly inhibited; continuous sifting into the porous substrate enhances the volume loss of surface
1014 particles and exposure of subsurface blocks (Figure S22b; Wilson & Head 2017b).

1015 Impacts into the solid magmatic foam of the Ina mounds are proposed to proceed by a
1016 different mechanism (Qiao et al., 2017; Wilson & Head, 2017b; Figure S22c). The Ina mounds
1017 are composed of abundant tiny vesicles with an extremely high porosity, up to ~95%. Kinetic
1018 energy of the meteoritic impacts will mainly be consumed in permanent compressing, crushing,
1019 shattering and penetrating the foam vesicles (the aerogel effect; Wilson & Head, 2017b; Figure
1020 S23) and impact-induced shock waves tend to decay much faster; both factors lead to a
1021 significant reduction of cratering efficiency. Under these circumstances, typical cratering
1022 processes are largely obstructed, and the resultant craters are non-blocky, poorly preserved and
1023 easily degraded (Wilson & Head, 2017b; Figure S22c). Excavated materials are ejected at much
1024 lower velocities and higher ejection angles, so that a minimum amount of materials would be
1025 ejected beyond the crater interior. As solid foam is very weakly resistant to projectile
1026 penetration, craters tend to be much smaller in diameter and deeper than a similar impact into
1027 solid basalt or typical regolith (Figure S23a, b), as evidenced by numerous laboratory and
1028 numerical simulation impact experiments (e.g., Figure S23; Collins et al., 2011; Hörz et al.,

1029 2000; Housen & Holsapple 2003, 2011; Michikami et al., 2007; Schultz et al. 2002; Flynn et al.,
1030 2015; Wünnemann et al. 2006, 2011, 2012) and spacecraft observations at highly porous
1031 asteroids (e.g., Housen et al., 1999). Such high aspect ratios will decrease rapidly due to filling
1032 with crushed materials, producing shallower depressions.

1033 4.2.2 Space weathering

1034 When surface materials on an atmosphereless body, like the Moon, are exposed to the harsh
1035 space environment including interplanetary dust and micrometeorite bombardment, solar and
1036 cosmic ray irradiation, and solar wind implantation and sputtering, their physical and/or
1037 chemically properties are gradually modified; these complicated modifications are summarized
1038 as space weathering. From an optical perspective, typical lunar-style space weathering is
1039 characterized by the gradual darkening of surfaces (especially at visible and near-infrared
1040 wavelength), subduing of diagnostic absorption bands of minerals (especially iron-bearing
1041 components), and reddening of spectral slopes (relatively elevated reflectance at longer
1042 wavelengths); these systematic optical alterations are collectively termed as optical maturation
1043 (Hapke, 2001; Pieters & Noble, 2016). The optical property difference between the newly-
1044 exposed basaltic outcrops at small recently-formed fresh craters (e.g., the NW and SW craters
1045 near Ina, Figure 19) and ancient mare deposits (e.g., those of the Ina shield volcano flank, Figure
1046 19) is a visual demonstration of the space weathering effects (Figure 20). If the Ina interior is
1047 indeed emplaced contemporaneously with the adjacent ancient mare more than 3 Ga ago (section
1048 4.1), could the unusual physical properties of the Ina floor and mounds also account for their
1049 observed obvious optical immaturity (Figure 19)? The extremely micro-vesicular Ina mounds
1050 and the popped surface magmatic foam layer are predicted to be very capable of absorbing
1051 impact-induced shock waves (Figure S22c; e.g., Housen & Holsapple, 2003). In this scenario,
1052 micrometeorite impact vaporization tends to be less efficient, and then the production of reduced
1053 submicroscopic metallic iron particles, the major optical maturation agent, is retarded; similarly
1054 inefficient weathering processes are also observed at several asteroidal bodies with an inferred
1055 porous interior (e.g., Clark et al., 2002). In consequence, space weathering at the Ina mounds
1056 proceeds at a diminished rate, consistent with the observed relatively optical immaturity
1057 compared with the surrounding ancient shield volcano (Table S3). On the Ina lava lake crust, the
1058 continual infiltration and seismic sieving of the fine components of the developing surface
1059 weathered materials into the abundant void space below would continually expose underlying
1060 primitive, unweathered materials (Wilson & Head, 2017b; Figure S22b), thus maintaining the
1061 observed apparent optical immaturity of the floor substrate (Figure 19 and Table S3).

1062 4.2.3 Regolith development and evolution

1063 Lunar regolith development on ancient mare lava flow deposits (McKay et al., 1991) is
1064 commonly visualized as a dominantly mechanical weathering process of fragmentation and
1065 comminution of the emplaced basaltic bedrock by subsequent impactor populations and a steady
1066 stream of charged atomic particles, building up a fragmental and unconsolidated regolith layer of
1067 broken, melted and otherwise altered debris that increases in thickness as a function of time. The
1068 formation of each successive impact crater brecciates the underlying solid basalt substrate,
1069 excavates regolith and rock materials and spreads them laterally as ejecta, mixing with the
1070 growing regolith layer (Figure S22a). Surface regolith accumulated on ~3.5-Ga-old mare basalt
1071 flows is generally ~4–5 meters in thickness (McKay et al., 1991; Bart et al., 2011). The on-going
1072 accumulation of surface regolith would cause the destruction and burial of surface blocky

1073 materials, leading to the very rare occurrence of boulders on a typical mature lunar surface (e.g.,
1074 Basilevsky et al., 2015; Bandfield et al., 2011).

1075 On the surrounding mare and on the flanks of the Ina shield volcano, regolith development
1076 proceeds normally so that the current regolith thickness is estimated as ~4.8 m (section 3.13). On
1077 the Ina mounds, due to the observed predominantly non-blocky impact craters and much less
1078 lateral ejecta, regolith development and maturation is highly subdued (Figure S22c), consistent
1079 with our estimated median regolith thickness of 2.1 m from blocky crater measurements (section
1080 3.13 and Figure 18) and the interpreted 10–15 cm lower limit of regolith thickness from LRO
1081 Diviner radiometer data (Elder et al., 2016; 2017). In addition, the convex-upward shape of the
1082 mounds would cause regolith to preferentially move down towards the steeper mound flanks and
1083 then partly infiltrate into the marginal moats and underlying void space within the floor lava lake
1084 crust, becoming thinner at the margins, consistent with estimated regolith thickness at one of the
1085 largest Ina mounds (section 3.13 and Figure 18). On the regionally flat (but locally hummocky)
1086 deflated lava pond surface, regolith development is highly modified by the presence of
1087 significant volumes of shallow void space. As superposed impacts break up the meters-thick,
1088 draped, very vesicular lava lake crust surface and cause seismic shaking effects, finer materials
1089 preferentially sift and drain into the subsurface voids (Figure S22b). The ever-ongoing
1090 infiltration process would largely retard and inhibit the physical development and accumulation
1091 of the surface regolith soils, preferentially exposing the blockier substrate, consistent with the
1092 observed very thin, or near-absent regolith layer on the floor terrain (section 3.13), and block
1093 distributions (section 3.9).

1094 The continuous preferential drainage of regolith into void spaces implies that eventually the
1095 void space will be filled, and the currently observed difference between the adjacent shield
1096 flanks and the hummocky/rocky floor in roughness and optical maturity will disappear. The
1097 current state of the hummocky/rocky floor thus provides clues as to the amount of original void
1098 space required to explain the difference in block distribution and maturity between the mounds
1099 and the floor. The estimated regolith thickness discrepancy between the Ina floor and
1100 surrounding mare indicates that, if the seismic sieving model is correct, a net total of 3–4 m of
1101 void space below the chilled lava lake crust is required to accommodate the difference in
1102 thickness. Assuming that the topographic difference between the wall ledge and the deepest part
1103 of the floor (~30 m) represents the minimum depth of the drained lava lake, then $(3-4/30) \sim 10-$
1104 13% of this thickness/depth must have been retained as void space to account for the Ina
1105 observations. Applying simple beam theory to typical widths of floor units between mounds
1106 (~50–200 m) shows that a 1.5 m thick chilled lava crust could support a roof over a lava drainage
1107 channel up to ~30 m deep and ~150 m wide. If 20–25% of the floor unit was initially underlain
1108 by such drained lava channels, this volume of void space, with the addition of the abundant large
1109 macrovesicles and open void spaces formed during the complex lava lake process, would be
1110 more than sufficient to account for the “missing regolith”. Furthermore, any smaller drainage
1111 channels, and pressure ridges, as well as open void space in vesicular lavas and foams (observed
1112 to be in the 10-40% range in the upper 10 m at Kīlauea Iki, Richter & Moore, 1966), would
1113 further contribute to available void space for particle drainage during regolith formation and
1114 seismic sieving.

1115 Block distributions observed in the Ina interior also provide important insights into lava
1116 lake subsidence and substructure. Optical maturity data show that the least optically mature
1117 regions are collocated with the blockiest areas (Figure 19), and the blockiest areas in Ina

1118 correspond to the areas of steepest slopes (Figures 5b and 6c), consisting of the (1) scarps at the
1119 edge of the Ina interior, (2) boulder fields making up about 6% of the interior floor unit, and (3)
1120 moats frequently surrounding the mounds. The scarps, steep slopes and blocks at the base of the
1121 Ina interior wall are readily explained by the lava lake margins chilling against the pit crater wall
1122 and then the chilled edge being exposed by the downward and inward movement of the lava lake
1123 crust during drainage. The preferred occurrence of blocks within the moats is consistent with the
1124 enhanced regolith drainage due to the steep slopes of the mound margins (Figure 6c) and excess
1125 void space (cracks) formed by magmatic foam extrusion. The hummocky and pitted floor units
1126 within Ina's interior (section 3.5 and Figure 13) are interpreted to represent different degrees of
1127 drainage during regolith development: the hummocky terrain represents relatively thicker
1128 regolith, where drainage is slowing, net accumulation of soil is occurring, and superposed craters
1129 are starting to be retained. The pitted terrain is interpreted to be thinner regolith, with efficient
1130 drainage producing the pitted texture, and crater retention being relatively less efficient. The
1131 boulder fields are interpreted to represent the regions with the most efficient and long-lasting
1132 regolith drainage, and thus to be underlain by areas of most significant void space. The
1133 distribution of boulder fields in the floor unit, consisting of multiple annuli preferentially around
1134 the center of Ina, and the central parts of the inter-mound floor unit (Figure 5b), supports this
1135 interpretation. In terrestrial pit crater lava lakes (e.g., the Alea lava lake during the August 1963
1136 eruption; Peck & Kinoshita, 1976), cooling is more efficient in the shallower marginal parts of
1137 the lake, and less efficient over the deeper part above the source vent; upon multi-stage,
1138 intermittent drainage toward the central part of the lake above the vent, a network of sub-chilled
1139 crust lava tubes are very likely to be developed preferentially in a circumferential pattern on the
1140 crust. Maximum void space in these annuli would then lead to preferential drainage and
1141 maximum block exposure, as we observe (Figure 5b). Taken together, lateral variations in the
1142 distribution of void space could readily account for the observed complicated and variable
1143 surface textures on the Ina floor unit.

1144 4.2.4 Landscape evolution

1145 Landscape evolution is the post-emplacement, sequential modification of the initial
1146 landscape over geologic time driven by a wide range of exogenic and endogenic processes. As
1147 landforms are bounded by slopes, their evolution is best understood through the study of slope
1148 character and development, and the related controlling factors. On the Moon, during at least
1149 post-mare periods, impact cratering is the dominant process responsible for altering the surface
1150 topography. Conventional lunar crater production functions (e.g., the one proposed by Neukum
1151 et al., 2001) suggest a steep cumulative SFD for craters smaller than a few kilometers. Under this
1152 impact crater flux, the very frequent formation of small craters will smooth the topography at
1153 longer length baselines in a “sand-blasting” fashion and topographically mute them over time
1154 (Soderblom, 1970). This progressive degradation through impact cratering can be treated as a
1155 continuum problem, and the net effect is diffusional (Fassett & Thompson, 2014). This typical
1156 diffusive landscape evolution model applies to standard regolith development on mare basalt
1157 materials. Together, these cumulative events operate to create a thick regolith and to cause
1158 diffusive degradation of crisp and sharp landforms and boundaries typical of initially-formed
1159 pristine lava flows (Wilson & Head, 2017b; Figure S22a), as observed at ancient mare regions
1160 surrounding Ina (Figure 3).

1161 On the basis of the very high likelihood that the initial Ina mounds and lower unit floor
1162 topography date from the last stages of shield volcano pit crater resurfacing more than 3 Ga ago,

1163 we infer that these late stage pit crater evolution processes and the unique products can also
1164 account for the crisp appearance of the Ina interior geomorphology. In the case of Ina, floor units
1165 with extreme macro-porosity, where seismic sifting and vertical regolith infiltration are the
1166 dominant factors, will not be characterized by the typical type of topographic diffusive process
1167 (Figure S22b); neither will the hypothesized magmatic foam mounds, where superposed craters
1168 tend not to spread ejecta laterally away from the mounds, and any ejecta that might be spread
1169 laterally tends to be lost to regolith infiltration (Figure S22c). Together, these unusual surface
1170 modification processes will change landscape evolution from typical diffusive-process-
1171 dominated (Fassett & Thompson, 2014) to one of predominantly vertical regolith infiltration,
1172 serving to maintain the visual crispness and steep slopes of the terrain, and its sharp boundaries
1173 with the mounds and the more typical surroundings, cause the observed boulder exposure, and
1174 perpetuation of the surface roughness and optical immaturity. Fassett and Thompson (2015)
1175 report maximum ages for Ina scarps and moats, based on their diffusional model, of 5–40 Ma,
1176 supporting our model of the ongoing seismic sifting and regolith infiltration. The presence of
1177 abundant 1–5 m blocks (Figures 5b,c) and the localized steep slopes (Figures 6c and S19) at the
1178 bases of moats both indicate that local regolith infiltration is most efficient there and downward
1179 moat development and boulder exposure are ongoing processes, consistent with the extremely
1180 young diffusional model age (<1–2 Ma; Fassett & Thompson, 2015).

1181 4.3 Crater populations and retention ages

1182 Focusing on the Ina hummocky/blocky floor materials, Schultz et al. (2006) interpreted
1183 their rough texture and optical immaturity to be due to removal of fine materials by outgassing of
1184 juvenile volatiles occurring within the past 10 Ma, while Braden et al. (2014) interpreted the Ina
1185 mounds to be formed by extrusive volcanism that occurred about 33 Ma ago on the basis of their
1186 superposed impact crater size-frequency distribution. Our new crater population study also yields
1187 <100 Ma model ages for the Ina mounds and floor terrains (section 3.11). If the Ina shield
1188 volcano indeed formed ~3.5 Ga ago (Figure S1b), and the observed morphological crispness of
1189 Ina interior is consistent with the waning-stage evolution of lava lake processes within the
1190 summit pit crater, could the small area or the unusual physical properties of the mounds and floor
1191 also account for these observed anomalously young crater retention ages? Our previous work has
1192 provided a preliminary analysis of impact into the magmatic foam mounds and the resultant
1193 crater retention age (Qiao et al., 2017). We here present an updated and more detailed
1194 investigation of impact cratering in Ina mounds and a new analysis of impact cratering in Ina
1195 floor hummocky units.

1196 To begin with, we focused on the Ina mounds, which are dated younger than 100 Ma via
1197 superposed impact crater populations (Braden et al., 2014 and section 3.11). In order to
1198 investigate the crater SFD and its discrepancy from the 3.5 Ga-old hosting shield volcano, we
1199 first re-counted all impact craters larger than 10 m in diameter superposed on the Ina mounds
1200 using LROC NAC images with a wide range of illumination geometries and found more than
1201 twice as many craters as reported by Braden et al. (2014), yielding a model age of 59 Ma (Figure
1202 16c and Table 1); this indicates that craters formed on the Ina mounds are poorly preserved and
1203 easily degraded beyond recognition, consistent with our proposed cratering mechanism on the
1204 solid magmatic foams (section 4.2.1). Secondly, we investigated the distribution of superposed
1205 craters as a function of topographic slope on the mounds and found that there are many fewer
1206 small craters where slopes exceed 6 degrees than on the flatter part of the mounds, leading us to
1207 conclude that the convex shape of the mounds could lead to the loss of superposed craters as a

1208 function of time. Thirdly, we asked the question: Could the small total area and irregular shapes
 1209 of the mounds contribute to an artificially younger crater retention age? We transferred a map of
 1210 Ina interior to the upper flank of the shield volcano where we obtained the ~3.5 Ga age for the
 1211 shield (Figure 16b), and found it has a relatively lower cumulative crater density at larger sizes
 1212 than the much more extensive crater counting area on the shield (ca. Figure S1b and Figure 16c).
 1213 This exercise suggests that the counting area may be too small and that if a larger counting area
 1214 is used, a greater number of larger craters would be detected, potentially resulting in an older
 1215 model age, as suggested by previous works (e.g., van der Bogert et al. 2015).

1216 Fourthly, we addressed the question of whether the solid magmatic foam substrate could be
 1217 responsible for altering the superposed impact crater SFD compared with what would be
 1218 expected in normal basalt lava flows (as observed on the Ina shield volcano flanks; ~3.5 Ga).
 1219 Target porosity, along with other substrate properties, has long been revealed to have significant
 1220 effects on the impact process and final crater dimensions, particularly for smaller craters formed
 1221 in the strength-dominated regime. On the Moon, the strength-controlled scaling applies to craters
 1222 with diameters smaller than ~300–400 m (Schultz & Spencer, 1979; Melosh, 1989), so almost all
 1223 craters superposed on both Ina mounds (Figure 16a) and the surrounding shield flank count area
 1224 (Figures 16 and S1) are formed in the strength-scaling regime. The extreme micro-vesicular
 1225 nature of the Ina mounds will introduce a distinct impact cratering mechanism characterized by
 1226 more energy dissipation, permanent crushing and compaction of the target material, smaller
 1227 crater diameters, and a minimum amount of ejected materials (section 4.2.1 and references
 1228 therein; Figure S22c). Wünnemann et al. (2011) employed a porosity compaction model and
 1229 conducted a suite of hundreds of numerical modeling experiments of impacts into targets of
 1230 variable porosity (up to 35%) and found a negative linear relationship between target porosity
 1231 and one of the crater scaling parameters when keeping other conditions constant; for instance, for
 1232 a constant substrate friction coefficient of 0.8, dimensionless crater diameters formed within a
 1233 25%-porosity target are reduced by ~20% compared with those within a consolidated (zero
 1234 porosity) target. Prieur et al. (2017) ran numerous numerical calculations and parameterized the
 1235 effect of porosity on crater scaling coefficients, which suggests a change in porosity from 10% to
 1236 50% would result in a decrease of ~20–25% in crater diameter. Laboratory impact cratering
 1237 experiments into various targets of a wider porosity (φ) range, including basaltic rocks ($\varphi \approx 0$),
 1238 dry sandstone ($\varphi = \sim 23\%$) and sintered glass beads ($\varphi = \sim 5\%–84\%$), demonstrate that porosity,
 1239 when observed as an isolated parameter, exponentially reduces crater volumes (V_N) (Moore et al.,
 1240 1963; Michikami et al., 2007; Poelchau et al., 2013). Mathematical fitting to all these
 1241 experimental data parameterizes crater volume as a function of target porosity: $V_N = (1.10 \pm$
 1242 $0.10) e^{(-0.077 \pm 0.004)\varphi}$, where φ is given as a percentage. Given the hypothesized magmatic foam
 1243 nature of Ina mounds and the popping of the surface layer during its extrusion process, a bulk
 1244 porosity of ~75% can be conservatively assumed (Qiao et al., 2017). The porosity of the
 1245 uppermost meters of typical mare regions (in which most regolith-building craters formed) is
 1246 incompletely understood, though it can reasonably be assumed to be between ~12%
 1247 (gravitational calculations for the lunar crust, Wieczorek et al. 2013) and ~30% (measurements
 1248 of returned core samples, Carrier et al., 1991). Substituting these substrate porosity values into
 1249 the empirical function implies that the volume of craters formed in the Ina mounds will be
 1250 reduced by a factor of between ~30 to ~125 compared with those in the typical lunar mare
 1251 regolith targets, which corresponds to a factor of ~3–5 decrease in crater diameter (specifically, a
 1252 reduction to 19.8%–31.5% of the original diameter value). This laboratory experiment-based
 1253 estimation of the crater diameter diminishing effect is generally consistent with pi-group scaling

1254 calculations, which show that impacts into more porous targets tend to produce smaller craters
1255 than into less porous targets, and target property contrasts between porous mare rock and non-
1256 porous rock can lead to an up to ~250% difference in final crater diameters (van der Bogert et al.
1257 2017). Target property variations have also been observed to result in an impact crater density
1258 difference of up to ~600–700% between comparably-aged surface terrains on Mars (Dundas et
1259 al., 2010), more than sufficient to explain the crater density disparity between the Ina interior
1260 mounds and exterior shield flanks (section 3.11).

1261 Finally, this considerable crater scaling effect of the highly porous nature of Ina mounds
1262 provides an important insight in interpreting its anomalously young crater retention ages and
1263 their discrepancy from the surrounding shield flanks. We re-sized all the superposed impact
1264 craters identified in the count area on the Ina shield volcano (Figure S1a) with diameter
1265 reductions by factors of 3 and 5 as found above. The cumulative SFDs of the two diameter-
1266 scaled crater populations then plot very close to that of the Ina mounds, and, of particular
1267 interest, the SFD plot of the Ina mound craters lies between that of the two scaled crater
1268 populations (Figure 22). Fitting of the scaled craters using Neukum functions (Neukum et al.,
1269 2001) yields model ages of 24 Ma and 93 Ma, respectively; both are younger than ~100 Ma.
1270 Most importantly, the crater retention age of Ina mounds either previously obtained by Braden et
1271 al. (33 Ma; 2014) or updated by our renewed crater counts (59 Ma; section 3.11) lies between the
1272 ages derived from the two scaled shield crater populations.

1273 We now turn our focus to the impact populations on the Ina hummocky floor terrain.
1274 Characterized by an unusual substrate nature of multiple large void spaces (macro-vesicularity)
1275 and abundant micro-vesicularity, impacts into the Ina floor terrain are predicted to be dominated
1276 by continued vertical infiltration and seismic sieving of the surface regolith and impact breccia,
1277 resulting in craters being poorly developed, difficult to identify, and degrading very rapidly
1278 (section 4.2.1 and Figure S22b). Large impacts will tend to not form ejecta, but instead crush the
1279 targets and leave very shallow craters filled with crushed rubble; these are not very obvious to
1280 start with and degrade rapidly, producing a deficit of larger craters. This unusual impact cratering
1281 behavior (decrease in diameter) and rapid loss of superposed craters will inhibit intensely the
1282 construction of a crater record typical of normal lunar terrains elsewhere and its preservation on
1283 the lunar surface, and push the impact crater SFD to extreme younger ages. The observed
1284 elevated optically immaturity of the floor terrains suggests that this crater “loss” process
1285 probably operates more intensely on the floor units than on the Ina mounds, consistent with the
1286 estimated comparable or younger crater retentions ages of the Ina floor units (Figure 16c).

1287 Based on the suite of analyses above, we conclude that the unusually low impact crater
1288 density on the Ina mounds and floor terrains and the resultant anomalously young crater retention
1289 ages can be well understood in terms of the role of the unique substrate characteristics (chilled
1290 lava lake crust floor and solid magmatic foam extrusions) in the formation and retention of
1291 superposed impact craters, along with other factors including the relatively smaller crater count
1292 area, and the rapid loss of craters due to the slope effect and continuous regolith infiltration
1293 process. Nevertheless, we should note that the detailed impact cratering mechanism in highly
1294 porous targets (e.g., Ina foamy mounds) and the resultant effects on crater retention age are
1295 currently not completely understood. Additional future laboratory and numerical investigations
1296 would further contribute to our understanding of these processes.

1297 4.4 Implications for the origin of other IMPs and duration of mare volcanism

1298 Our comprehensive geological characterization and observation-based analysis
 1299 convincingly supports the two-component scenario of waning-stage lava lake processes and
 1300 magmatic foam extrusion for the formation of the Ina interior (Qiao et al., 2017; Wilson & Head,
 1301 2017b). These processes produce volcanic deposits with very unusual physical properties, thus
 1302 exerting an influence on the nature of regolith development, and crater formation and retention
 1303 processes, resulting in anomalously young interpreted ages for the Ina summit pit crater floor
 1304 that more plausibly formed contemporaneously with the underlying shield volcano about 3.5 Ga
 1305 ago. The two other lunar IMP occurrences dated as younger than 100 Ma by Braden et al. (2014)
 1306 (i.e., Sosigenes, ~18 Ma, and Cauchy 5, ~58 Ma; Figure S24) also lie at the top of dikes (Qiao et
 1307 al., 2018a; Qiao et al., 2018b), and hence could be re-interpreted to be emplaced in a similar
 1308 manner billions of years ago. Our interpreted ancient formation ages, in contrast to the
 1309 geologically very recent lava extrusion hypothesis (Braden et al., 2014), also coincide with the
 1310 climax of global volcanism between ca. 3.3–3.8 Ga ago (e.g., Pasckert et al., 2018 and therein).
 1311 The current lunar thermal regime and magmatic evolution models suggest that the Moon, as a
 1312 one-plate planetary body, progressively lost its primordial and internally generated heat
 1313 effectively by conduction, leading to volcanism having waned in middle lunar history and ceased
 1314 sometime in the last ~1 Ga (e.g., Solomon & Head, 1980; Head & Wilson, 1992, 2017; Hiesinger
 1315 et al. 2011; Morota et al. 2011). Our new model of contemporaneous late-stage shield building
 1316 volcanism ~3.5 Ga ago thus makes a major re-evaluation of the conventional theory unnecessary.
 1317 Our progressive observational and numerical investigations of Ina (Qiao et al., 2016, 2017,
 1318 2018a, 2018b; Wilson & Head, 2017b, 2018) make it a prime target candidate for future landers,
 1319 rovers and sample return missions, which show enormous potential for strengthening our
 1320 knowledge of the magmatism and thermal evolution of the Moon and other terrestrial bodies
 1321 (e.g., Draper et al., 2018; Qiao et al., 2018c; Wagner et al., 2018).

1322 5. Conclusions

1323 On the basis of the comprehensive geological characterization and analysis of the origin of
 1324 the Ina pit crater presented above, we draw the following conclusions:

- 1325 (1) *Location, Context and Age*: Ina is located in the middle of Lacus Felicitatis, a small
 1326 Imbrian-aged mare occurrence on the lunar nearside. The Lacus Felicitatis basalts are
 1327 superposed on the areally extensive ejecta deposits from the Imbrim and Serenitatis
 1328 basins emplaced ca. 3.85 Ga ago, and on the extensive and topographically prominent
 1329 linear ejecta scour radial to the two basins. The mare basalts emplaced within central
 1330 Lacus Felicitatis (within which Ina is located) exhibit apparent compositional changes as
 1331 a function of time, with underlying (relatively old) basalts more titanium-rich than the
 1332 surface (most recently emplaced) basalts. The central part of Lacus Felicitatis lies on a
 1333 plateau up to ~800 m above the adjacent maria on topography most likely related to the
 1334 radial Imbrium ejecta sculpture.
- 1335 (2) *Superposition of Ina on an Ancient Shield Volcano*: Locally, Ina occurs as a ~2×3 km
 1336 summit pit crater atop a broad dome ~22 km wide at its base, ~320 m high and ~0.6 km³
 1337 in volume, which is interpreted as a small shield volcano built up through accumulating
 1338 low-effusion rate, cooling-limited flows during eruptions from a single dike source ~3.5
 1339 Ga ago. The Ina shield volcano is at the upper end of the height and diameter range of
 1340 over 300 small mare shields identified on the Moon, consistent with its formation by
 1341 relatively longer flows (up to ~12 km) through lengthy eruptions (estimated at ~3–6

1342 months). Theories of the origin of the Ina structure and its unusual features must account
 1343 for the fact that Ina is the summit pit crater on an ancient ~3.5 Ga shield volcano built on
 1344 associated mare deposits.

1345 (3) *Similarity of Ina Summit Pit Crater to those on Hawai'i*: The Ina summit pit crater
 1346 interior is defined by an inward-facing wall and a relatively flat basal terrace/ledge with a
 1347 steep inward-facing scarp up to ~12 m high, and the pit crater is externally bordered by a
 1348 low raised “collar” structure. On the basis of our documentation and the similarities to
 1349 small Hawaiian volcano pit craters, we interpret Ina’s external narrow collar to be the
 1350 remnant of lava lake filling and overflow, together with deposited pyroclastic debris, and
 1351 the interior basal terrace and steep inward-facing scarp to be the chilled margin of a lava
 1352 lake remaining after lava lake cooling and/or recession, embayed by subsequent
 1353 magmatic foam extrusions near the floor edge.

1354 (4) *Major Ina Interior Units*: The Ina interior is made up of three major morphologic units
 1355 also typical of other major lunar IMPs: (a) topographically higher, bulbous-shaped
 1356 mound units (50% by area) surrounded by (b) topographically lower, hummocky units
 1357 (44%) with ridged and pitted textures, and (c) topographically lower, blocky units (6%)
 1358 consisting of 1–5 m size boulders.

1359 (5) *Theoretical Assessment of the Ascent and Eruption of Magma in Late Stage Summit Pit*
 1360 *Craters on the Moon*: On the basis of (a) our latest theoretical treatment of late-stage
 1361 shield-building magmatic activity and volatile exsolution physics, (b) documentation of
 1362 magmatic-volcanic processes from terrestrial small shield volcano summit pit craters in
 1363 Hawai'i, and (c) comprehensive geological characterization of the context and interior of
 1364 Ina pit crater, we interpret the wide range of characteristics associated with the Ina
 1365 feature to be consistent with a two-component model of origin during the waning stages
 1366 of shield volcano summit pit crater eruption activities characterized by the extrusion and
 1367 solidification of magmatic foams (“mound foam model”) on a subsided lava lake crust
 1368 (“hummocky floor model”), occurring ~3.5 Ga ago, contemporaneous with the
 1369 underlying shield volcano and the major global phase of lunar mare volcanism.

1370 (6) *Nature and Origin of the Ina Summit Pit Crater Interior Mounds*: Over 80 individual
 1371 mounds are arrayed across the interior of Ina and a few form coalescing patterns. The
 1372 tops of Ina mounds are typically ~20–50 m below the pit crater rim crest, and rise up to
 1373 ~20 m above the adjacent floor terrains. Topographic moats, several meters wide and up
 1374 to ~1 m deep, are often observed at the mound margins. The summit elevation of mounds
 1375 decreases toward the center of Ina and the majority of mounds show area-averaged
 1376 slopes towards the pit crater center. Several bleb-like mounds are observed to be located
 1377 in small topographic depressions in a manner similar to “ring-moat dome structures”
 1378 recently documented elsewhere in the lunar maria. The bleb-like mounds are interpreted
 1379 to be magmatic foam extruded through cracks in the solidified lava lake crust. Extrusion
 1380 of the foam causes subsidence and flexure of the lava lake crust in the immediate vicinity
 1381 of the foam, enhancing the meniscus-like borders of the mounds, the scarp-like contacts
 1382 with the floor terrains, and the creation of moats at the margins. The popping of the
 1383 outermost layer of extruded foam gas bubbles will produce a surface layer with smaller
 1384 particle sizes than typical mature regolith. Rheological modeling shows that magmatic
 1385 foam extrusion is likely to proceed at a very low effusion rate ($<1 \text{ m}^3/\text{s}$), and that the

1386 majority of the Ina mounds are predicted to be emplaced over a period of several hours to
 1387 several days (Wilson & Head, 2017b).

1388 (7) *Nature and Origin of the Ina Summit Pit Crater Floor Unit:* The Ina summit pit crater
 1389 interior floor, including both hummocky and blocky units, mainly lies about 20–50 m
 1390 below the pit crater rim, and is generally flat, while sloping gently ($<2^\circ$) toward the
 1391 center (Figure 7). The pit crater floor can be categorized as three annular terraces, with
 1392 ~10 m elevation decrements toward the interior. The interior mounds appear to
 1393 preferentially present at the contacts between the annular terraces, suggesting an
 1394 association between lava lake subsidence, lava lake crust flexure and cracking, and the
 1395 extrusion of the foam mounds. The floor hummocky/blocky units are characterized by a
 1396 wide range of very complex morphologies. We interpret the floor terrains as solidified
 1397 lava lake crust, and each of their complex topographic and morphologic characteristics
 1398 corresponds to the various processes operating during the lava lake formation, evolution
 1399 and solidification process: 1) the three-stage annular, inwardly lower floor topography is
 1400 interpreted to be formed through lava lake inflation, drainage and ultimate solidification;
 1401 2) the hummocky textures could be analogous to lava lake inflation, lava lake crust
 1402 flexure, bending, fracturing and ridge formation, with hornitos and other features partly
 1403 buried by subsequent flows; 3) the abundant pits are interpreted to be due to regolith
 1404 infiltration and sifting into the porous and macro-vesicular lava lake crust and void space
 1405 below; 4) the linear depressions/fractures are interpreted to be modified cracks in the
 1406 lava lake surface formed by flexure, cooling and shrinkage during lava lake deflation and
 1407 deformation; 5) the polygonal patterns are analogous to highly deformed and cracked
 1408 lava lake crust; 6) the vermicular patterns are analogous to tilted lava lake crust plates; 7)
 1409 the ridged textures are interpreted to be locally deformed lava surface crust; 8) the floor
 1410 blocky units are analogous to blocks of the solidified lava lake crust exposed by impact
 1411 and drainage of regolith fines into the subsurface; 9) the preferential occurrences of
 1412 mounds at the contacts between floor annular terraces is interpreted to be due to the
 1413 extrusion of magmatic foam through the lava lake crust fractures caused by its inward
 1414 subsidence.

1415 (8) *Effects of Unusual Summit Pit Crater Floor Features on Their Subsequent Evolution:*
 1416 The unusual physical characteristics of the Ina interior, solidified magmatic foam
 1417 mounds with bulk porosity up to ~95% and chilled lava lake crust floor with abundant
 1418 micro-vesicularity and large void spaces, introduce remarkable differences in the
 1419 processes that characterize post-emplacment geological modification of lunar features,
 1420 including impact cratering, optical maturation, regolith development and topographic
 1421 degradation.

1422 (9) *Characteristics of Impact Cratering in the Lunar Summit Pit Crater Floor Environment:*
 1423 On the Ina floor terrains, due to the highly vesicular nature of the substrate, impact
 1424 cratering will be dominated by permanent crushing and compaction of the target
 1425 materials, disruption of vesicle walls, excavation of the blocky portions of the crust
 1426 substrate, and a negligible amount of lateral ejecta transfer beyond the crater rim. The
 1427 resultant craters are predicted to be poorly developed (much deeper penetration relative
 1428 to lateral crater growth), filled with crushed rubble, abnormally-shaped, difficult to
 1429 identify and to degrade rapidly, and to show a deficit of larger craters due to the
 1430 decreased diameter-depth relationship. The continuous infiltration of the finer

1431 components of surface regolith into the significantly macro-porous substrate, assisted by
1432 subsequent impact-induced seismic shaking and sieving, is predicted to change the
1433 typical laterally diffusive topographic degradation into a vertical infiltration-dominated
1434 style, serving to largely inhibit the physical development and accumulation of regolith,
1435 maintain the morphological crispness and optical immaturity, and expose underlying
1436 fresh and unweathered blocks and boulders.

1437 (10) *Impact Cratering on the Summit Pit Crater Floor Foam Mounds*: On the Ina floor
1438 mounds, interpreted to be formed by extrusion of magmatic foam, subsequent impact
1439 cratering will operate in a style dominated by permanent compressing, crushing,
1440 shattering and penetrating of the foam vesicles (the aerogel effect), and rapid decay of
1441 impact-induced shock waves, leading to a significant reduction of cratering efficiency.
1442 Under these circumstances, the mound craters tend to be much smaller in diameter and
1443 deeper, non-blocky, poorly preserved and easily degraded, than those formed by a
1444 similar impact into typical solid basalt or regolith. The effective absorption of impact-
1445 induced shock waves decreases the production of reduced submicroscopic metallic iron
1446 particles, retarding the typical optical maturing of the mound materials. Regolith
1447 development on Ina mounds is inhibited due to the predominantly non-blocky impact
1448 craters, much lower amount of lateral ejecta, and the preferential downslope movement
1449 of surface regolith toward the steeper mound margins. Landscape evolution on the
1450 mounds will also operate in a vertical compressing and crushing style, rather than a
1451 lateral ejecta dispersal dominated style, thus helping to maintain sharp mound boundaries
1452 with the floor terrains.

1453 (11) *Effect of the High-porosity Substrate Characteristics on the Retention Ages of*
1454 *Superposed Impact Craters*: The impact craters superposed on both mounds and floor
1455 terrains of the Ina summit pit crater interior exhibit a range of morphological peculiarities,
1456 significantly different from their counterparts on typical mare regolith regions. The Ina
1457 floor has an areal density of superposed impact craters comparable to, or slightly lower
1458 than, the Ina mounds, and both Ina interior units yield crater retention ages less than 100
1459 Ma, significantly younger than the ~3.5 Ga old age estimated for the adjacent and
1460 underlying shield volcano flanks. The apparent discrepancy in impact crater populations
1461 and the resultant crater retention ages can be understood in the context of the role of the
1462 unique substrate characteristics (chilled lava lake crust floor and solidified magmatic
1463 foam extrusions) in the formation and retention of superposed impact craters. Accounting
1464 for the effects of the reduced size of craters (smaller by factors of ~3–5) formed in the
1465 highly porous magmatic foam mounds results in a shift of the crater SFD model ages
1466 from <100 Ma to ~3.5 Ga, contemporaneous with the age of the underlying ancient
1467 shield volcano and the major global phase of lunar mare volcanism. We conclude that
1468 extremely young mare basalt eruptions to account for the Ina summit pit crater floor
1469 formation is not required, and that the presented scenario is in accord with lunar thermal
1470 evolution models.

1471 (12) *Implications for Future Exploration*: Future robotic and human exploration of Ina and
1472 related IMP deposits could resolve many of the outstanding questions remaining about
1473 these enigmatic features. Sample return missions could provide radiometric dates for the
1474 Ina deposits, readily distinguishing between a 3.5 Ga and a <0.1 Ga crystallization age,
1475 as well as determining the physical properties of the mounds and hummocky materials.

1476 Seismometers and other geophysical instruments could test hypotheses for the density
 1477 structure of the lava lake floor and underlying solidified lava lake. Penetrometer missions
 1478 could also assist in the analysis of physical properties of the substrate materials. Such
 1479 future missions could help resolve the several hypotheses for the enigmatic Ina feature
 1480 and contribute critical information on the total duration of mare basalt volcanism and the
 1481 thermal evolution of the Moon.

1482 **Acknowledgments**

1483 This study is a multilateral effort involving scientists from the United States, the United
 1484 Kingdom and China. This study is supported by the Key Research Program of the Chinese
 1485 Academy of Sciences (Grant No. XDPB11), the National Natural Science Foundation of China
 1486 (Nos. 41703063 and 41373066), the China Postdoctoral Science Foundation (Nos.
 1487 2017M610421 and 2018T110682) and Open Fund of State Key Laboratory of Information
 1488 Engineering in Surveying, Mapping and Remote Sensing, Wuhan University (Grant No. 18P03).
 1489 L. Q. was partially supported by the State Scholarship Fund from Chinese Scholarship Council
 1490 as a visiting student at Brown University (No. 201406410040). L. W. thanks the Leverhulme
 1491 Trust for support via an Emeritus Fellowship. We gratefully acknowledge financial support from
 1492 the NASA Solar System Exploration Research Virtual Institute (SSERVI) grant for Evolution
 1493 and Environment of Exploration Destinations under cooperative agreement number
 1494 NNA14AB01A at Brown University. This work was partly funded as part of J. W. H.'s
 1495 membership on the Lunar Reconnaissance Orbiter Lunar Orbiter Laser Altimeter (LOLA) team,
 1496 under NASA grant NNX09AM54G to J. W. H. We gratefully acknowledge W. Brent Garry, an
 1497 anonymous reviewer and the Editor David Baratoux for their helpful comments. All original
 1498 LRO data can be found in the NASA's Planetary Data System (<http://pds.nasa.gov/>) and all
 1499 original Kaguya/SELENE data are archived at SELENE Data Archive
 1500 (<https://darts.isas.jaxa.jp/planet/pdap/selene/>).

1501 **References**

- 1502 Anderson, J. A., Sides, S. C., Soltesz, D. L., Sucharski, T. L., & Becker K. J. (2004).
 1503 Modernization of the integrated software for imagers and spectrometers. *35th Lunar and*
 1504 *Planetary Science Conference*, Lunar and Planetary Institute, League City, Texas, abstract
 1505 #2039.
- 1506 Barker, M. K., Mazarico, E., Neumann, G. A., Zuber, M. T., Haruyama, J., & Smith, D. E.
 1507 (2016). A new lunar digital elevation model from the Lunar Orbiter Laser Altimeter and
 1508 SELENE Terrain Camera. *Icarus*, 273, 346-355. <https://doi.org/10.1016/j.icarus.2015.07.039>
- 1509 Bart, G. D., Nickerson, R. D., Lawder, M. T., & Melosh, H. J. (2011). Global survey of lunar
 1510 regolith depths from LROC images. *Icarus*, 215, 485-490.
 1511 <https://doi.org/10.1016/j.icarus.2011.07.017>
- 1512 Bart, G. D. (2014). The quantitative relationship between small impact crater morphology and
 1513 regolith depth. *Icarus*, 235(0), 130-135. <https://doi.org/10.1016/j.icarus.2014.03.020>
- 1514 Bandfield, J. L., Ghent, R. R., Vasavada, A. R., Paige, D. A., Lawrence, S. J., & Robinson, M. S.
 1515 (2011). Lunar surface rock abundance and regolith fines temperatures derived from LRO
 1516 Diviner Radiometer data. *Journal of Geophysical Research: Planets*, 116(E12).
 1517 <https://doi.org/10.1029/2011JE003866>

- 1518 Basilevsky, A. T., Head, J. W., & Horz, F. (2013). Survival times of meter-sized boulders on the
 1519 surface of the Moon. *Planetary and Space Science*, 89, 118-126.
 1520 <https://doi:10.1016/j.pss.2013.07.011>
- 1521 Bennett, K. A., Horgan, B. H. N., Bell, J. F., III, Meyer, H. M., & Robinson, M. S. (2015). Moon
 1522 Mineralogy Mapper investigation of the Ina irregular mare patch. *46th Lunar and Planetary
 1523 Science Conference*, Lunar and Planetary Institute, The Woodlands, Texas, abstract #2646.
- 1524 Bowman-Cisneros, E. (2010). *LROC EDR/CDR Data Product Software Interface Specification*.
 1525 Retrieved from [http://lroc.sese.asu.edu/data/LRO-L-LROC-2-EDR-](http://lroc.sese.asu.edu/data/LRO-L-LROC-2-EDR-V1.0/LROLRC_0001/DOCUMENT/LROCSIS.PDF)
 1526 [V1.0/LROLRC_0001/DOCUMENT/LROCSIS.PDF](http://lroc.sese.asu.edu/data/LRO-L-LROC-2-EDR-V1.0/LROLRC_0001/DOCUMENT/LROCSIS.PDF)
- 1527 Braden, S. E., Stopar, J. D., Robinson, M. S., Lawrence, S. J., van der Bogert, C. H., &
 1528 Hiesinger, H. (2014). Evidence for basaltic volcanism on the Moon within the past 100 million
 1529 years. *Nature Geoscience*, 7(11), 787-791. <https://doi.org/10.1038/ngeo2252>
- 1530 Braden, S. E. (2013). Analysis of spacecraft data for the study of diverse lunar volcanism and
 1531 regolith maturation rates (Doctoral dissertation). Retrieved from ASU Library.
 1532 (<http://repository.asu.edu/items/20943>). Tempe, AZ: Arizona State University.
- 1533 Carrier, W. S., Olhoeft, G. R., & Mendell W. (1991). Physical properties of the lunar surface. In
 1534 G. H. Heiken, D. T. Vaniman, B. M. French, (Eds.), *Lunar Sourcebook* (pp. 475–594).
 1535 Cambridge: Cambridge University Press.
- 1536 Carter, L. M., Hawke, B. R., Garry, W. B., Campbell, B. A., Giguere, T. A., & Bussey, D. B. J.
 1537 (2013). Radar observations of lunar hollow terrain. *44th Lunar and Planetary Science
 1538 Conference*, Lunar and Planetary Institute, The Woodlands, Texas, abstract #2146.
- 1539 Clark, B. E., Hapke B., Pieters, C. & Britt, D. (2002). Asteroid space weathering and regolith
 1540 evolution. In W. F. Bottke, A. Cellino, P. Paolicchi, R. P. Binzel (Eds), *Asteroids III* (pp. 585–
 1541 599). Tuscon, AZ: University of Arizona Press.
- 1542 Collins, G. S., Melosh, H. J., & Wünnemann, K. (2011). Improvements to the ϵ - α porous
 1543 compaction model for simulating impacts into high-porosity solar system objects.
 1544 *International Journal of Impact Engineering*, 38(6), 434-439.
 1545 <https://doi.org/10.1016/j.ijimpeng.2010.10.013>
- 1546 Crater Analysis Techniques Working Group (1979). Standard techniques for presentation and
 1547 analysis of crater size-frequency data. *Icarus*, 37(2). 467-474. [https://doi.org/10.1016/0019-](https://doi.org/10.1016/0019-1035(79)90009-5)
 1548 [1035\(79\)90009-5](https://doi.org/10.1016/0019-1035(79)90009-5).
- 1549 Daubar, I. J., Atwood-Stone, C., Byrne, S., McEwen, A. S., & Russell, P. S. (2014). The
 1550 morphology of small fresh craters on Mars and the Moon. *Journal of Geophysical Research:*
 1551 *Planets*, 119(12), 2620-2639. <https://doi.org/10.1002/2014JE004671>.
- 1552 Draper, D. S., Stopar, J. D., Lawrence, S. J., Denevi, B., John, K., Graham, L., et al. (2018), The
 1553 Irregular Mare Patch Exploration Lander (IMPEL) SmallSat mission concept. *49th Lunar and
 1554 Planetary Science Conference*, Lunar and Planetary Institute, The Woodlands, Texas, abstract
 1555 #1617.
- 1556 Dundas, C. M., Keszthelyi, L. P., Bray, V. J., & McEwen, A. S. (2010). Role of material
 1557 properties in the cratering record of young platy-ridged lava on Mars. *Geophysical Research
 1558 Letters*, 37, L12203. <https://doi.org/10.1029/2010GL042869>
- 1559 Dzurisin, D., Koyanagi, R. Y., & English, T. T. (1984). Magma supply and storage at Kilauea
 1560 volcano, Hawaii, 1956–1983. *Journal of Volcanology and Geothermal Research*, 21(3), 177-
 1561 206. [https://doi.org/10.1016/0377-0273\(84\)90022-2](https://doi.org/10.1016/0377-0273(84)90022-2)
- 1562 El-Baz, F. (1972). New geological findings in Apollo 15 lunar orbital photography. *Proceedings
 1563 of 3rd Lunar and Planetary Science*, 39–61.

- 1564 El-Baz, F. (1973), D-caldera: New photographs of a unique feature. In *Apollo 17 Preliminary*
 1565 *Science Report* (NASA SP-330, pp. 30-13–30-17). Washington, DC: United States
 1566 Government Printing Office.
- 1567 Elder, C. M., Hayne, P. O., Ghent, R. R., Bandfield, J. L., Williams, J. P., & Paige, D. A. (2016).
 1568 Regolith formation on young lunar volcanic features, *47th Lunar and Planetary Science*
 1569 *Conference*, Lunar and Planetary Institute, The Woodlands, Texas, abstract #2785.
- 1570 Elder, C. M., Hayne, P. O., Bandfield, J. L., Ghent, R. R., Williams, J. P., Donaldson Hanna, K.
 1571 L., & Paige, D. A. (2017). Young lunar volcanic features: Thermophysical properties and
 1572 formation. *Icarus*, 290, 224-237. <https://doi.org/10.1016/j.icarus.2017.03.004>
- 1573 Fassett, C. I., & Thomson, B. J. (2014). Crater degradation on the lunar maria: Topographic
 1574 diffusion and the rate of erosion on the Moon. *Journal of Geophysical Research: Planets*,
 1575 119(10), 2255-2271. <https://doi.org/10.1002/2014je004698>
- 1576 Fassett, C. I., & Thomson, B. J. (2015). A landscape evolution perspective on how young is
 1577 young on the lunar surface. *46th Lunar and Planetary Science Conference*, Lunar and
 1578 Planetary Institute, The Woodlands, Texas, abstract #1120.
- 1579 Flynn, G. J., Durda, D. D., Patmore, E. B., Clayton, A. N., Jack, S. J., Lipman, M. D., & Strait,
 1580 M. M. (2015). Hypervelocity cratering and disruption of porous pumice targets: Implications
 1581 for crater production, catastrophic disruption, and momentum transfer on porous asteroids.
 1582 *Planetary and Space Science*, 107, 64-76. <https://doi.org/10.1016/j.pss.2014.10.007>
- 1583 Garry, W., Robinson, M., Zimbelman, J., Bleacher, J., Hawke, B., Crumpler, L., et al. (2012),
 1584 The origin of Ina: Evidence for inflated lava flows on the Moon, *Journal of Geophysical*
 1585 *Research: Planets*, 117, E00H31. <https://doi.org/10.1029/2011JE003981>
- 1586 Garry, W. B., Hawke, B. R., Crites, S., Giguere, T., & Lucey, P. G. (2013). Optical maturity
 1587 (OMAT) of Ina 'D-Caldera', the Moon. *44th Lunar and Planetary Science Conference*, Lunar
 1588 and Planetary Institute, The Woodlands, Texas, abstract #3058.
- 1589 Hapke, B. (2001), Space weathering from Mercury to the asteroid belt, *Journal of Geophysical*
 1590 *Research: Planets*, 106(E5), 10039-10073. <https://doi.org/10.1029/2000je001338>
- 1591 Hardee, H. C. (1980). Solidification in Kilauea Iki Lava Lake, *Journal of Volcanology and*
 1592 *Geothermal Research*, 7(3-4), 211-233. [https://doi.org/10.1016/0377-0273\(80\)90030-X](https://doi.org/10.1016/0377-0273(80)90030-X)
- 1593 Haruyama, J., Matsunaga, T., Ohtake, M., Morota, T., Honda, C., Yokota, Y., et al. (2008).
 1594 Global lunar-surface mapping experiment using the Lunar Imager/Spectrometer on SELENE.
 1595 *Earth, Planets and Space*, 60(4), 243-255. <https://doi.org/10.1186/BF03352788>
- 1596 Haruyama, J., Hara, S., Hioki, K., Iwasaki, A., Morota, T., Ohtake, M., et al. (2012). Lunar
 1597 global digital terrain model dataset produced from SELENE (Kaguya) terrain camera stereo
 1598 observations. *43rd Lunar and Planetary Science Conference*, Lunar and Planetary Institute,
 1599 The Woodlands, Texas, abstract #1200.
- 1600 Hauri, E. H., Weinreich, T., Saal, A. E., Rutherford, M. C., & Van Orman, J. A. (2011). High
 1601 pre-eruptive water contents preserved in lunar melt inclusions. *Science*, 333(6039), 213-215.
 1602 <https://doi.org/10.1126/science.1204626>
- 1603 Hauri, E. H., Saal, A. E., Rutherford, M. J., & Van Orman, J. A. (2015). Water in the Moon's
 1604 interior: Truth and consequences. *Earth and Planetary Science Letters*, 409, 252-264.
 1605 <https://doi.org/j.epsl.2014.10.053>
- 1606 Head, J. W. (1976). Evidence for the sedimentary origin of Imbrium sculpture and lunar basin
 1607 radial texture. *The Moon*, 15, 445-462.
- 1608 Head, J. W. (1979). Serenitatis multi-ringed basin: Regional geology and basin ring
 1609 interpretation. *The Moon and the Planets*, 21, 439-462. <https://doi.org/10.1007/bf00897836>

- 1610 Head, J., & Gifford, A. (1980). Lunar mare domes: Classification and modes of origin. *The*
1611 *Moon and the Planets*, 22, 235-258. <https://doi.org/doi:10.1007/BF00898434>
- 1612 Head, J. W., & Wilson, L. (1992). Lunar mare volcanism: Stratigraphy, eruption conditions, and
1613 the evolution of secondary crusts. *Geochimica et Cosmochimica Acta*, 56(6), 2155-2175.
1614 [https://doi.org/10.1016/0016-7037\(92\)90183-J](https://doi.org/10.1016/0016-7037(92)90183-J)
- 1615 Head, J. W., & Wilson, L. (2017). Generation, ascent and eruption of magma on the Moon: New
1616 insights into source depths, magma supply, intrusions and effusive/explosive eruptions (Part 2:
1617 Predicted emplacement processes and observations). *Icarus*, 283, 176-223.
1618 <https://doi.org/10.1016/j.icarus.2016.05.031>
- 1619 Henriksen, M. R., Manheim, M. R., Burns, K. N., Seymour, P., Speyerer, E. J., Deran, A., et al.
1620 (2017). Extracting accurate and precise topography from LROC narrow angle camera stereo
1621 observations. *Icarus*, 283, 122-137. <https://doi.org/10.1016/j.icarus.2016.05.012>
- 1622 Hiesinger, H., Head, J. W., Wolf, U., Jaumann, R., & Neukum, G. (2011). Ages and stratigraphy
1623 of lunar mare basalts: A synthesis. *Geological Society of America Special Papers*, 477, 1-51.
1624 [https://doi.org/10.1130/2011.2477\(01\)](https://doi.org/10.1130/2011.2477(01))
- 1625 Hörz, F., Zolensky, M. E., Bernhard, R. P., See, T. H., & Warren, J. L. (2000). Impact features
1626 and projectile residues in aerogel exposed on Mir. *Icarus*, 147(2), 559-579.
1627 <https://doi.org/10.1006/icar.2000.6450>
- 1628 Housen, K. R., Holsapple, K. A., & Voss, M. E. (1999). Compaction as the origin of the unusual
1629 craters on the asteroid Mathilde. *Nature*, 402(6758), 155-157. <https://doi.org/10.1038/45985>
- 1630 Housen, K. R., & Holsapple, K. A. (2003). Impact cratering on porous asteroids. *Icarus*, 163(1),
1631 102-119. [https://dx.doi.org/10.1016/S0019-1035\(03\)00024-1](https://dx.doi.org/10.1016/S0019-1035(03)00024-1)
- 1632 Housen, K. R., & Holsapple, K. A. (2011). Ejecta from impact craters. *Icarus*, 211(1), 856-875.
1633 <https://doi.org/10.1016/j.icarus.2010.09.017>
- 1634 Kneissl, T., van Gasselt, S., & Neukum, G. (2011). Map-projection-independent crater size-
1635 frequency determination in GIS environments—New software tool for ArcGIS. *Planetary and*
1636 *Space Science*, 59(11–12), 1243-1254. <https://doi.org/10.1016/j.pss.2010.03.015>
- 1637 Kreslavsky, M. A., & Head, J. W. (2016). The steepest slopes on the Moon from Lunar Orbiter
1638 Laser Altimeter (LOLA) Data: Spatial distribution and correlation with geologic features.
1639 *Icarus*, 273, 329-336. <https://doi.org/10.1016/j.icarus.2016.02.036>
- 1640 Lemelin, M., Lucey, P. G., Song, E., & Taylor, G. J. (2015). Lunar central peak mineralogy and
1641 iron content using the Kaguya Multiband Imager: Reassessment of the compositional structure
1642 of the lunar crust. *Journal of Geophysical Research: Planets*, 120(5), 869-887.
1643 <https://doi.org/10.1002/2014je004778>
- 1644 Lucey, P. G., Blewett, D. T., & Jolliff, B. L. (2000a). Lunar iron and titanium abundance
1645 algorithms based on final processing of Clementine ultraviolet-visible images. *Journal of*
1646 *Geophysical Research: Planets*, 105(E8), 20297-20305. <https://doi.org/10.1029/1999je001117>
- 1647 Lucey, P. G., Blewett, D. T., Taylor, G. J., & Hawke, B. R. (2000b). Imaging of lunar surface
1648 maturity. *Journal of Geophysical Research: Planets*, 105(E8), 20377-20386.
1649 <https://doi.org/10.1029/1999je001110>
- 1650 Mangan, M.T., & Helz, R. T. (1986). *The distribution of vesicles and olivine phenocrysts in*
1651 *samples from drill hole KI 79-3, Kilauea Iki lava lake, Hawaii* (U. S. Geological Survey
1652 Open-File Report, 86–424).
- 1653 McKay, D. S., Heiken, G., Basu, A., Blanford, G., Simon, S., Reedy, R., et al. (1991). The lunar
1654 regolith. In G. H. Heiken, D. T. Vaniman, B. M. French (Eds.), *Lunar Sourcebook* (pp. 285–
1655 356). Cambridge: Cambridge University Press.

- 1656 Melosh, H. J. (1989). *Impact cratering: A geologic process*, London: Oxford University Press.
- 1657 Michael, G. G. & Neukum, G. (2010). Planetary surface dating from crater size-frequency
1658 distribution measurements: Partial resurfacing events and statistical age uncertainty. *Earth and*
1659 *Planetary Science Letters*, 294(3-4), 223-229. <https://doi.org/10.1016/j.epsl.2009.12.041>
- 1660 Michael, G. G., Kneissl, T., & Neesemann, A. (2016). Planetary surface dating from crater size-
1661 frequency distribution measurements: Poisson timing analysis. *Icarus*, 277, 279-285.
1662 <https://dx.doi.org/10.1016/j.icarus.2016.05.019>
- 1663 Michikami, T., K. Moriguchi, K., Hasegawa, S., & Fujiwara, A. (2007). Ejecta velocity
1664 distribution for impact cratering experiments on porous and low strength targets. *Planetary*
1665 *and Space Science*, 55(1-2), 70-88. <https://doi.org/10.1016/j.pss.2006.05.002>
- 1666 Moore, H. J., MacCormack, R. W., & Gault, D. E. (1963). Fluid impact craters and
1667 hypervelocity-high velocity impact experiments in metals and rocks. *Proceedings of 6th*
1668 *Hypervelocity Impact Symposium*, pp. 367-400.
- 1669 Morota, T., Haruyama, J., Ohtake, M., Matsunaga, T., Honda, C., Yokota, Y., et al. (2011).
1670 Timing and characteristics of the latest mare eruption on the Moon. *Earth and Planetary*
1671 *Science Letters*, 302(3-4), 255-266. <https://doi.org/10.1016/j.epsl.2010.12.028>
- 1672 Neish, C. D., Madden, J., Carter, L. M., Hawke, B. R., Giguere, T., Bray, V. J., Osinski, G. R., &
1673 Cahill, J. T. S. (2014). Global distribution of lunar impact melt flows. *Icarus*, 239, 105-117.
1674 <https://doi.org/10.1016/j.icarus.2014.05.049>.
- 1675 Neish, C. D., Hamilton, C. W., Hughes, S. S., Nawotniak, S. K., Garry, W. B., Skok, J. R., et al.
1676 (2017). Terrestrial analogues for lunar impact melt flows. *Icarus*, 281, 73-89.
1677 <https://doi.org/10.1016/j.icarus.2016.08.008>
- 1678 Neukum, G., Ivanov, B. A., & Hartmann, W. K. (2001). Cratering records in the inner solar
1679 system in relation to the lunar reference system. *Space Science Reviews*, 96(1-4), 55-86.
- 1680 Oberbeck, V., & Morrison R. (1974). Laboratory simulation of the herringbone pattern
1681 associated with lunar secondary crater chains, *The Moon*, 9(3-4), 415-455.
- 1682 Oberbeck, V. R., & Quaide, W. L. (1967). Estimated thickness of a fragmental surface layer of
1683 Oceanus Procellarum. *Journal of Geophysical Research*, 72(18), 4697-4704.
1684 <https://doi.org/10.1029/JZ072i018p04697>
- 1685 Papike, J. J., Hodges, F. N., Bence, A. E., Cameron, M., & Rhodes, J. M. (1976). Mare basalts:
1686 Crystal chemistry, mineralogy, and petrology. *Reviews of Geophysics*, 14(4), 475-540.
1687 <https://doi.org/10.1029/RG014i004p00475>
- 1688 Pasckert, J. H., Hiesinger, H., & van der Bogert, C. H. (2018). Lunar farside volcanism in and
1689 around the South Pole-Aitken basin. *Icarus*, 299(Supplement C), 538-562.
1690 <https://doi.org/10.1016/j.icarus.2017.07.023>
- 1691 Peck, D. L., & Kinoshita, W. T. (1976). *The eruption of August 1963 and the formation of Alae*
1692 *Lava Lake, Hawaii* (U.S. Geological Survey Professional Paper 935-A, pp. A1-B33).
1693 Washington: United States Government Printing Office.
- 1694 Pieters, C. M., & Noble, S. K. (2016). Space weathering on airless bodies. *Journal of*
1695 *Geophysical Research: Planets*, 121(10), 1865-1884. <https://doi.org/10.1002/2016JE005128>
- 1696 Pike, R. J., (1974). Depth/diameter relations of fresh lunar craters: Revision from spacecraft data.
1697 *Geophysical Research Letters*, 1(7), 291-294. <https://doi.org/10.1029/GL001i007p00291>.
- 1698 Pike, R. J., & Spudis, P. D. (1987). Basin-ring spacing on the Moon, Mercury, and Mars. *Earth,*
1699 *Moon, and Planets*, 39(2), 129-194. <https://doi.org/10.1007/bf00054060>

- 1700 Poelchau, M. H., Kenkmann, T., Thoma, K., Hoerth, T., Dufresne, A., & Schäfer, F. (2013). The
 1701 MEMIN research unit: Scaling impact cratering experiments in porous sandstones. *Meteoritics*
 1702 & *Planetary Science*, 48(1), 8-22. [https://doi.org/ 10.1111/maps.12016](https://doi.org/10.1111/maps.12016)
- 1703 Prieur, N. C., T. Rolf, T., Luther, R., Wünnemann, K., Xiao, Z., & Werner, S. C. (2017). The
 1704 effect of target properties on transient crater scaling for simple craters. *Journal of Geophysical*
 1705 *Research: Planets*, 122(8), 1704-1726. <https://doi.org/10.1002/2017JE005283>
- 1706 Qiao, L., Head, J. W., Xiao, L., Wilson, L., & Dufek, J. (2016). Sosigenes lunar irregular mare
 1707 patch (IMP): Morphology, topography, sub-resolution roughness and implications for origin.
 1708 *47th Lunar and Planetary Science Conference*, Lunar and Planetary Institute, The Woodlands,
 1709 Texas, abstract #2002.
- 1710 Qiao, L., Head, J., Wilson, L., Xiao, L., Kreslavsky, M., & Dufek, J. (2017). Ina pit crater on the
 1711 Moon: Extrusion of waning-stage lava lake magmatic foam results in extremely young crater
 1712 retention ages. *Geology*, 45(5), 455-458. <https://doi.org/10.1130/G38594.1>
- 1713 Qiao, L., Head, J. W., Xiao, L., Wilson, L., & Dufek, J. D. (2018a). The role of substrate
 1714 characteristics in producing anomalously young crater retention ages in volcanic deposits on
 1715 the Moon: Morphology, topography, sub-resolution roughness and mode of emplacement of
 1716 the Sosigenes Lunar Irregular Mare Patch (IMP). *Meteoritics & Planetary Science*, 53(4), 778-
 1717 812. <https://doi.org/10.1111/maps.13003>.
- 1718 Qiao, L., Head, J. W., Wilson, L., & Ling, Z. (2018b). Lunar irregular mare patch (IMP) sub-
 1719 types: Linking their origin through hybrid relationships displayed at Cauchy 5 small shield
 1720 volcano. *49th Lunar and Planetary Science Conference*. Lunar and Planetary Institute, The
 1721 Woodlands, Texas, abstract #1392.
- 1722 Qiao, L., Head, J. W., Xiao, L. & Wilson, L. (2018c). Exploration of lunar irregular mare patches
 1723 (IMPs): Testing models for their formation. *Lunar Science Targets for Landed Missions*,
 1724 NASA Ames Research Center, Moffett Field, California, abstract # LLW2018-55.
- 1725 Ravi, S., Mahanti, P., Meyer, H., & Robinson, M. S. (2016). On the usefulness of optical
 1726 maturity for relative age classification of fresh craters. *American Geophysical Union Fall*
 1727 *Meeting*, San Francisco, California, abstract #P53A-2166.
- 1728 Richter, D. H., Ault, W. U., Eaton, J. P., & Moore, J. G. (1964). *The 1961 eruption of Kilauea*
 1729 *volcano, Hawaii* (U.S. Geological Survey Professional Paper 474-D, pp. D1–B34).
 1730 Washington: United States Government Printing Office.
- 1731 Richter, D. H., & Moore, J. G. (1966). *Petrology of the Kilauea Iki lava lake, Hawaii* (U.S.
 1732 Geological Survey Professional Paper 537-B, pp. B1–B26). Washington: United States
 1733 Government Printing Office.
- 1734 Robinson, M. S., Brylow, S. M., Tschimmel, M., Humm, D., Lawrence, S. J., Thomas, P. C., et
 1735 al. (2010a). Lunar Reconnaissance Orbiter Camera (LROC) Instrument Overview. *Space*
 1736 *Science Reviews*, 150(1-4), 81-124. <https://doi.org/10.1007/s11214-010-9634-2>
- 1737 Robinson, M. S., Thomas, P. C., Braden, S. E., Lawrence, S. J., Garry, W. B., & LROC Team.
 1738 (2010b). High Resolution Imaging of Ina: Morphology, relative ages, formation. *41st Lunar*
 1739 *and Planetary Science Conference*, Lunar and Planetary Institute, The Woodlands, Texas,
 1740 abstract #2592.
- 1741 Rutherford, M. J., Head, J. W., Saal, A. E., Hauri, E., & Wilson, L. (2017). Model for the origin,
 1742 ascent, and eruption of lunar picritic magmas. *American Mineralogist*, 102(10), 2045-2053.
 1743 <https://dx.doi.org/10.2138/am-2017-5994ccbyncnd>

- 1744 Saal, A. E., Hauri, E. H., Cascio, M. L., Van Orman, J. A., Rutherford, M. C., & Cooper, R. F.
 1745 (2008). Volatile content of lunar volcanic glasses and the presence of water in the Moon's
 1746 interior. *Nature*, 454, 192. <https://doi.org/10.1038/nature07047>
- 1747 Schaber, G. G. (1973). Lava flows in Mare Imbrium: Geologic evaluation from Apollo orbital
 1748 photography. In *Proceedings of the 4th Lunar and Planetary Science* (Vol. 1, pp. 73-92).
- 1749 Schaber, G. G., Boyce, J. M., & Moore, H. J. (1976). The scarcity of mappable flow lobes on the
 1750 lunar maria: The unique morphology of the Imbrium flows. *Proceedings of 7th Lunar and*
 1751 *Planetary Science*, 2783–2800.
- 1752 Schultz, P. H., & Spencer J. (1979). Effects of substrate strength on crater statistics: Implications
 1753 for surface ages and gravity scaling. *Tenth Lunar and Planetary Science Conference*, Lunar
 1754 and Planetary Institute, Houston, Texas, abstract #1380.
- 1755 Schultz, P., & Spudis, P. (1983). Beginning and end of lunar mare volcanism. *Nature*,
 1756 302(5905), 233-236. <https://doi.org/10.1038/302233a0>
- 1757 Schultz, P. H., Anderson, J. L. B., & Heineck, J. T. (2002). Impact crater size and evolution:
 1758 Expectations for Deep Impact. *33rd Lunar and Planetary Science Conference*, Lunar and
 1759 Planetary Institute, League City, Texas, abstract #1875.
- 1760 Schultz, P. H., Staid, M. I., & Pieters, C. M. (2006). Lunar activity from recent gas release.
 1761 *Nature*, 444(7116), 184-186. <https://doi.org/10.1038/nature05303>
- 1762 Schultz, P. H., & Crawford, D. A. (2016). Origin and implications of non-radial Imbrium
 1763 Sculpture on the Moon. *Nature*, 535(7612), 391-394. <https://doi.org/10.1038/nature18278>
- 1764 Shkuratov, Y., Kaydash, V., & Videen, G. (2012). The lunar crater Giordano Bruno as seen with
 1765 optical roughness imagery. *Icarus*, 218(1), 525-533.
 1766 <https://dx.doi.org/10.1016/j.icarus.2011.12.023>
- 1767 Shoemaker, E. M. (1962). Interpretation of lunar craters. In Z. Kopal (Eds.) *Physics and*
 1768 *astronomy of the Moon* (pp. 283-360). New York: Academic Press.
- 1769 Smith, D. E., Zuber, M. T., Jackson, G. B., Cavanaugh, J. F., Neumann, G. A., Riris, H., et al.
 1770 (2010). The Lunar Orbiter Laser Altimeter Investigation on the Lunar Reconnaissance Orbiter
 1771 Mission. *Space Science Reviews*, 150(1), 209-241. [https://dx.doi.org/10.1007/s11214-009-](https://dx.doi.org/10.1007/s11214-009-9512-y)
 1772 [9512-y](https://dx.doi.org/10.1007/s11214-009-9512-y)
- 1773 Soderblom, L. A. (1970). A model for small-impact erosion applied to the lunar surface. *Journal*
 1774 *of Geophysical Research*, 75(14), 2655-2661. <https://dx.doi.org/10.1029/JB075i014p02655>
- 1775 Solomon, S. C., & Head, J. W. (1980). Lunar Mascon Basins: Lava filling, tectonics, and
 1776 evolution of the lithosphere. *Reviews of Geophysics*, 18(1), 107-141.
 1777 <https://dx.doi.org/10.1029/RG018i001p00107>
- 1778 Spudis, P. D. (1993). *The Geology of Multi-Ring Impact Basins*, Cambridge: Cambridge
 1779 University Press.
- 1780 Stöffler, D., & Ryder, G. (2001). Stratigraphy and isotope ages of lunar geologic units:
 1781 Chronological standard for the inner solar system. *Space Science Reviews*, 96(1-4), 9-54.
 1782 <https://dx.doi.org/10.1023/a:1011937020193>
- 1783 Stooke, P. J. (2012). Lunar meniscus hollows. *43rd Lunar and Planetary Science Conference*,
 1784 Lunar and Planetary Institute, The Woodlands, Texas, abstract #1011.
- 1785 Staid, M., Isaacson, P., Petro, N., Boardman, J., Pieters, C. M., Head, J. W., et al. (2011). The
 1786 spectral properties of Ina: New observations from the Moon Mineralogy Mapper. *42nd Lunar*
 1787 *and Planetary Science Conference*, Lunar and Planetary Institute, The Woodlands, Texas,
 1788 abstract #2499.

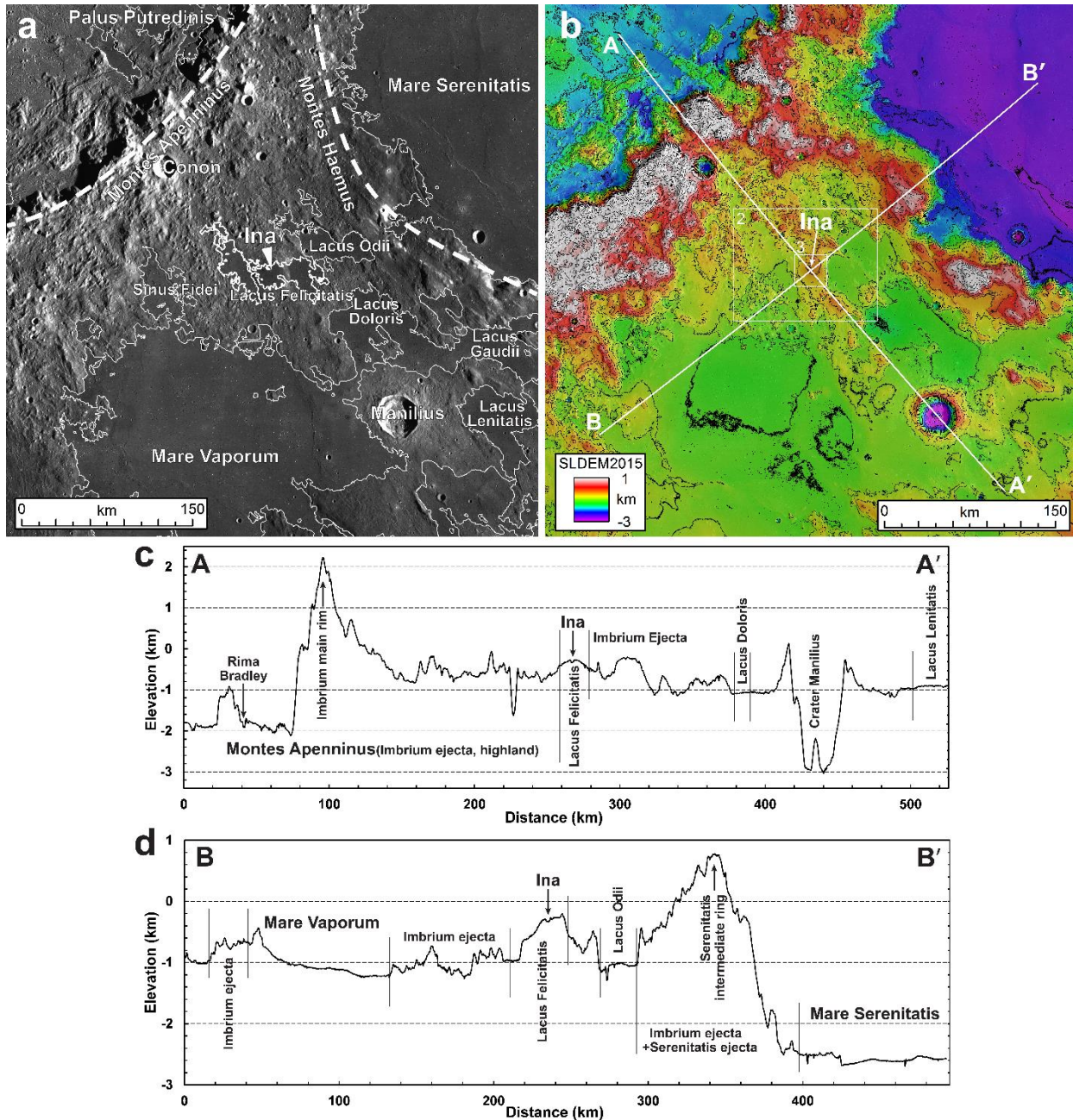
- 1789 Strain, P. L., & El-Baz, F. (1980). The geology and morphology of Ina. In *Proceedings of the*
 1790 *11th Lunar Science Conference* (pp. 2437-2446).
- 1791 Trask, N. J. (1966). Size and spatial distribution of craters estimated from the Ranger
 1792 photographs, In *Ranger VIII and IX, Part II, Experimenters' Analyses and Interpretations*
 1793 (JPL Technical Reports 32-800, pp. 252-264). Pasadena, CA: Jet Propulsion Lab.
- 1794 Tye, A. R., & Head, J. W. (2013). Mare Tranquillitatis: Distribution of mare domes, relation to
 1795 broad mare rise, and evidence of a previously unrecognized basin from LOLA altimetric data.
 1796 *44th Lunar and Planetary Science Conference*, Lunar and Planetary Institute, The Woodlands,
 1797 Texas, abstract #1319.
- 1798 Valantinas, A., Kinch, K. M. & Bridžius, A. (2018), Low crater frequencies and low model ages
 1799 in lunar maria: Recent endogenic activity or degradation effects? *Meteoritics & Planetary*
 1800 *Science*, 53(4), 826-828. <https://doi.org/10.1111/maps.13033>.
- 1801 van der Bogert, C. H., Hiesinger, H., Dundas, C. M., Krüger, T., McEwen, A. S., Zanetti, M., &
 1802 Robinson, M. S. (2017). Origin of discrepancies between crater size-frequency distributions of
 1803 coeval lunar geologic units via target property contrasts. *Icarus*, 298(Supplement C), 49-63.
 1804 <https://doi.org/10.1016/j.icarus.2016.11.040>
- 1805 van der Bogert, C. H., Michael G., Kneissl T., Hiesinger H., & Pasckert J. H. (2015). Effects of
 1806 count area size on absolute model ages derived from random crater size-frequency
 1807 distributions. *46th Lunar and Planetary Science Conference*, Lunar and Planetary Institute,
 1808 The Woodlands, Texas, abstract #1742.
- 1809 Vaughan, W. M. & Head, J. W. (2012). Ina: Lunar Sublimation Terrain? *5th annual NASA Lunar*
 1810 *Science Forum*. NASA Lunar Science Institute, Moffett Field, California.
- 1811 Wagner, R., Denevi, B. W., Stopar, J. D., van der Bogert, C. H. & Robinson, M. S. (2018). The
 1812 age of Ina and the thermal history of the Moon. *Lunar Science Targets for Landed Missions*,
 1813 NASA Ames Research Center, Moffett Field, California, abstract #LLW2018-15.
- 1814 Whitaker, E. A. (1972). An unusual mare feature, In *Apollo 15 Preliminary Science Report*
 1815 (NASA SP-289, pp. 25-84–25-85).
- 1816 Wieczorek, M. A., Neumann, G. A., Nimmo, F., Kiefer, W. S., Taylor, G. J., Melosh, H. J., et al.
 1817 (2013). The crust of the Moon as seen by GRAIL. *Science*, 339(6120), 671-675.
 1818 <https://doi.org/10.1126/science.1231530>
- 1819 Wilson, L., & Head, J. W. (2003). Lunar Gruithuisen and Mairan domes: Rheology and mode of
 1820 emplacement. *Journal of Geophysical Research: Planets*, 108(E2), 5012.
 1821 <https://doi.org/10.1029/2002je001909>
- 1822 Wilson, L., B. R., Giguere, T. A., & Petrycki, E. R. (2011). An igneous origin for Rima Hyginus
 1823 and Hyginus crater on the Moon. *Icarus*, 215(2), 584-595.
 1824 <https://doi.org/10.1016/j.icarus.2011.07.003>
- 1825 Wilson, L., & Head, J. W. (2017a). Generation, ascent and eruption of magma on the Moon:
 1826 New insights into source depths, magma supply, intrusions and effusive/explosive eruptions
 1827 (Part 1: Theory). *Icarus*, 283, 146-175. <https://doi.org/10.1016/j.icarus.2015.12.039>.
- 1828 Wilson, L., & Head, J. W. (2017b). Eruption of magmatic foams on the Moon: Formation in the
 1829 waning stages of dike emplacement events as an explanation of “irregular mare patches”.
 1830 *Journal of Volcanology and Geothermal Research*, 335, 113-127.
 1831 <https://doi.org/10.1016/j.jvolgeores.2017.02.009>.
- 1832 Wilson, L., & Head, J. W. (2018). Controls on lunar basaltic volcanic eruption structure and
 1833 morphology: Gas release patterns in sequential eruption phases. *Geophysical Research Letters*,
 1834 45, 5852–5859. <https://doi.org/10.1029/2018GL078327>

- 1835 Wright, T. L., Peck, D. L. & Shaw, H. R. (1976). Kīlauea lava lakes: natural laboratories for
1836 study of cooling, crystallization and differentiation of basaltic magma. In G. H. Sutton, M. H.
1837 Manghnani, R Moberly, E U Mcafee (Eds), *The Geophysics of the Pacific Ocean Basin and Its*
1838 *Margin* (pp. 975-390). Washington, DC: American Geophysical Union.
1839 <https://doi.org/10.1029/GM019p0375>
- 1840 Wünnemann, K., Collins, G. S., & Melosh, H. J. (2006). A strain-based porosity model for use in
1841 hydrocode simulations of impacts and implications for transient crater growth in porous
1842 targets. *Icarus*, 180(2), 514-527. <https://dx.doi.org/10.1016/j.icarus.2005.10.013>
- 1843 Wünnemann, K., Nowka D., Collins G. S., Elbeshausen D., & Bierhaus M. (2011). Scaling of
1844 impact crater formation on planetary surfaces – Insights from numerical modeling, In
1845 *Proceedings of the 11th Hypervelocity Impact Symposium*, Fraunhofer, Freiburg, Germany, 1-
1846 16.
- 1847 Wünnemann, K., Marchi S., Nowka D., and Michel P. (2012). The effect of target properties on
1848 impact crater scaling and the lunar crater chronology. *43rd Lunar and Planetary Science*
1849 *Conference*, Lunar and Planetary Institute, The Woodlands, Texas, abstract #1805.
- 1850 Xiao, Z., Zeng, Z., Ding, N., & Molaro, J. (2013). Mass wasting features on the Moon – how
1851 active is the lunar surface? *Earth and Planetary Science Letters*, 376, 1-11.
1852 <https://doi.org/10.1016/j.epsl.2013.06.015>
- 1853 Xiao, Z., & Werner, S. C. (2015). Size-frequency distribution of crater populations in
1854 equilibrium on the Moon. *Journal of Geophysical Research: Planets*, 120(12), 2277-2292.
1855 <https://doi.org/10.1002/2015JE004860>
- 1856 Zhang, F., Head, J. W., Basilevsky, A. T., Bugiolacchi, R., Komatsu, G., Wilson, L., . . . Zhu,
1857 M.-H. (2017). Newly discovered ring-moat dome structures in the lunar maria: Possible
1858 origins and implications. *Geophysical Research Letters*, 44(18), 9216-9224.
1859 <https://doi.org/10.1002/2017GL074416>

1860 **Table**

1861 **Table 1.** Statistics of Numbers (#) of Impact Crater Counts with Several Diameter (D) Ranges on
 1862 the Ina Interior Mounds (Figure 16a) and Floor Units (Figure 16a), and Surrounding Shield
 1863 Volcano Surface Regions with Same Areas and Shapes as Ina Interior Units (Figure 16b).

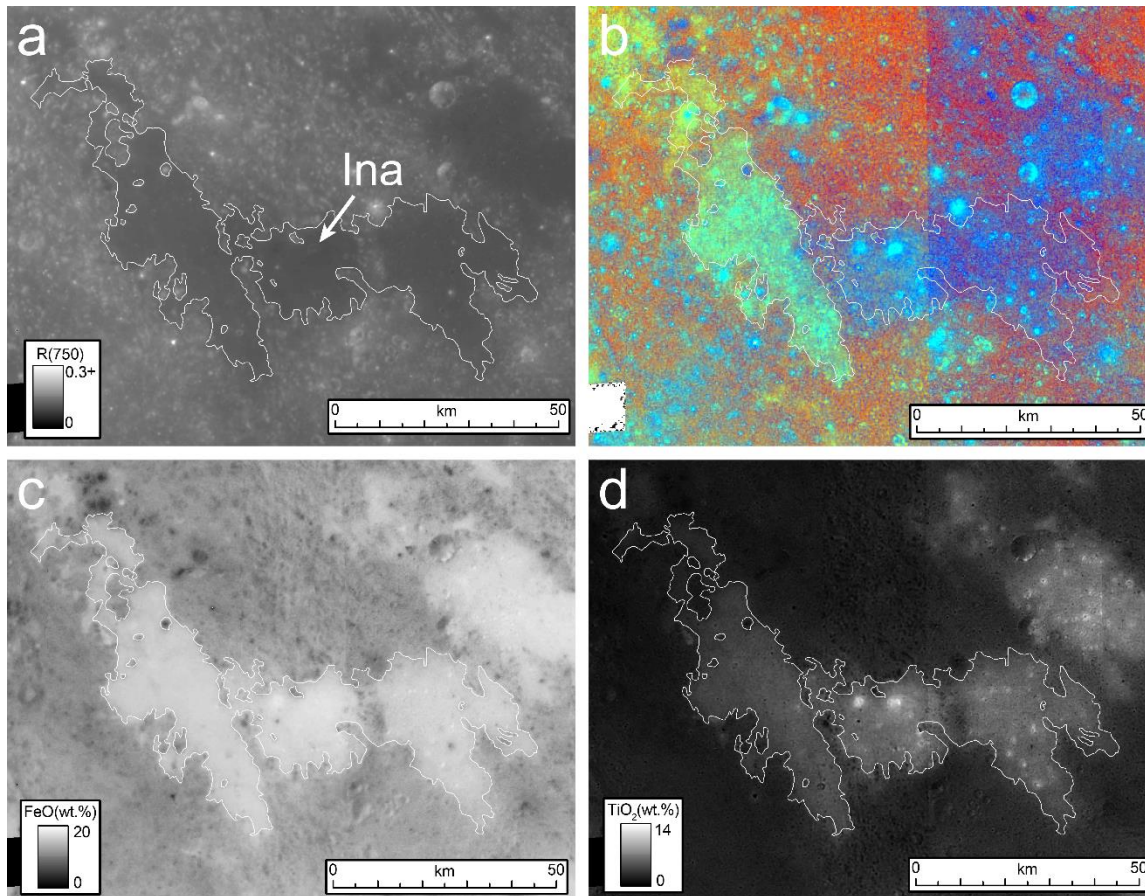
Count area	Size of counting area (km ²)	# of craters D≥10 m	# of craters D≥25 m	# of craters D≥50 m
Ina mounds	2.27	542	25	3
Ina floor	2.28	378	32	4
Surrounding “mounds”	2.27	1506	135	50
Surrounding “floor”	2.28	1547	139	55

1864 **Figures**

1865

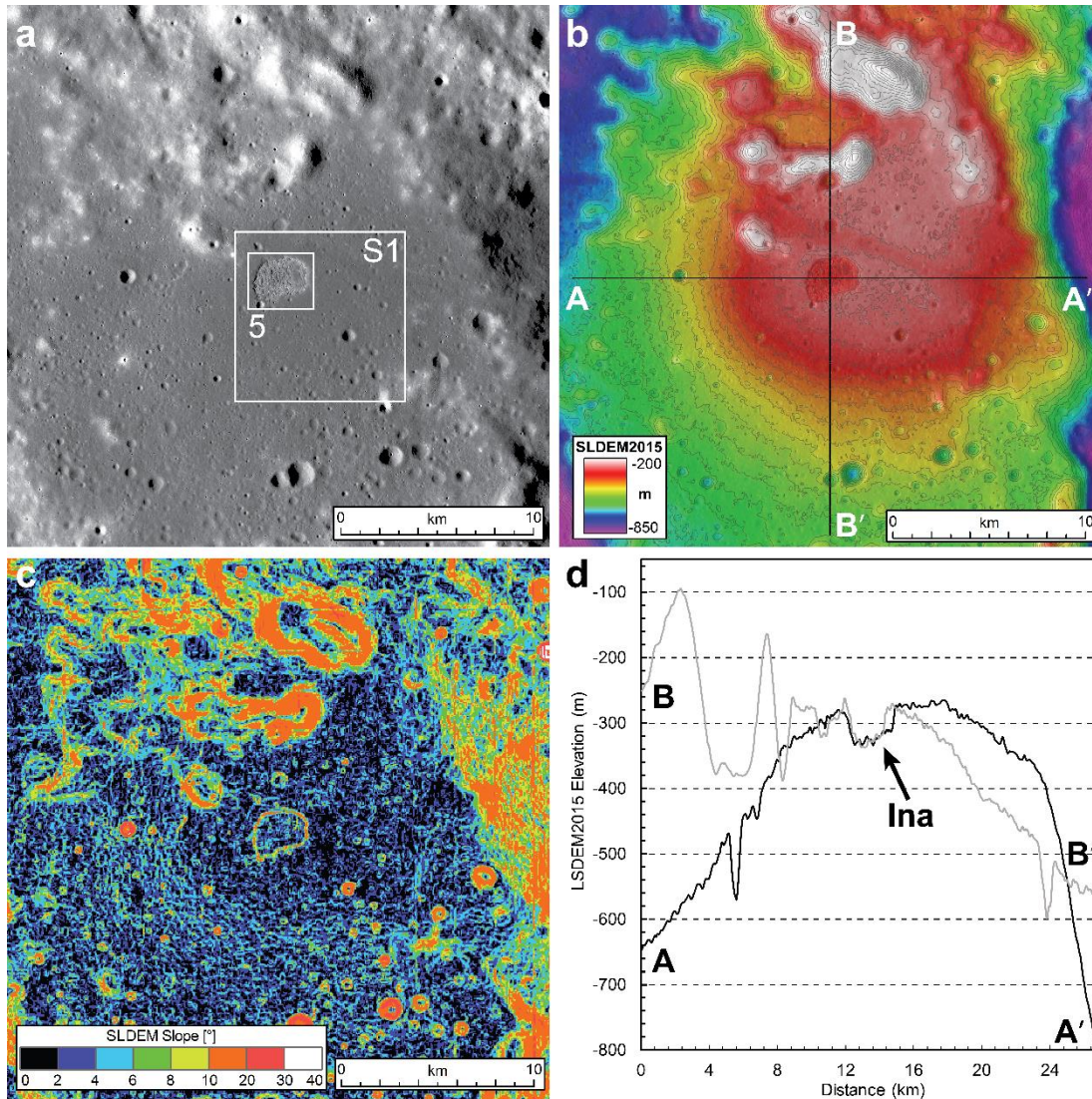
1866 **Figure 1.** (a) Major physiographic features within the regional context of Ina. The Ina feature is
 1867 marked by the white arrow (center); the approximate locations of parts of the Imbrium basin
 1868 main ring ($D = 1160$ km; Pike & Spudis, 1987) and Serenitatis basin intermediate ring ($D = 613$
 1869 km; Head, 1979) are marked by the bold dashed white curves; the multiple mare regions are
 1870 labeled by their nomenclature, with their boundaries marked by the thin solid white outlines. The
 1871 extent of Lacus Felicitatis, in which Ina occurs, is highlighted by a thicker white outline. The
 1872 background image is a portion of the LROC-WAC nearside low-sun mosaic, pixel size is 100 m.
 1873 (b) Topographic map of the regional context of the Ina feature. Ina is indicated by the white
 1874 arrow. The white lines mark the locations of the two topographic profiles shown in panels c,d,

1875 and the white boxes mark the locations of Figures 2 and 3. Contour interval is 300 m.
 1876 Topography data are derived from the SELENE-TC+LRO-LOLA merged DEM (SLDEM2015,
 1877 Barker et al., 2016). (c) NW-SE and (d) SW-NE topographic profile derived from SLDEM2015
 1878 topography, showing the major topographic features (labeled by their nomenclature) of the
 1879 regional context of the Ina feature, in a direction radial to the center of the Imbrium basin and
 1880 Serenitatis basin, respectively. See panel b for its location. All the maps for the Ina region in this
 1881 paper are projected into a sinusoidal projection with a central meridian of 5.3473°E, and north is
 1882 up.



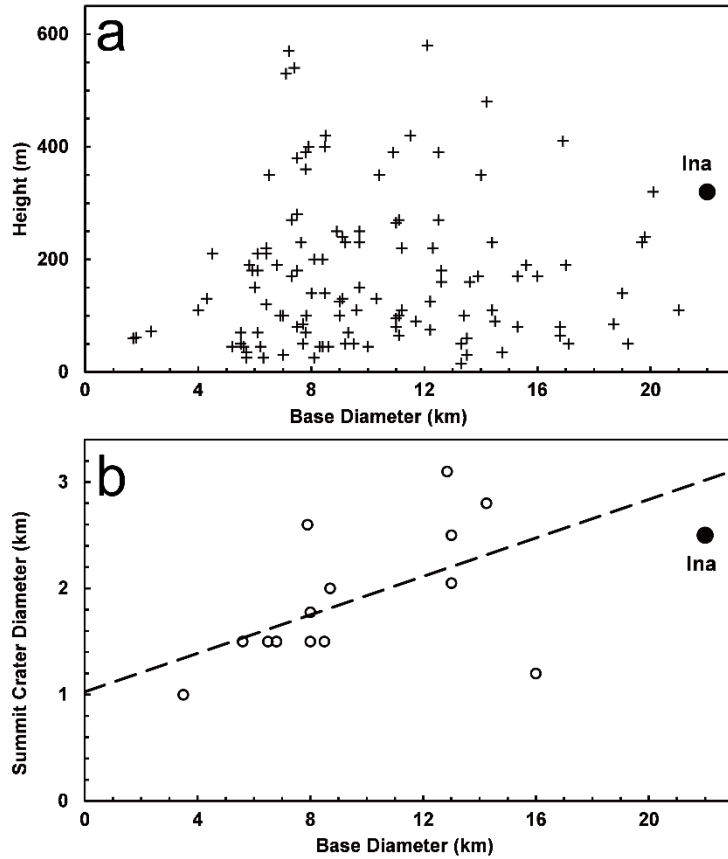
1883

1884 **Figure 2.** Clementine UVVIS maps of Lacus Felicitatis: (a) 750 nm reflectance, (b) color ratio
 1885 composite (red channel = 750/415 nm, green channel = 750/950 nm and blue channel = 415/750
 1886 nm), (c) FeO and (d) TiO₂ abundance calculated from the Lucey et al. (2000a) algorithm. The
 1887 boundary of Lacus Felicitatis is shown by the white outline, and Ina is marked by the white
 1888 arrow in panel (a).



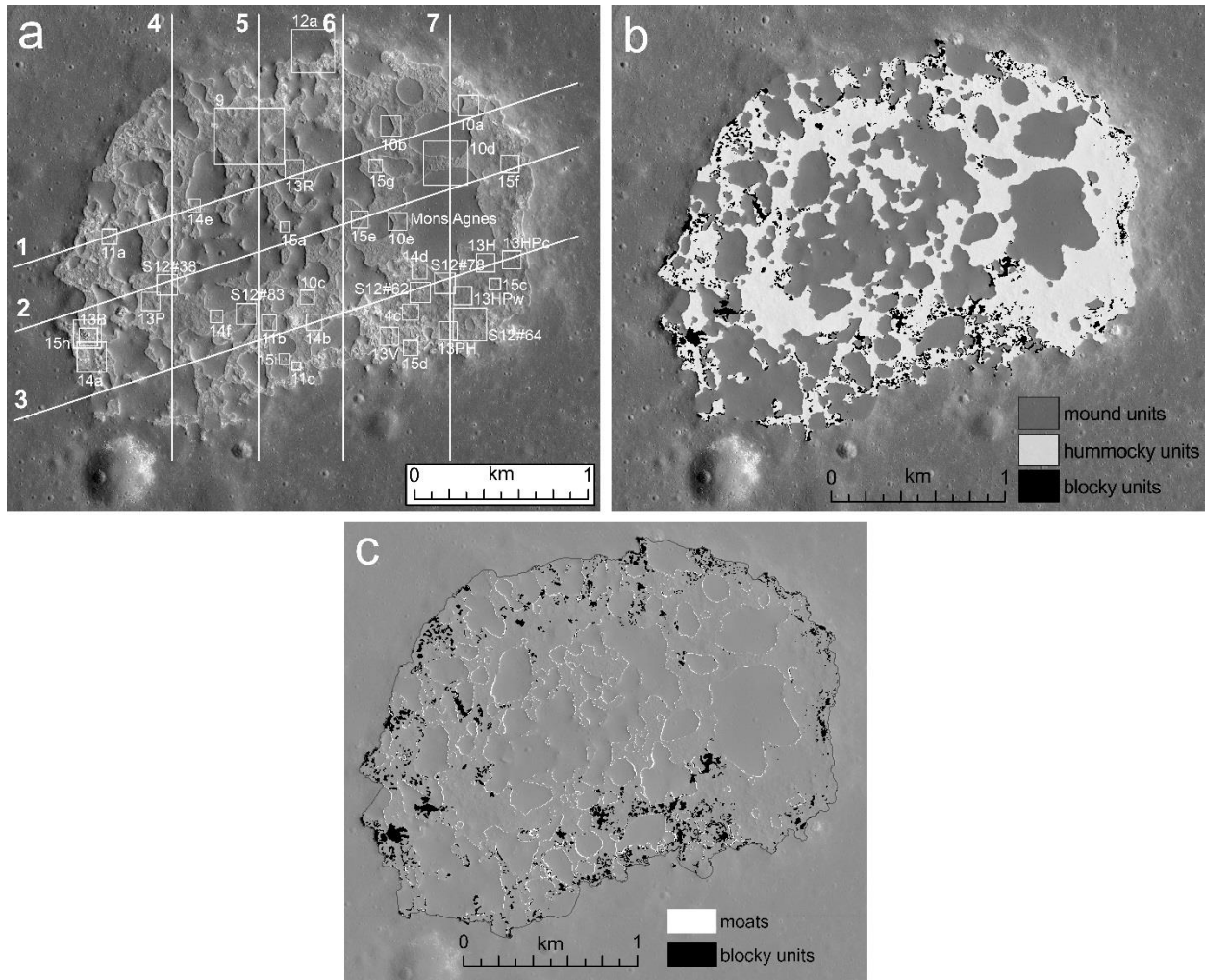
1889

1890 **Figure 3.** Image and topography of the small shield volcano on which the Ina feature sits. (a)
 1891 Portion of Kaguya TC evening image mosaic TCO_MAPe04_N21E003N18E006SC, 10 m/pixel.
 1892 White boxes mark the locations of Figures 5 (also 6, 13 upper panel, 16a, S2, S10, S11, S14, S15
 1893 and S19) and S1. (b) SLDEM2015 topography overlain on Kaguya TC evening mosaic. The
 1894 black lines mark the locations of the two elevation profiles shown in panel (d). (c) SLDEM2015-
 1895 derived topographic slope map, with a baseline of ~180 m. (d) West-east (A-A') and north-south
 1896 (B-B') topographic profiles across the small shield, with Ina location marked by the black arrow.



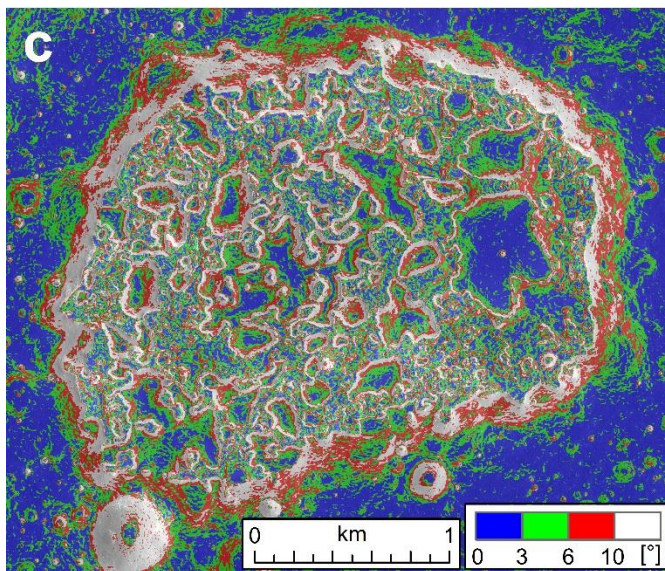
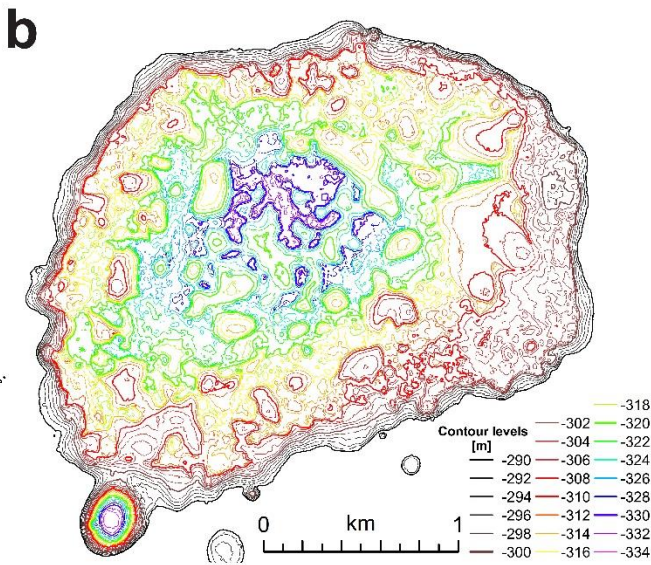
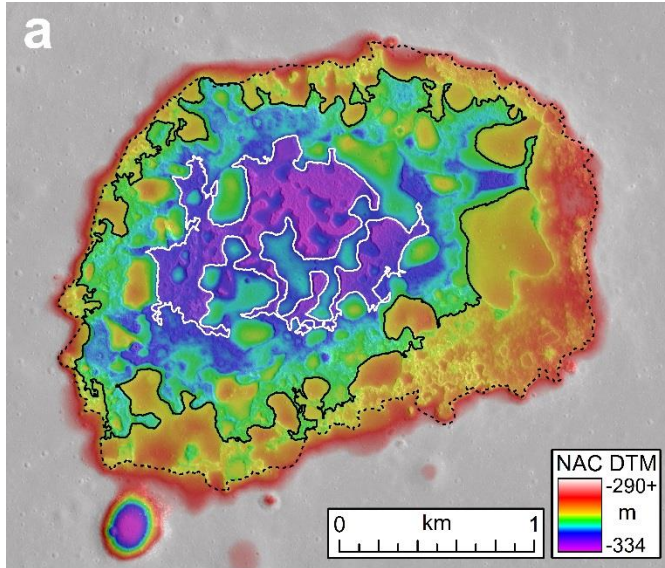
1897

1898 **Figure 4.** (a) Base diameter-height plot for lunar small shield volcanoes catalogued by
 1899 Consolidated Lunar Dome Catalogue (crosses; <http://digilander.libero.it/glrgroup/cldc.htm>) and
 1900 the Ina shield (black dot) and (b) base diameter-summit pit crater diameter plot for small lunar
 1901 shield volcanoes catalogued in Head & Gifford (1980) (circles) and Ina shield (black dot).



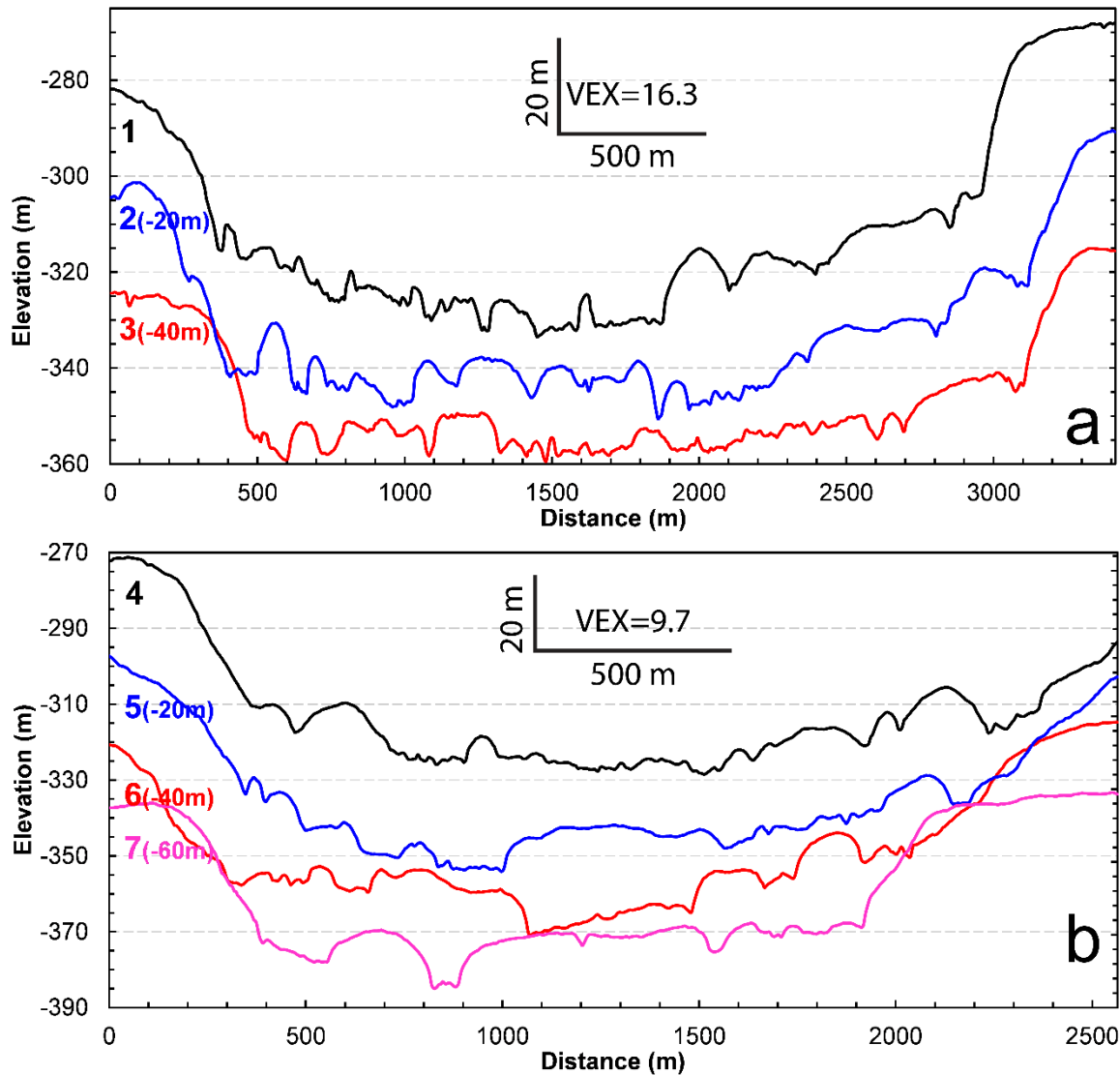
1902

1903 **Figure 5.** (a) Ina pit crater interior imaged by LROC NAC frame M119815703, pixel size = 0.48
 1904 m, incidence angle = $\sim 56^\circ$. The white lines mark the locations of topographic profiles shown in
 1905 Figure 7, with their starting points labeled by the profile numbers, and the white boxes mark the
 1906 locations of Figures 9-15 and S12. (b) Geologic sketch map shows the spatial distribution of the
 1907 multiple morphologic units of Ina interior; background is a portion of LROC NAC M119815703.
 1908 (c) Spatial distribution of moats (white lines, surrounding mounds) and blocky units (black
 1909 patches) within Ina.



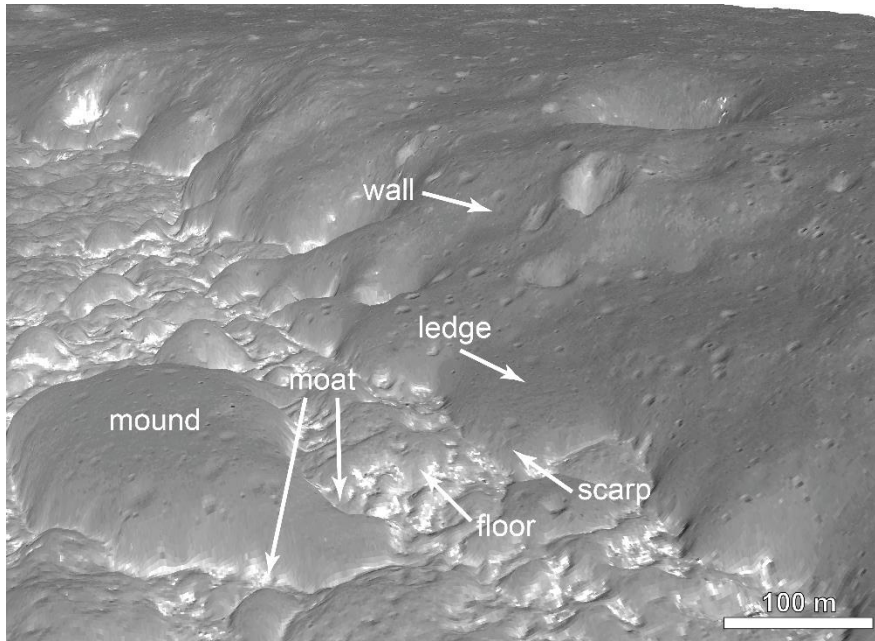
1910

1911 **Figure 6.** (a) Topographic variations of the Ina pit crater floor: colorized NAC DTM topography
 1912 overlay on LROC NAC M119815703. The black dashed outline marks the boundary of the Ina
 1913 interior floor, and the black and white solid lines are the contours -314 m and -324 m,
 1914 respectively, to define the three annular terraces of the floor topography (see the details in
 1915 section 3.4 and Figure S14). (b) LROC NAC DTM-derived contour map of the Ina interior,
 1916 contour interval is 2 m (modified from Fig. DR1 of Qiao et al. (2017)). (c) NAC DTM slope map
 1917 for the Ina pit crater, overlay on LROC NAC M119815703.



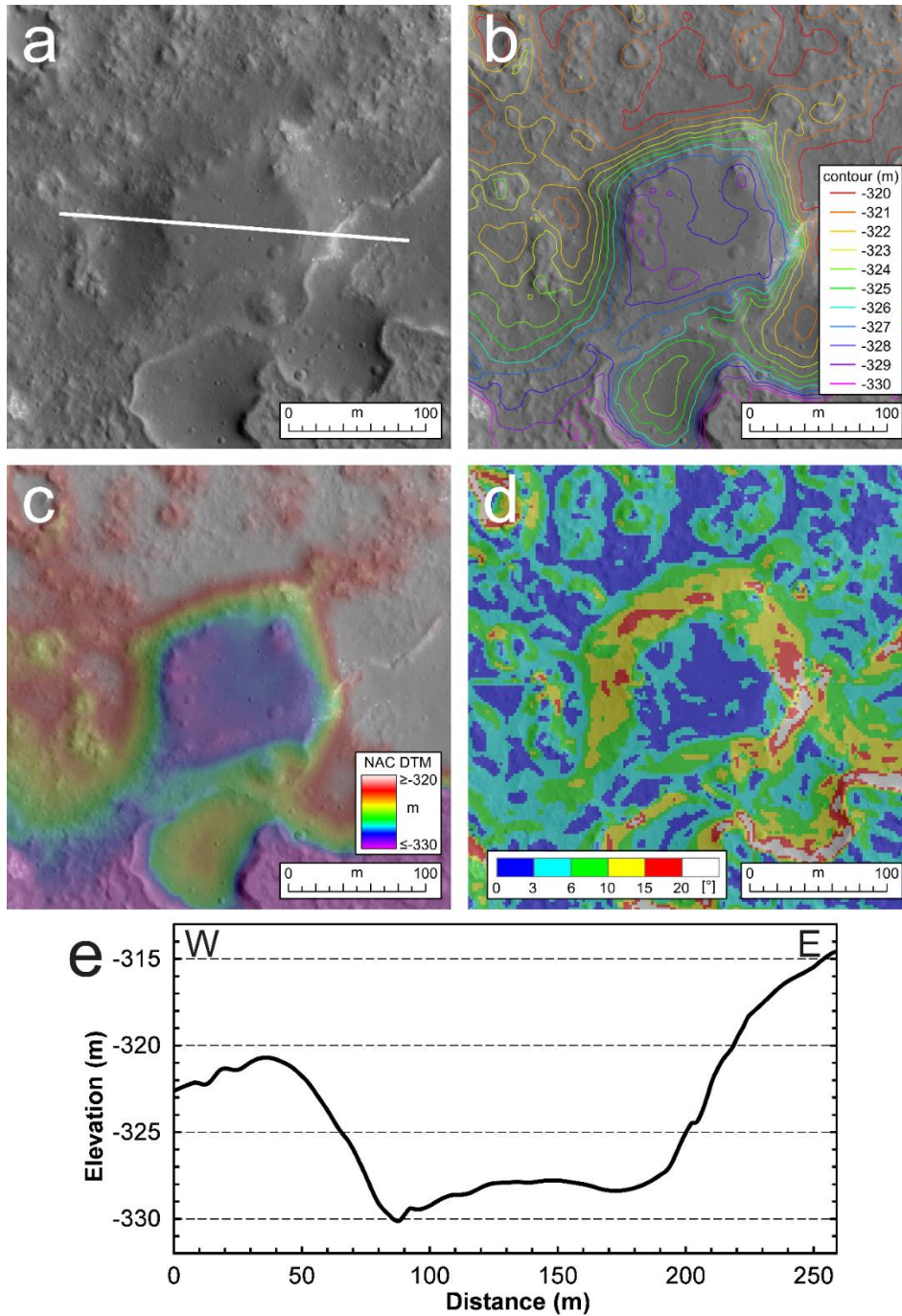
1918

1919 **Figure 7.** (a) West-east and (b) north-south topographic profiles crossing the Ina interior, derived
 1920 from NAC DTM topography, with vertical exaggeration (VEX) labeled. The locations of these
 1921 profiles are shown in Figure 5a, and the profile numbers correspond to those shown there. For
 1922 clarity, profiles in each panel are offset by -20 m in succession.



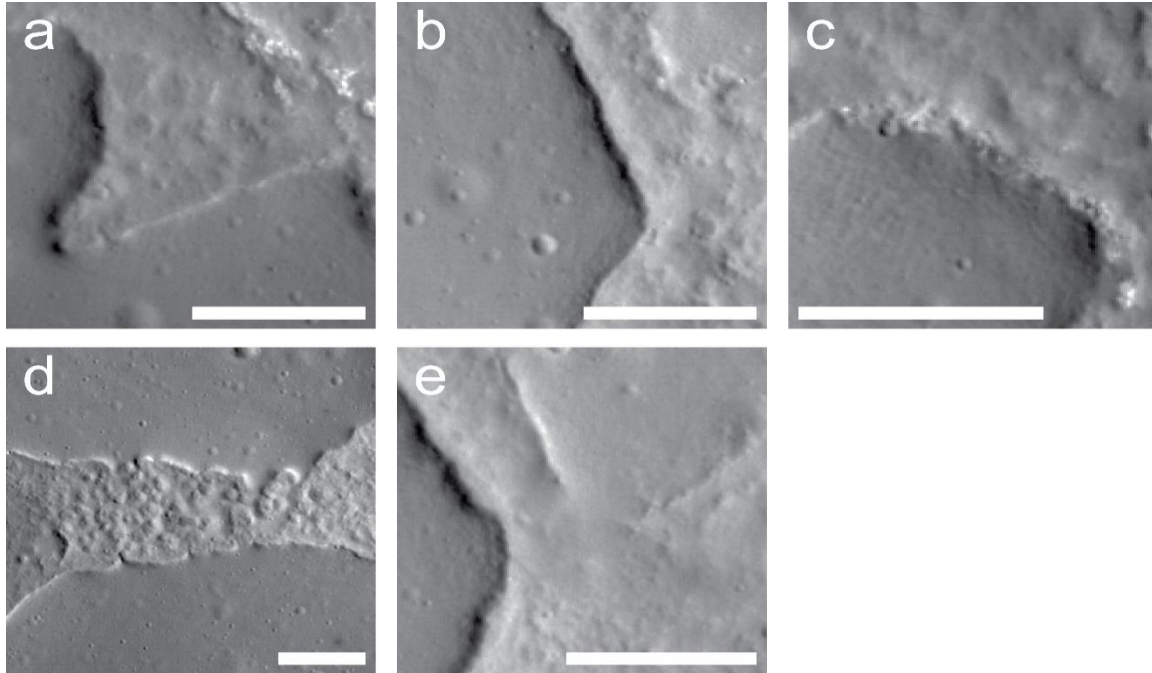
1923

1924 **Figure 8.** Perspective view of southern middle edge of the Ina interior, showing the
1925 morphological transition from the shield volcano (including wall, ledge and scarp) to Ina floor
1926 (including floor terrains and mounds with surrounding moats). LROC NAC frame M119815703
1927 overlain on LROC NAC DTM topography. View is looking southeast and vertical exaggeration
1928 is ~5.0.



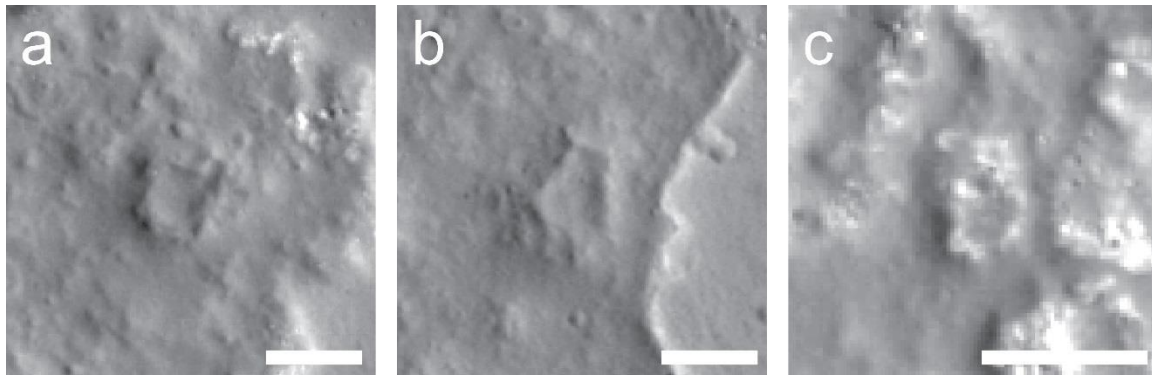
1929

1930 **Figure 9.** The largest “low mound” (topographically lower, while smoothly textured terrain) of
 1931 the Ina interior, with a diameter of ~200 m. (a) Portion of LROC NAC M119815703; the
 1932 location of the topographic profiles shown in (e) is marked by the white line, (b) NAC DTM-
 1933 derived contour overlay on LROC NAC M119815703; contour interval is 1 m, (c) colorized
 1934 NAC DTM topography overlay on LROC NAC M119815703, (c) NAC DTM-derived
 1935 topographic slope, and (e) west-east topographic profile across this depression feature.



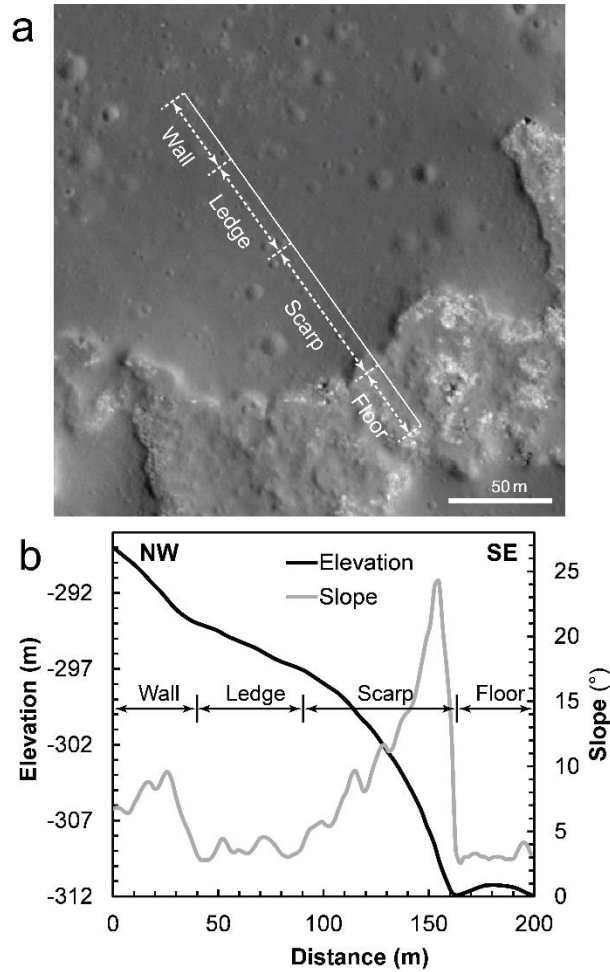
1936

1937 **Figure 10.** Morphologies of the mound-floor transition area: (a) clearly-defined boundary, (b)
1938 topographically lower moat occurring at the transition, (c) blocky materials exposed in the moats,
1939 (d) gradual finger-like morphologic transitions and (e) continuous morphologic transitions. All
1940 panels are portions of LROC NAC frame M119815703, and each scale is 50 m.



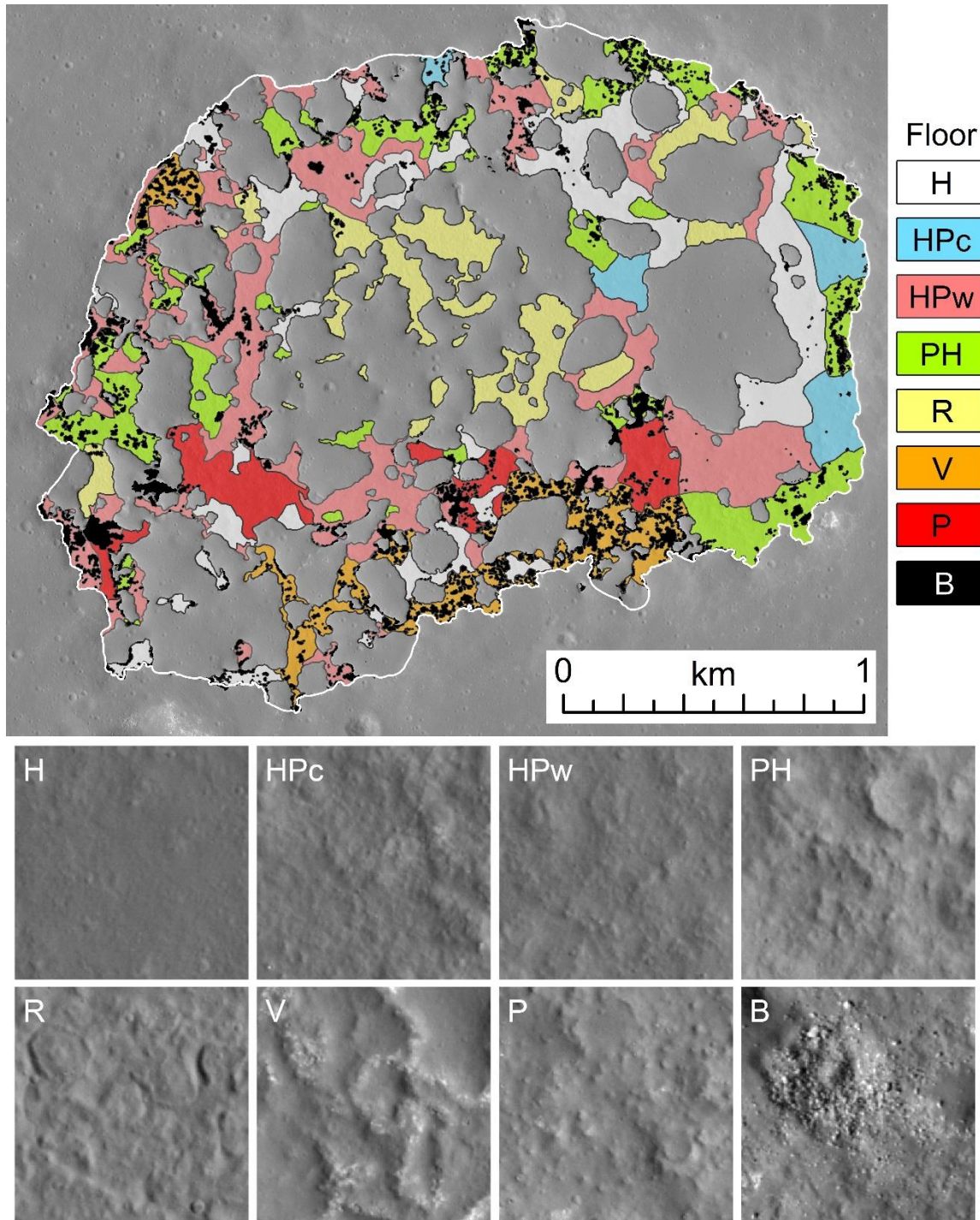
1941

1942 **Figure 11.** Unusual depressions with a relatively extensive central uplifted structure, on the floor
1943 units: (a) circular, (b) elliptical, and (b) rocky materials within the marginal ring of low-lying
1944 areas. All panels are portions of LROC NAC frame M119815703, and each scale is 20 m.



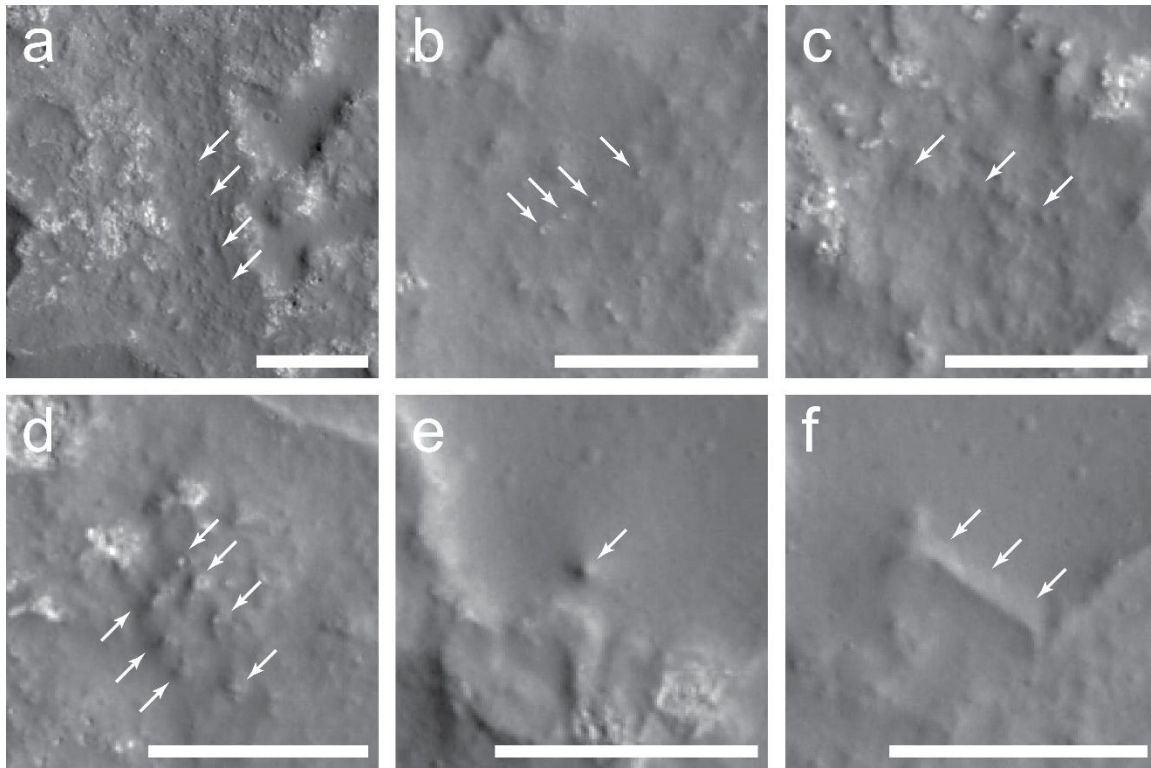
1945

1946 **Figure 12.** A sample of ledges and scarps observed at the north margin of Ina: (a) LROC NAC
 1947 images (portion of LROC NAC M119815703), and (b) NAC DTM elevation (black curve) and
 1948 slope (grey curve). The approximate extents of each morphologic unit (wall, ledge, scarp and
 1949 floor) are marked.



1950

1951 **Figure 13.** Geomorphological division of the Ina floor terrains (above): H: fine-textured and
 1952 hummocky units, HPc: hummocky and moderately pitted units, with closely-spaced pits and
 1953 ridges, HPw: hummocky and moderately pitted units, with wide-spaced pits and ridges, PH:
 1954 hummocky and highly pitted units, R: ridged and pitted units, V: vermicular units, P: pitted units,
 1955 B: blocky units (see texts in section 3.5 for the detailed description of each unit). The LROC
 1956 NAC images (below) show the examples of each unit; each panel is 106×106 m.

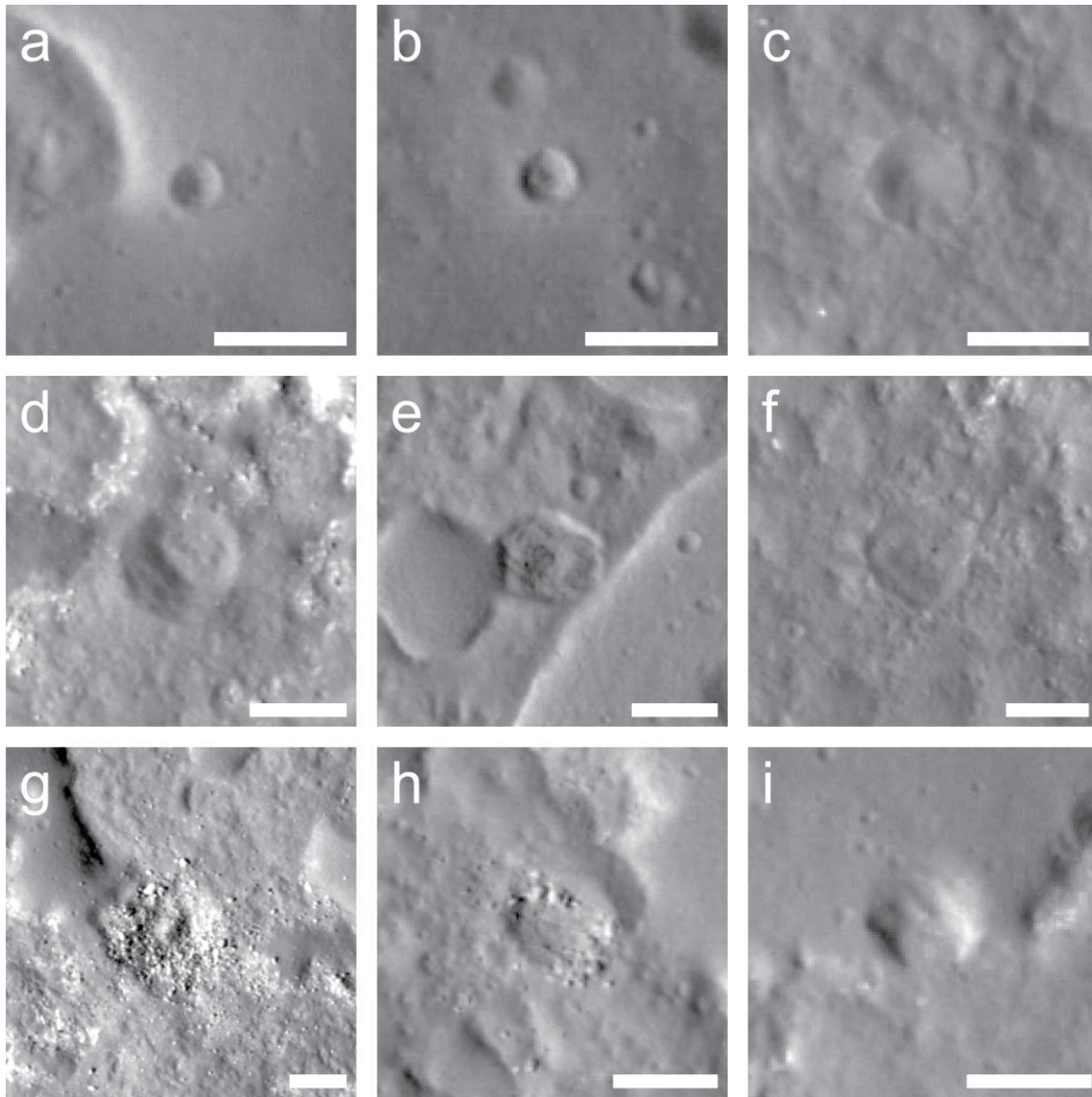


1957

1958

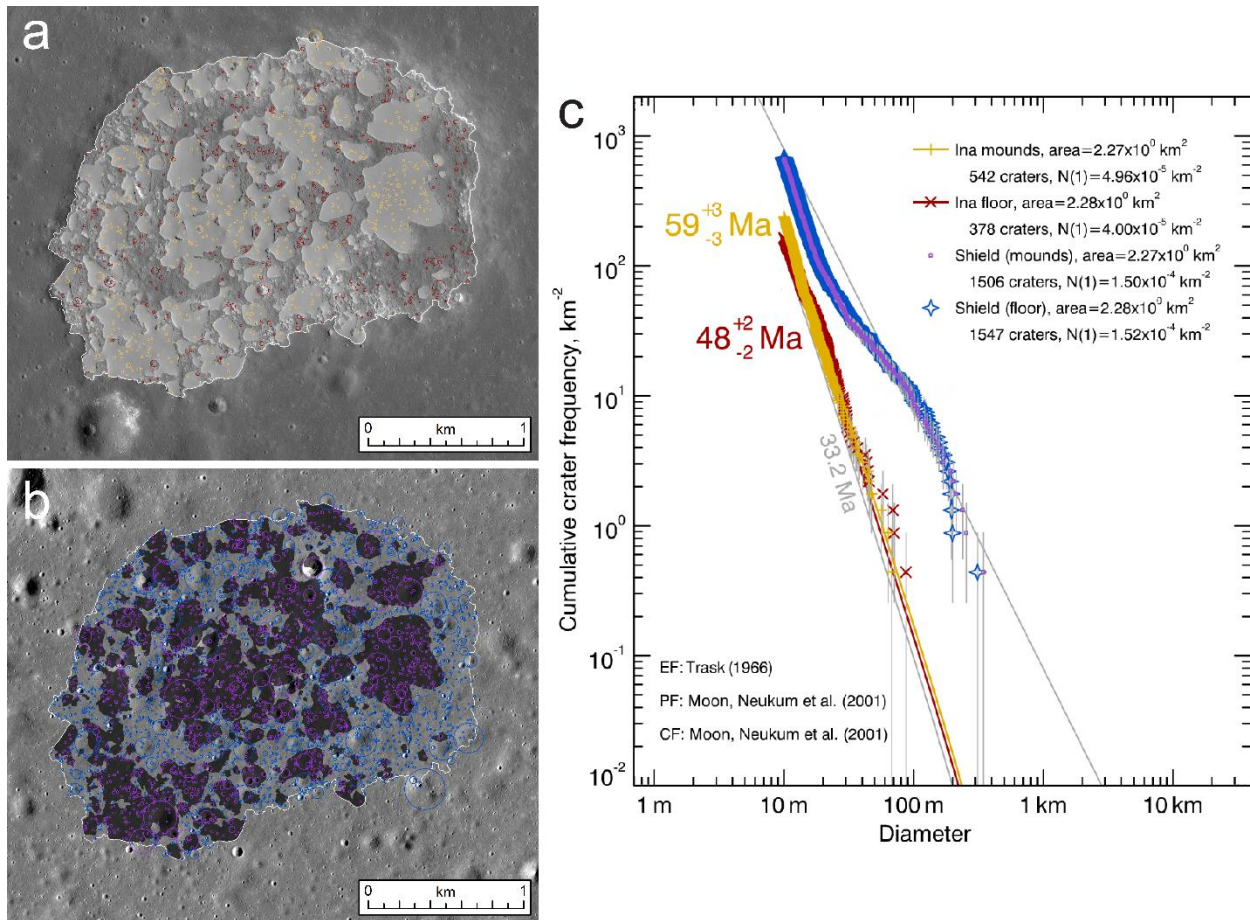
1959

Figure 14. Pits (marked by white arrows) observed at Ina interior terrains; each scale is 50 m. All panels are portions of LROC NAC frame M119815703.



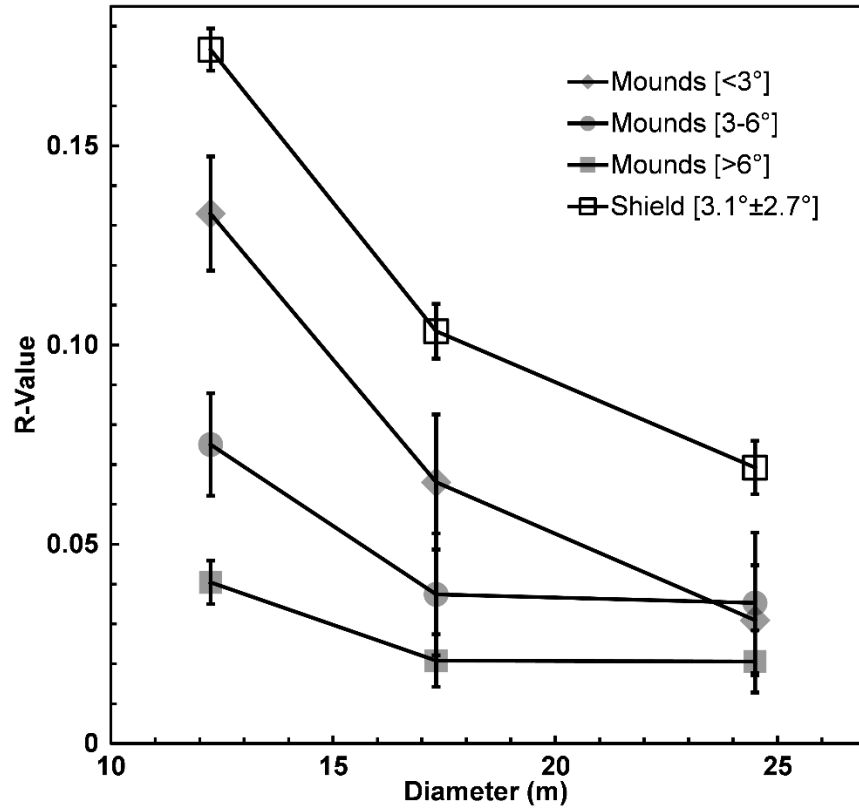
1960

1961 **Figure 15.** Impact craters on the Ina interior terrains: (a) a crater with relatively sharp rim crests
 1962 on the mounds, (b) a crater on the surrounding mare (for comparison; centered at 18.453°N,
 1963 5.311°E), with comparable rim morphology crispness of the crater in panel (a), surrounding halo
 1964 formation is observed, (c-e) representative craters on the floor terrains, (f) a very shallow impact
 1965 crater on the floor, (g-h) blocky craters on the floor, and (i) a crater at the mound-floor boundary.
 1966 All panels are portions of LROC NAC frame M119815703, and each scale is 20 m.



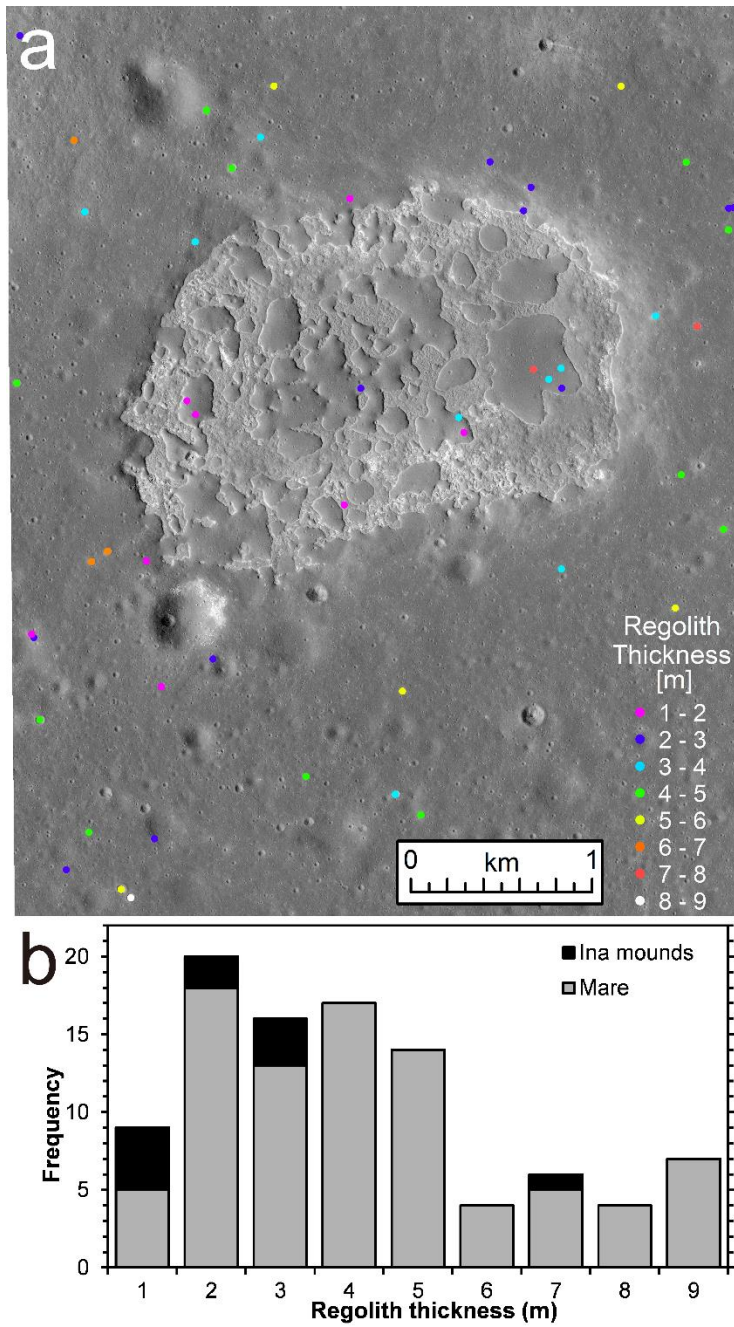
1967

1968 **Figure 16.** (a) Superposed impact craters (with rim positions marked by circles) identified on the
 1969 Ina interior mounds (yellow circles) and floor terrains (red circles). The mounds are lightly
 1970 masked out by grey patches and Ina interior floor is outlined by the white polygon. The
 1971 background image is a portion of LROC NAC frame M119815703. (b) Spatial distribution of the
 1972 counted impact craters on the surface region (delineated by white line) on the shield flank
 1973 surrounding Ina, with the same area and shape as the Ina interior (see its location in Figure S1a).
 1974 The patches with the same areas and shapes with Ina interior mounds are marked by darker color.
 1975 Craters superposed on the areas with same shapes with Ina mounds and floor units are marked by
 1976 violet and blues circles, respectively. Background image is a portion of LROC NAC frame
 1977 M1138873574. (c) Cumulative size-frequency distribution of impact craters superposed on the
 1978 Ina interior mounds (yellow crosses) and floor units (red multiplication signs), and surrounding
 1979 shield mare regions with same areas and shapes of the interior units (mounds: violet dots, floor:
 1980 blue stars, panel (b)). The fitting of the model age is based on the Neukum lunar PF and CF,
 1981 using the CraterStats software package (Micheal & Neukum, 2010; Michael et al. 2016). The
 1982 gray line on the right is the lunar equilibrium function (EF) curve from Trask (1966), and the left
 1983 one is the 33.2 Ma isochron reported by Braden et al. (2014).



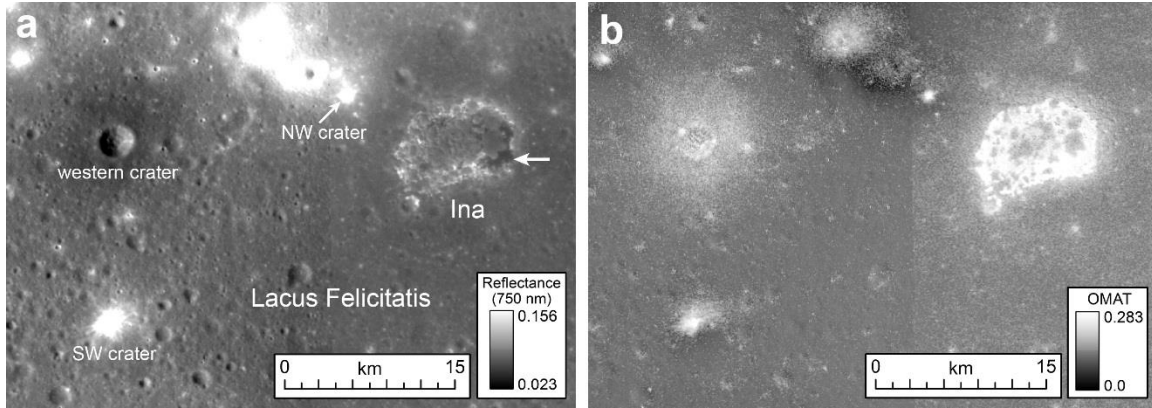
1984

1985 **Figure 17.** Plot of crater size-frequency distribution (R-values calculated based on Crater
 1986 Analysis Techniques Working Group (1979)) with several diameter ranges (10–15 m, 15–20 m,
 1987 and 20–30 m) for representatively-sloped areas on Ina mounds outlined in Figure S15 and
 1988 surrounding shield volcano surface marked by dark patches in Figure 16b. See Table S2 for the
 1989 specific values.



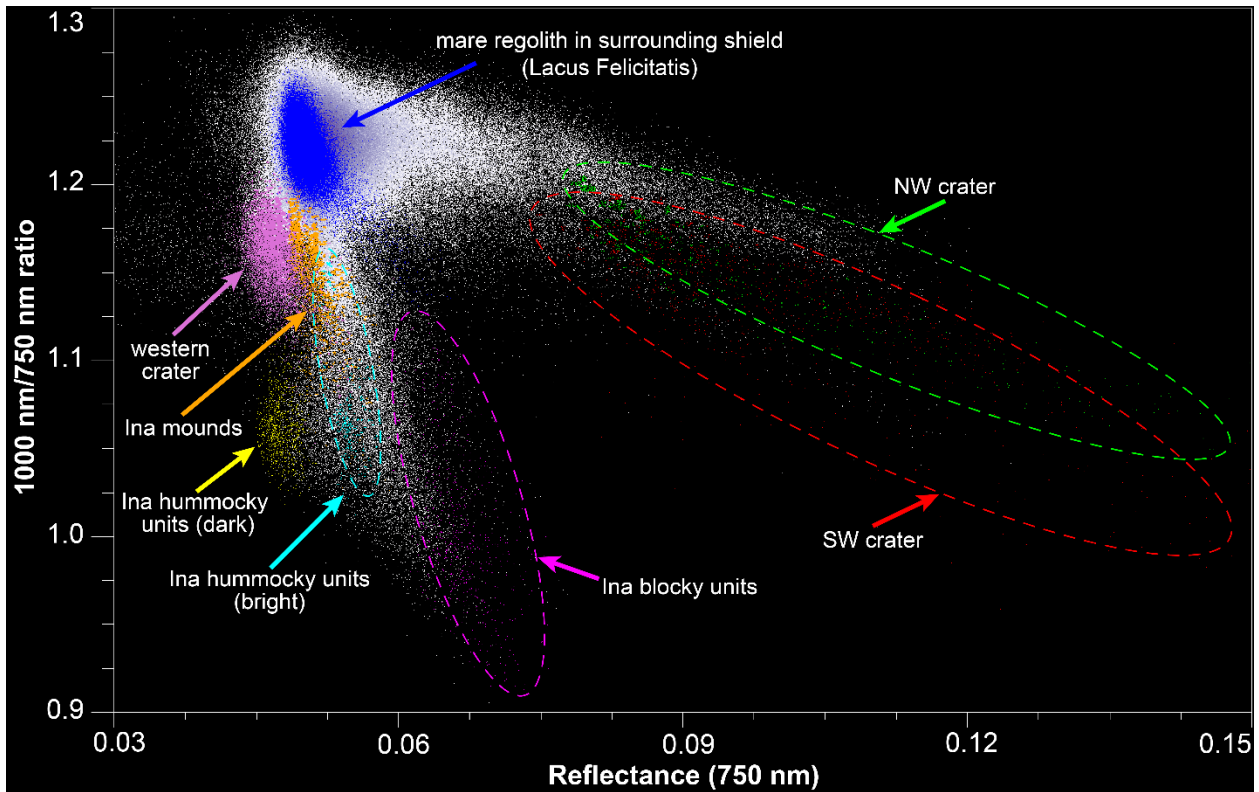
1990

1991 **Figure 18.** (a) Regolith thickness of the Ina interior mounds and the surrounding shield area
 1992 determined from crater interior morphology and diameters on LROC NAC frame M119815703
 1993 and (b) their histogram.



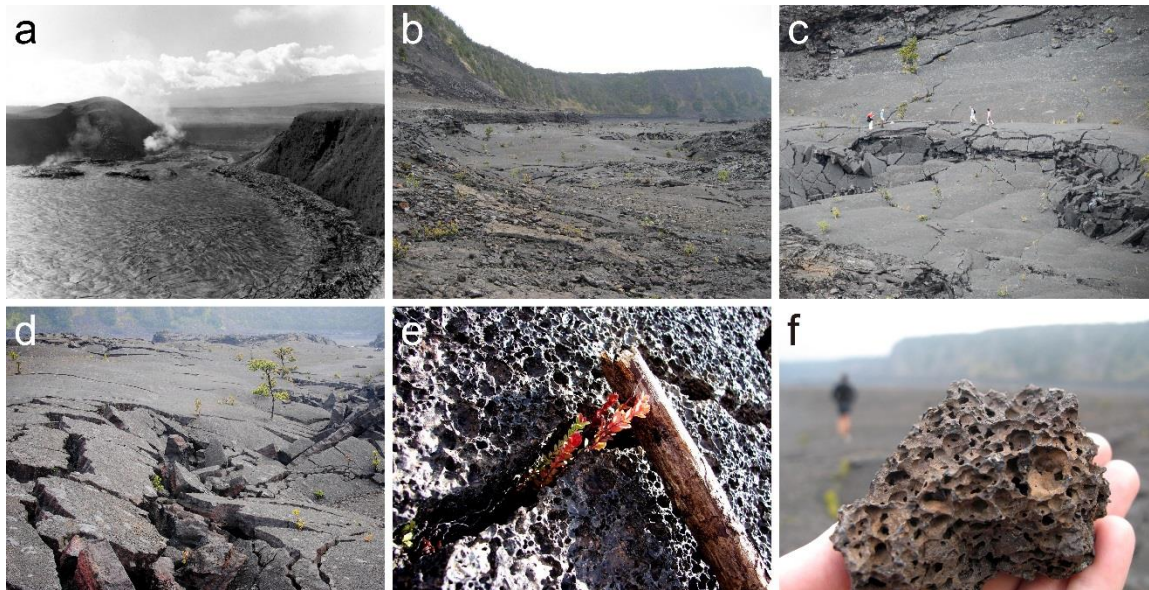
1994

1995 **Figure 19.** Kaguya MI (a) 750 nm reflectance and (b) optical maturity maps of Ina and the
 1996 surrounding region. The thicker arrow at the right edge in panel (a) indicates the darker portion
 1997 of the Ina floor hummocky units.



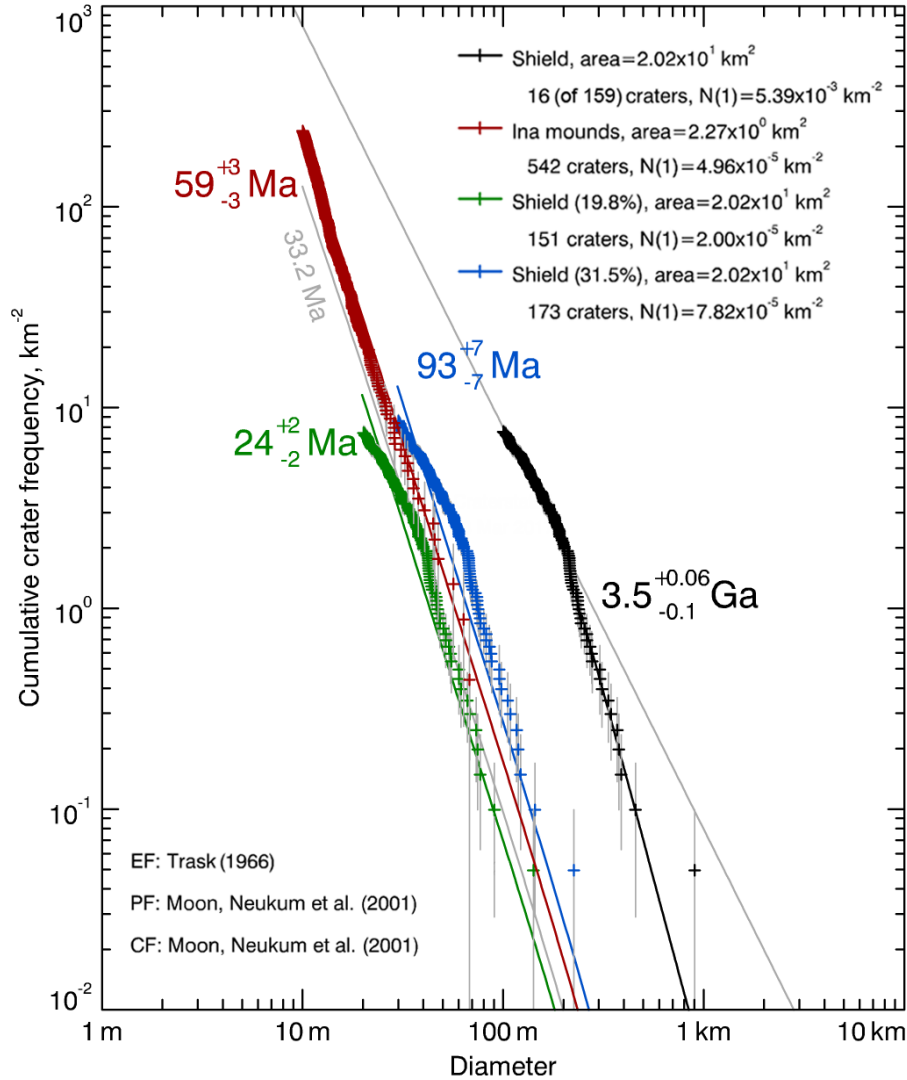
1998

1999 **Figure 20.** 2-D scatter plot of Kaguya MI 1000 nm/750 nm reflectance ratio, as an indicator of
 2000 the 1 μm mafic absorption band strength, against 750 nm reflectance. Multiple surface features
 2001 within and surrounding Ina are plotted with differently colored data points and their values are
 2002 cataloged in Table S3.



2003

2004 **Figure 21.** Kīlauea Iki summit pit crater/vent on the Kīlauea shield volcano, Hawai'i. (a) The
 2005 third phase of activity in Kīlauea Iki Crater during the 1959 Kīlauea eruption. Note the chilled
 2006 ledge (right), ~15–60 m wide and approximately 15 m high, surrounds the entire lava lake. The
 2007 vent at the base of Pu'u Pua'i cone and the largest island (upper left) continue to emit fumes.
 2008 View is from Byron Ledge overlook after activity ceased. U.S. Geological Survey photo
 2009 rdh00079 taken on December 2, 1959. (b) Northwest edge of the Kīlauea Iki crater floor. Note
 2010 the elevated marginal ledge formation and the highly fractured crater floor crust. Photo by Scott
 2011 Carpenter on February 10, 2009 (www.flickr.com/photos/scarpenter/3300718818/). (c) West
 2012 floor of Kīlauea Iki crater, near the Pu'u Pua'i cone. Note the draped plate at the edge of pre-
 2013 eruption topography (top), the chilled marginal terrace, and the pressure ridge (center with hikers
 2014 on top) formed by deformation of the subsiding rigid crustal layer on top of the lava lake. Note
 2015 evidence for abundant void space associated with these deformed plates. U. S. National Park
 2016 Service photo taken on November 11, 2010. (d) The deformed, fractured and macro-vesicular
 2017 nature of the lava lake crust present at the west Kīlauea Iki crater floor. Photo by Harry Chen on
 2018 November 26, 2011 (www.flickr.com/photos/harrychen/6434789769/). (e) A close look at the
 2019 Kīlauea Iki lava lake crust floor. Note the abundant small vesicles and the several centimeters-
 2020 long plants for scale. Photo by Jenny Levine on November 8, 2007
 2021 (www.flickr.com/photos/shifted/2044399797/). (f) A sample of the crater floor plate, showing
 2022 the highly micro-vesicularity property. Photo by Chris McGillicuddy on November 27, 2011
 2023 (www.flickr.com/photos/mcg/6412143341/).



2024

2025 **Figure 22.** Investigation of the response of solid magmatic foam substrate to the formation and
 2026 retention of superposed craters, and the estimated crater counting model ages. The cumulative
 2027 SFD of craters identified on the shield flank (Figure S1) and Ina mounds (Figure 16) are re-
 2028 plotted here as black and red crosses, respectively. All the counted shield craters are re-sized
 2029 with their diameters reduced by factors of ~ 3 and ~ 5 (specifically, 19.8% and 31.5% of the
 2030 original values), and cumulatively plotted as green and blue crosses, separately. The gray line on
 2031 the right is the lunar equilibrium curve from Trask (1966), and the left gray line is the isochron
 2032 for the 33.2 Ma age obtained by Braden et al. (2014). The model age fitting is based on the
 2033 Neukum lunar PF and CF, using the CraterStats software package (Micheal & Neukum, 2010;
 2034 Michael et al. 2016).